# MECHANICAL CONTROL OF THE KONDO EFFECT AND SPIN STATES IN SINGLE MOLECULES

A Dissertation

Presented to the Faculty of the Graduate School

of Cornell University

in Partial Fulfillment of the Requirements for the Degree of

Doctor of Philosophy

by

Joshua Joseph Parks

August 2009

MECHANICAL CONTROL OF
THE KONDO EFFECT AND SPIN STATES
IN SINGLE MOLECULES

Joshua Joseph Parks, Ph.D.
Cornell University 2009

This dissertation describes measurements of electron transport through single molecules in mechanically controllable break junctions.

In the first two experiments, we study molecules in the Kondo regime at low temperature. We vary the electrode spacing to tune the spin-$\frac{1}{2}$ Kondo effect in a $C_{60}$ molecule as well as its lowest-energy vibrational mode. In the second experiment, we achieve spin control in an organometallic cobalt complex by stretching the molecule, thereby breaking its symmetries.

We also describe the fabrication of ferromagnetic-electrode devices for the study of spin-dependent transport through individual molecules and nanoparticles. Finally, we present the development of an instrument for the measurement of single-molecule conductances at room temperature by repeatedly forming and breaking contact between two gold surfaces in a molecular environment.

## BIOGRAPHICAL SKETCH

Joshua Parks spent much of his early childhood in Seoul, one of the world's most vibrant and cosmopolitan cities that, as the greater powers would have it, is located merely 30 miles from the world's most heavily militarized border. The excitement of air-raid sirens and drills proved to be a bit much, and his family moved to Philadelphia, PA, where Josh would grow up eating Philly cheesesteaks, playing Little League Baseball, taking violin lessons at Temple Music Prep, and of course, getting heartbroken at the end of every professional sports season – a streak that finally ended on a fateful October evening in 2008.

Josh got his first flavor of scientific research during the summer after the 9th grade, in Jonathan Chernoff's lab at Fox Chase Cancer Center, where he studied problems in protein phosphorylation. Jon's insight in letting him work on a hot, newly discovered tumor suppressor gene led to nice results: the top award by the Biotechnology Industry Organization in 1997 and 1st place at the Intel International Science & Engineering Fair in 1999.

Up to this time (and perhaps still now), Josh's most notable achievement in physics was having to stand in a corner for failing a Gauss's Law exam in the 12th grade, bringing his high school physics teacher, Dr. Joel Simon, much undeserved grief.

Josh entered Harvard College in the Fall of 1999, eager to delve deeper into cell biology. But he slowly got peer-pressured into venturing towards the physical sciences. The first stop was structural cell biology in the lab of Stephen Harrison, where Josh crystallized tricky proteins, and had fun shooting x-rays.

The scale started to tip during the Fall semester of his junior year, when Jan Hendrick Schön published eye-catching papers every week that piqued Josh's interest in device physics. He was also inspired in defeat by an "introductory"

quantum mechanics class taught by Daniel Fisher whose participants still carry a badge of honor. The final straw was several close friends, including Greg Tseng, convincing him during winter break to study physics.

In March 2002, Josh finally made the leap, getting in touch with Charlie Marcus to start trying to reproduce Hendrick Schön's results. Two months later, the *New York Times* broke news of the Schön affair. Oh well. Undaunted, Josh decided to switch from the biochemistry to the physics concentration during the summer, and applied to graduate programs six months later, beginning a serious effort to catch up with the curriculum. Much of it was not pretty: he still has in his possession an email from Mike Tinkham regarding a final exam in which he got the second-lowest score. Josh still managed to graduate *magna cum laude* in June 2003 with a degree in chemistry and physics.

In the Fall of 2003, he came to Ithaca, NY, to pursue graduate studies at Cornell, where he had a lot of fun working in Dan Ralph's group and TA'ing two semesters of the honors physics sequence. Outside of the lab, he enjoyed the flexibility to pick up new hobbies and rekindle old interests for the maintenance of sanity within the bustling mecca of Ithaca, NY. These excursions have included running, rowing, poker, avid reading, music, a renewed commitment to chocolate and espresso, and of course the one constant throughout his stay: dedicated abstinence from Finger Lakes wines [*ed:* This has recently been broken]. Despite his constant struggles with the town and the extreme weather, he has decided to stay another year to learn some chemistry and to play with graphene.

To my parents.

## ACKNOWLEDGEMENTS

I'd like to begin by thanking past and present members of my thesis committee: Paul McEuen, Garnet Chan, Piet Brouwer, Héctor Abruña (honorary), and Dan Ralph. Paul has been an influence far beyond the three oral exams of mine through which he has had to sit. His exquisite taste for scientific research is something that is particularly exceptional, even among the very best. During my time as a graduate student, it was amazing to see Paul keep up with his professorial duties, write novels, and at the same time have his group churn out papers that make you say, "Wow." I hope to learn a lot more from him as I venture into carbon-land.

I owe Garnet much thanks for reaching out actively and offering to help us understand our data, which really got the ball rolling on the cobalt terpy project. He was also incredibly nice in joining my committee on such short notice. Garnet recently won the ACS Pure Chemistry prize, and its prestige is obvious if you take a look at the list of past winners. I expect great things from Garnet, and hope to continue to collaborate with him down the road. I also give him much respect for furnishing his group with Herman Miller chairs.

If I had a dime for every silly question that I asked Piet before, during, and after his solid-state class, I'd be pretty wealthy. Piet really took the time to patiently explain to me topics ranging from the Kondo effect to Fermi liquid theory to interference effects, and even whether there is an IRG meeting. Another amazing aspect of Piet is how well he is able to relate to experimentalists. I wish him the best in his Humboldt Professorship; he will truly be missed on the 5th floor of Clark Hall.

Prof. Abruña adopted me as an honorary group member over the past year, and this has led to not only fruitful work on organometallic complexes and

conductance measurements, but also to fantastic wine, food, and coffee. Every year, he throws a fantastic party for his group, and these parties would be one of the few things that could attract me back to Ithaca once I leave. I also owe much thanks for his being a second advisor to me, offering valuable advice about careers and science, and helping to open up channels for me to stay in Ithaca for another year. His love of coffee was a major bargaining chip used when asking Dan for a Gaggia espresso machine for our office.

Finally, we come to my advisor, Dan Ralph. I first met Dan at March Meeting 2003 in Austin, where in my youthful naïveté, I fearlessly approached top experimental condensed matter physicists in the hallways to talk, with the excuse that I was deciding on graduate programs to attend in the Fall. Dan took the time to talk to me in the Hyatt ballroom for over an hour, telling me about Cornell and the research going on in the group. (Dan, by the way, had 3 students giving invited talks that year.) The encounter made a very positive impression, and was a major reason why I chose to attend Cornell. During my first semester, I TA'ed an honors mechanics class that Dan was teaching, and got a glimpse of how well he takes care of students. Dan did so many things to greatly reduce my workload, so that I only had to focus on leading effective sections.

After joining the group during the summer after my first year, it became very evident that doing graduate work in the Ralph group is an amazing experience. You never have to worry about anything other than your research: account numbers mysteriously get updated, stipend checks arrive, and Dan comes down every day to talk about physics and to provide any additional support that you need. As if that weren't enough, the facilities and funding will spoil you for life; liquid helium flows freely, e-beam lithography sessions can go on interminably, and if you ask for a new piece of equipment short of a dilution refrigerator, there

will be a big package waiting for you within a few weeks. (Recently, a student casually asked for a new probe station with a projected-field magnet, and voilà, he got one.) The aforementioned is a small testament to the perfect environment for experimental physics that Dan provides for the group. In terms of his style, he teaches you to be an independent, thorough experimentalist (we will all miss the intense paper-writing process), so that by the end, you are ready to stand on your own feet. There were probably many times during graduate school when I could have used a butt-kicking, but I really appreciate how Dan let me work through my issues, being nearby if I needed any help. Without the guidance and support of Dan, the content of this thesis would not have been possible. Thank you.

I thank David Goldhaber-Gordon for teaching me so much over e-mail and through coversations at conferences and visits during the past 6 or 7 years. David's graduate work largely shaped my research direction during the early part of grad school, and it was through a second reading of his seminal Kondo paper that things finally "clicked" for me. I have been very embarassed over the years, because David has always treated me like a direct colleague even as far back as when I was an undergrad, but this is just a small testament to his amazing kindness and humility.

Recently, I have had the privilege of learning a lot from Theo Costi. His lucid explanations about the underscreened Kondo effect and his providing us with results of NRG calculations have been extremely helpful in understanding and analyzing the cobalt terpy data.

The NSF graduate research fellowship program has funded three years of my time in graduate school, and I sincerely thank them for their generous support.

I come to the scientific mentors who inspired me prior to graduate school. I thank Charlie Marcus for his contagious enthusiasm for science and his single-handedly getting me, who had been a physics major for less than a semester, into the top graduate programs. During my short time with his group, I met numerous prominent physicists who stopped by Charlie's lab; these 20 or so encounters are what gave me the brash confidence to approach and talk to physicists like Dan at conferences. The amount of attention that I received from Charlie was just amazing, and he really went out of his way to make me gain the broadest perspective that I could in the shortest time possible. I also thank Andy Kent for his guidance and his teaching me lithography and measurements during my first summer with the Marcus Lab.

I thank Steve Harrison and Yizhi Tao for showing me how beautiful structural biology can be; this was my launching point to get into physics. I thank Jon Chernoff for giving me almost 4 years of lab experience prior to entering college. Jon worked with me directly at least twice a week, and I really appreciate how much time and energy he gave to a high school student. This experience is why I decided to go into science; it also made every molecular biology lab course a piece of cake.

I thank three teachers from high school: Dr. Joel Simon, who planted the first seeds of my interest in physics; Mr. Brooks, who taught me college-level organic chemistry that is useful even now; and Mr. Erlick, for running a research program and matching us up with academic and industrial labs around Philadelphia.

There were several people who were instrumental in my grad school application process, both in helping me to get into programs and in making informed decisions. I thank Hongkun Park, Bill Klemperer, Howard Georgi, and Masahiro

Morii, who all discussed with me various programs and wrote letters on my behalf. Greg Tseng helped a tremendous deal, having gone through the application process only 2 years before. Tomokazu Sato is responsible for making sure that my physics GRE scores were acceptable, by shaming me into aiming higher the day before the exam. I also thank Shaffique Adam not only for an exciting endorsement of Cornell at the 2003 March Meeting, but for also hosting me during visitation weekend. Connie Chang and Hande Ustunel showed me around Ithaca that weekend. Talking to Abhay Pasupathy was particularly influential, as I feel that our conversation of single-molecule transport over sandwiches and wraps was what really sealed the deal for my coming to Cornell.

At Cornell, David M. Lee provided me with much needed encouragement when I was having doubts about staying in graduate school during my first year. The tremendously positive interactions with Dave on a regular basis during the Spring of 2004 was what made me stick it out.

Much of my life over the past 5 years has been spent in Dan's lab. I began working with Alex Champagne, who is an absolutely amazing experimentalist and who worked on a challenging thesis that I could never have finished. It is because he spent so many tireless hours designing and building two versions of the mechanically controllable break junction that my thesis became possible. Alex worked with me by teaching me all the fundamental skills needed to survive in a lab, and I have tried my best to emulate his approach when working with younger students. Among the many things that Alex introduced to me was excellent beer.

After Alex left for his postdoc, Kirill and Ferdinand helped me survive. Whenever I ran into a problem in the lab, they helped me intently as if it were their own problem and helped me resolve issues quickly. Thanks to Kirill for

patiently explaining to me so much physics and for putting up with all my Borat impressions. Thanks to Ferdinand for tirelessly answering all my technical questions, for his delicious baked goods, and for all the fun times from the tea pahtay to all the shenanigans.

Jacob taught me how to cool and run a fridge, invited me over for delicious meals, and most importantly (as some might argue), taught me to play ping-pong. Although Dan jokingly gave us grief, it was also very nice to have a fellow Harvard alumnus in the lab with whom I could reminisce about painful undergraduate experiences. Thanks to Jack for always reminding me that things will get better, for pointing out Ferdinand's pronunciation of "cantilever", and for setting up things like the basement murder mystery game.

I have much for which to thank Kiran, who joined the Ralph group at the same time as I did. We really survived grad school together, and she was one of the few people to whom I could complain about Ithaca. Like clockwork, Kiran would give me a call on snowy days so that we could commiserate. I am very happy that she will be moving to California, but I will really miss those phone calls where we would laugh because that was the only way to cope.

Thanks goes to Sufei for putting up with me (I gave him a lot of grief over the years) and for being such a good sport about everything (cf. pen fifteen). I'm so glad that we were in the Ralph group together. Thanks to Yongtao for his incredibly funny one-liners, for reminiscing about high school math and physics competitions with me, and for holding the Ralph group record of being the object of man crushes.

I have also had the pleasure of working with Eugenia, who is an incredibly sharp and talented experimentalist. When taught how to do something, she is often three steps ahead. I once jokingly told her to go make photomasks,

giving minimal information on how to do it. Within 24 hours, she had made a full set of masks with all the new alignment marks and important features already incorporated. This type of initiative made our collaboration in building and writing software for the sewing machine an absolute joy. It was also really nice to have a wine, coffee, and running buddy. I also thank Mitk'El for his "fundamental" happiness; it was an absolute pleasure to work together. With Saikat joining the group last Fall came incredibly fresh ideas and plenty of great conversations about life and science. Thank you, Saikat.

I thank my collaborators Geoff Hutchison, Samuel Flores-Torres, Eric Neuscamman, and Angang Dong.

I also thank the other Ralphies: Marie, Sergey, Ilya, Janice, Chen, Lin, Wan, Taka, Colin, Ted, and Alex. The other folks in the Clark basement: Markus, Vera, Shahal, Arend, Nathan, Vlad, Praveen, and Ethan.

Several summer students in the group made things a lot more fun. Linh Pham was a superstar REU student that I had the chance to work with. I wish her the best in her current graduate studies at Harvard. I also thank Thiti, Kristin, Lauren, Mark, Tina, and Christine.

During grad school, I had opportunities for musical collaborations. Thanks to Nozomi, Ferdinand, Ivan, Robin, Albert, Andrew, Huimin, and Sophie for all the fun chamber music we got to play.

Thanks to all the people who kept me sane outside of the lab: Ryan, Spencer, Dave, Matt, Zack, Evan, Ameya, Cooper, Dana, and Alex.

And thanks to my Physics 116 and 217 sections: you guys really were fantastic. Thank you for all the hard work and all the fun during our year together.

## TABLE OF CONTENTS

## LIST OF TABLES

## LIST OF FIGURES

CHAPTER 1

# OVERVIEW OF THIS THESIS

Single molecules represent the ultimate limit in the miniaturization of an active device element. But because of a molecule's small size ($\sim 1$ nm), fabricating electrical devices based on individual molecules to measure their conductance and to control their properties has been a very difficult task. This dissertation describes progress that has been made on these fronts in measurements of electron transport through single molecules in mechanically controllable break junctions.

Chapter 2 provides an introduction to the Kondo effect and to the primary experimental tool that we use in this thesis. In chapter 3, we vary the electrode spacing to tune the spin-$\frac{1}{2}$ Kondo effect in a $C_{60}$ molecule and observe good agreement with predictions such as universal scaling. We are also able to observe and tune features arising from the lowest-energy vibrational mode of $C_{60}$. Chapter 4 describes an experiment in which we achieve spin control in an organometallic cobalt complex by stretching the molecule, thereby breaking its symmetries. Chapter 5 describes the fabrication of ferromagnetic-electrode devices for the study of spin-dependent transport through individual molecules and nanoparticles. It also covers some of the experiments that were pursued. Finally, we present in chapter 6 the development of an instrument for the measurement of single-molecule conductances at room temperature. This is achieved by repeatedly forming and breaking contact between two gold surfaces in a molecular environment, and we present a few preliminary results.

CHAPTER 2

# INTRODUCTION TO THE KONDO EXPERIMENTS

In this chapter, we provide background for the discussion of the single-molecule Kondo experiments. We begin with an experimentalist's introduction to the Kondo effect, with emphasis on concepts and phenomena. We then introduce our primary experimental tool: the mechanically controllable break junction.

## 2.1 Background

The Kondo effect is one of the most intensely studied phenomena in condensed matter physics. It concerns the behavior of a magnetic impurity embedded within a metallic host. As the temperature is lowered, the effective behavior of the impurity can transition from magnetic to non-magnetic, owing to a many-body interaction with the conduction electrons.

The origin of the Kondo effect goes back to the observation of peculiar behavior in the resistivity of normal metals during the 1930's. As a metal is cooled to the lowest temperatures and the electron-phonon scattering mechanisms are frozen, one might expect to enter a regime in which the only contribution to the resistance is impurity scattering, and thus the metal's resistivity should saturate to a finite value. However, it was noticed that a local *minimum* (rather than a saturation) in the resistivity can occur. This remained a mystery for 30 years until a basic theoretical understanding in 1964, when Jun Kondo associated the resistance minimum with the presence of magnetic impurities, and showed that the behavior occurs due to the screening of a local moment by the conduction

electrons in the host metal [1]. A many-body spin-singlet state is formed because the spins of the conduction electrons interact antiferromagnetically with the spin of an impurity, which leads to the formation of a virtual bound state at the Fermi energy of strength $\sim k_B T_K$. At temperatures below this characteristic energy scale, a magnetic impurity in the metal promotes spin-flip scattering, which results in a rise, and hence a local minimum, in the resistivity of the metal host. The form of the Hamiltonian that Kondo used in his model was

$$\mathcal{H} = \sum_{k\sigma} \epsilon_{k\sigma} c^\dagger_{k\sigma} c_{k\sigma} + J\, \mathbf{s}(0) \cdot \mathbf{S}, \tag{2.1}$$

where $\epsilon_k$ gives the dispersion relation of the normal metal and $c^\dagger_{k\sigma}$ ($c_{k\sigma}$) are the creation (annihilation) operators for a conduction electron with wavevector $k$ and spin $\sigma$. In the second term, the exchange coupling is antiferromagnetic $J > 0$, $\mathbf{s}(0)$ represents the spin of the conduction electron at the site of the impurity, and $\mathbf{S}$ is the spin of the impurity. This is known as the Kondo or the *s-d* exchange Hamiltonian, and we will revisit this in the next section.

Another ~30 years after this milestone, the Kondo effect experienced a renaissance due to developments in nanofabrication techniques that enabled electron transport measurements through tunable quantum dots. These are entities that have a discrete energy spectrum owing to quantum size effects, realized in gate-defined semiconductors, carbon nanotubes, and in molecules. In such quantum-dot devices, the controllability is such that the Kondo effect can be studied at the level of a *single* localized impurity – provided by an unpaired electron on the quantum dot – interacting with the spin of the conduction electrons.

By now, the original Kondo problem is very well-understood and is covered in great detail in a graduate-level course, e.g. that of Piet Brouwer. I cannot possibly do justice to 75 years in the development of the Kondo effect, so my

goal for this chapter is to distill the main concepts and to provide background for the next two chapters. For additional enrichment, there exists a standard reference by Hewson [2], nice coverage in a book on many-body transport [3], and a review article by Pustilnik and Glazman that provides treatment beyond the spin-$\frac{1}{2}$ picture [4]. If the reader is new to the Kondo effect, then I would recommend the review by Kouwenhoven and Glazman [5].

One final note before embarking on our discussion. We will be focusing on a Kondo effect originating from a spin impurity. However, a magnetic Kondo effect is not the only possibility, as the key ingredient for the realization of a Kondo effect is a local degeneracy. This can be manifest in several different ways: Kondo signals arising from two-level tunneling systems [6], the degeneracy of orbital quantum states [7], and possibly even degenerate charge states [8].

## 2.2 The Anderson model and the origin of $J > 0$

We first begin by discussing the Anderson model [9], which was introduced in 1961 by Phil Anderson as a simple microscopic description of a transition metal impurity in a normal metal. This will be useful in our later discussion of quantum dots, as many quantum-dot devices are well-described by the Anderson model. The goal of this section is to 1) establish parameter regimes in which there exists a local magnetic moment (for the observation of the Kondo effect) and 2) to show the microscopic origin of the antiferromagnetic interaction between the spin of the localized impurity and the spin of the conduction electrons. In the process, we will relate the Anderson model back to the Kondo model (Eq. (2.1)).

The Anderson Hamiltonian includes the Fermi sea of conduction electrons

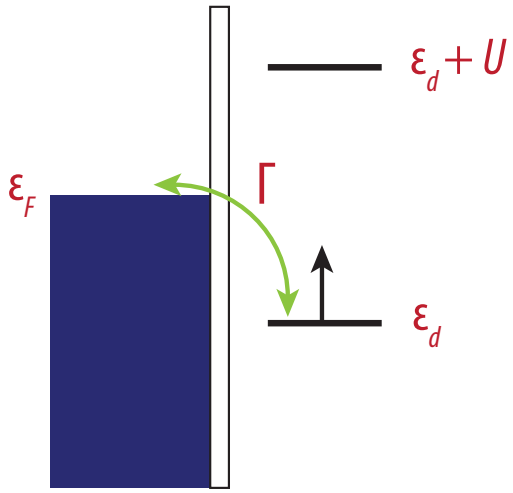


**Figure 2.1:** Schematic of the Anderson model, showing a localized impurity site that is coupled to the Fermi sea of conduction electrons. The situation in which the impurity site is singly occupied is of greatest interest (see text).

in the metal (the extended $s$-orbital states) and a localized impurity level (traditionally, a $d$-orbital state) of energy $\epsilon_d$:

$$\mathcal{H} = \sum_{k\sigma} \epsilon_{k\sigma} c^\dagger_{k\sigma} c_{k\sigma} + \epsilon_d \sum_\sigma d^\dagger_\sigma d_\sigma + U n_{d\downarrow} n_{d\uparrow} + \sum_{k\sigma} \left( t_k c^\dagger_{k\sigma} d_\sigma + t^*_k d^\dagger_\sigma c_{k\sigma} \right). \tag{2.2}$$

There is also a Coulomb interaction term of energy $U$ when the impurity level is doubly occupied. Finally, there exists a hybridization term with matrix elements $t_k$, which allows an electron to hop on and off the impurity site from and to the Fermi sea. The energy scale associated with this hybridization is $\Gamma(\epsilon) = 2\pi \sum_k |t_k|^2 \rho(\epsilon_k)$, as given by Fermi's golden rule. A schematic of the Anderson model is shown in Fig. 2.1.

The model allows for possible occupation of the impurity site by either 0, 1, or 2 electrons, with chemical potentials 0, $\epsilon_d$, and $\epsilon_d + U$, respectively. We are interested in the parameter regime in which there exists a local moment, which can only occur when the impurity level is singly occupied, as a second electron has to fill the level with an opposite spin according to Pauli's exclusion principle.

Therefore, the existence of a local magnetic moment requires three conditions:

1. $\epsilon_d < \epsilon_F$: the impurity level is below the Fermi level, as to ensure occupation.
2. $\epsilon_d + U > \epsilon_F$: the doubly occupied level is above the Fermi level, as to exclude double occupation.
3. $\Gamma < \epsilon_F - \epsilon_d$ and $\epsilon_d + U - \epsilon_F$: the width of the impurity level, $\Gamma$, a measure of the lifetime broadening due to hybridization of the level with the Fermi sea, is smaller than the energy difference between the Fermi level and both the singly and doubly occupied levels.

While the above parameters ensure a ground state of single occupancy, we can consider virtual (i.e. second-order) excitations to an impurity state with 0 or 2 electrons. From second-order perturbation theory, we know that the energy correction terms will go as $\sim |t_k|^2/(\epsilon_F - \epsilon_d)$ for excitations to the unoccupied state, and $\sim |t_k|^2/(\epsilon_d + U - \epsilon_F)$ for excitations to a doubly-occupied state. We also know two other things: 1) the excitations must involve a conduction electron of spin opposite to that of the impurity (Pauli exclusion principle), and 2) from quantum mechanics, second-order perturbative energy corrections are always negative. Therefore, if we capture the above with an effective Hamiltonian, treating the perturbation term as a Heisenberg-like exchange, we have

$$\mathcal{H}_{\text{eff}} = \sum_{k\sigma} \epsilon_{k\sigma} c^\dagger_{k\sigma} c_{k\sigma} + \sum_{kk';\sigma\sigma'} J_{kk'} \mathbf{S} \cdot (c^\dagger_{k\sigma} \boldsymbol{\sigma}_{\sigma\sigma'} c_{k'\sigma'}). \tag{2.3}$$

The coupling $J_{kk'}$ must be positive, since the perturbation term is derived from excitations of opposite spins, and because the overall sign of the term is negative. Thus the interaction between the local moment and the conduction electrons must be antiferromagnetic. Schrieffer and Wolff [10] arrived at the above conclusion more rigorously, by performing a canonical transformation to show that

the Kondo model is a special case of the Anderson model, and found that the coupling constant is

$$J_{kk'} \simeq 2\left(\frac{t_{k'}^* t_k}{\epsilon_F - \epsilon_d} + \frac{t_{k'}^* t_k}{\epsilon_d + U - \epsilon_F}\right) > 0. \tag{2.4}$$

If we set the spin of the conduction electrons at the impurity site as $\mathbf{s}(0) = \frac{1}{2}\sum_{kk';\sigma\sigma'} c_{k\sigma}^\dagger \boldsymbol{\sigma}_{\sigma\sigma'} c_{k'\sigma'}$ and note that $t_k$ does not depend on $k$ for the localized impurity, such that we can set $J = 2J_{kk'}$, then Eq. (2.3) becomes identical to the Kondo Hamiltonian (Eq. (2.1)).

### 2.2.1 Emergence of a resonance at the Fermi energy

What is a consequence of the antiferromagnetic interaction between the spin of the impurity and the spin of the conduction electrons? When you calculate the electron scattering rate, a remarkable thing is observed: the impurity causes a dramatic enhancement of the scattering rate, but *only* nearby the Fermi energy [2], an energy scale that is not at all intrinsic to the impurity. Similar effects are observed in the $T$-matrix as well as in the energy-dependent scattering phase shifts, from which an enhancement in the density of states at $E_F$ can be explicitly calculated. The width of this resonance is $\sim k_B T_K$, the energy scale with which we had associated the virtual bound state formed between a conduction electron and the impurity.

The resonant level, pinned at the Fermi energy, emerges for $T \lesssim T_K$ as a result of the conduction electrons (with energies within $\sim k_B T_K$) collectively contributing to the screening of the local moment. For a spin-$\frac{1}{2}$ impurity, the resonant level is occupied, on average, by just a single conduction electron, which compensates the spin on the impurity and forms a spin-singlet state.

## 2.3 Effective dot Hamiltonian and the Glazman rotation

In this section, we begin to address the issue of how to describe the physics of a quantum dot attached to two metallic leads, particularly focusing on its relation to the Anderson model that was studied in Sec. 2.2. An adequate description should include the energy levels of the dot, a Coulomb repulsion term, the energy dispersion of the leads, and a tunneling term. We then arrive at an Anderson-like Hamiltonian:

$$\mathcal{H} = \sum_{\nu\sigma} \epsilon_{d\nu} d^\dagger_{\nu\sigma} d_{\nu\sigma} + U \sum_{\nu} n_{\nu\uparrow} n_{\nu\downarrow} + \sum_{\alpha\in L,R;\, k\sigma} \epsilon_{\alpha k\sigma} c^\dagger_{\alpha k\sigma} c_{\alpha k\sigma} + \sum_{\alpha\in L,R;\, k\sigma} \left( t_\alpha c^\dagger_{\alpha k\sigma} d_{\nu\sigma} + t^*_\alpha d^\dagger_{\nu\sigma} c_{\alpha k\sigma} \right) \tag{2.5}$$

We have generalized the dot to have a spectrum of energy levels $\epsilon_{d\nu}$ indexed by $\nu$, a point that we will return to later, but for these calculations, we will assume a single-level dot. In contrast to the Anderson model, there are now *two* reservoirs with which the quantum dot can hybridize, indexed by $\alpha \in L, R$. The question then arises as to whether this modification complicates the physics of the system. It turns out that the answer is largely no.

To see this, we can perform a unitary transformation of the fermion operators. Glazman and Raikh [11] used the following rotation in $L$-$R$ space

$$\begin{pmatrix} a_{k\sigma} \\ b_{k\sigma} \end{pmatrix} = \frac{1}{\sqrt{|t_L|^2 + |t_R|^2}} \begin{pmatrix} t^*_L & t^*_R \\ -t_R & t_L \end{pmatrix} \begin{pmatrix} c_{L;k\sigma} \\ c_{R;k\sigma} \end{pmatrix}, \tag{2.6}$$

which transforms the left and right reservoirs to two species of fermions whose wavefunctions are either even ($a_{k\sigma}$) or odd ($b_{k\sigma}$) with respect to the center of the dot. In applying this transformation to Eq. (2.5), we observe a remarkable thing:

the hybridization or tunneling term includes only the *even* fermion species

$$\mathcal{H} = \mathcal{H}_{\rm dot} + \sum_{k\sigma} \epsilon_{k\sigma} a^\dagger_{k\sigma} a_{k\sigma} + \sum_{k\sigma} \epsilon_{k\sigma} b^\dagger_{k\sigma} b_{k\sigma} + \sqrt{|t_L|^2 + |t_R|^2} \sum_{k\sigma} \left( a^\dagger_{k\sigma} d_{n\sigma} + d^\dagger_{n\sigma} a_{k\sigma} \right). \tag{2.7}$$

The above transformation of Eq. (2.5) describes a non-interacting, independent electron reservoir consisting of the odd combination of lead electrons, and an Anderson model with a single electron reservoir consisting only of the even combination of lead electrons. Thus, the physics is as if the dot is attached to one electrode. This is why two-channel Kondo physics [12] is not observed in such geometries.

Before continuing, I would like to add two short remarks. First, we have not yet addressed the issue of having multiple energy levels on the quantum dot. When there are many electrons on the dot, interaction effects may come into play. With a constant electrostatic interaction, as we have thus far considered, the spin $S$ on the dot alternates between $S = 0$ and $S = \frac{1}{2}$ as electrons are successively added. However, including a Hund's rule, intradot exchange coupling favors parallel alignment of spins on the dot such that an $S \geq 1$ state is possible. This could lead to higher-spin Kondo effects, as we will address in Sec. 2.4.5 and in Chapter 4. The second comment is that the notion of independent fermionic species of which only one couples to the dot, thereby providing one channel for the screening of a localized spin, is not strictly true, because the coupling to the odd species $J_2$ can be non-zero in a multilevel quantum dot, and we will discuss this later as well.

In the next section, we summarize the most salient signatures for the Kondo effect in quantum dots.

## 2.4 The Kondo effect in quantum dots

The Kondo effect in quantum dots was first observed in a lithographically defined, semiconductor quantum dot by Goldhaber-Gordon *et al.* [13] in 1998 and soon thereafter by Cronenwett *et al.* [14], kicking off a frenzy of experimental and theoretical studies. The typical Kondo temperatures in these experiments were $T_K \sim 100$ mK, so that the effect was seen only at the lowest experimentally accessible temperatures. In 2000, with the first observation of the Kondo effect in carbon nanotube quantum dots [15], $T_K$ went up an order of magnitude to $\sim 1$ K, and two years later, that figure was pushed up another order of magnitude to 10's of K in single molecules [16, 17]. Investigations of magnetic atoms on metal surfaces using a scanning tunneling microscope also showed the Kondo effect [18, 19]. These signatures were later observed for single molecules as well [20].

### Conditions for the observation of the Kondo effect

Let us begin by discussing the conditions necessary to observe a Kondo effect. First, a key ingredient for the Kondo effect is a localized impurity, which in a quantum dot is realized by an unpaired spin. For dots described by the constant interaction model in which the spin filling alternates between $S = 0$ and $\frac{1}{2}$, an odd-even behavior – alternating between a Kondo effect and no Kondo effect as successive electrons are added – has been observed. Most generally, a local moment with an accessible doublet is sufficient.

Second, since the Kondo resonance is formed for $T \lesssim T_K$, the Kondo temperature needs to be experimentally accessible. To achieve this, there are two

requirements: 1) the dot needs to be well-coupled to the electrodes, and 2) the dot needs to be small. As we discussed in the previous section, the strength of antiferromagnetic coupling between the spin of an impurity and the spin of the conduction electrons is dependent on the tunneling matrix elements, so that a larger $\Gamma$ will aid in the formation of the Kondo effect. Specifically, the Kondo temperature based on scaling studies [21] is given by

$$T_K = \frac{\sqrt{\Gamma U}}{2} e^{\pi \varepsilon_0 (\varepsilon_0 + U)/\Gamma U}, \tag{2.8}$$

where $\varepsilon_0$ is the energy of the localized spin relative to the Fermi level, i.e. a negative quantity. Note that $T_K$ is exponentially dependent on $\Gamma$ and $U$, so that in addition to increasing $\Gamma$, increasing the Coulomb energy $U$ by decreasing the size of the dot will yield a larger $T_K$. Fabricating a sufficiently small quantum dot was a major challenge towards the first observation of the Kondo effect. It is also a major reason why Kondo temperatures that are $\sim 2$ orders of magnitude larger than those of lithographically defined quantum dots have been observed in molecules.

If maximizing $T_K$ enables observation of the Kondo effect over a wider range of temperatures, one might then ask why $\Gamma$ is not arbitrarily increased, either to enhance the effects of or to offset any disadvantages in dot size. The first answer is that this parameter is generally not tunable for nanotubes and molecules – this thesis presents the first work in the tuning of $\Gamma$ in a $C_{60}$ molecule. In semiconductor quantum dots, in which dot-lead couplings are tunable using electrostatic gates, increasing $\Gamma$ presents two problems: 1) doing so leads to an effectively larger dot, which decreases both $U$ as well as $\Delta E$, the level spacing, and this interferes with 2) the conditions for the survival of a local moment that we proposed in the last section, i.e. $\Gamma < -\varepsilon_0$ and $\varepsilon_0 + U$, for the resolution of the Kondo resonance. Typically, $\Gamma$ cannot exceed the level spacing $\Delta E$.

### 2.4.1 Experimental signatures

Now that we understand how to create conditions that are ripe for the observation of the Kondo effect, let us discuss what might be measured in an experiment.

**Enhancement of conductance at zero-bias: Peak in $dI/dV$**

As we discussed, a hallmark of the Kondo effect is a resonance of width $\sim k_B T_K$ in the density of the states pinned to the Fermi energy. A schematic is depicted in Fig. 2.2a. The local density of states can be probed by measuring $dI/dV$ as a function of bias voltage, which shifts the chemical potentials of both the left and right leads. Figure 2.2b, taken from Ref. [22], shows $dI/dV$ traces demonstrating a clear zero-bias Kondo peak. In principle, the Kondo temperature can be extracted by setting the full-width at half-maximum of the Kondo peak to $2k_B T_K/e$ at the lowest temperature, assuming $T << T_K$ [15,18,22]. Because of decoherence that can be introduced by a bias voltage [23], a more accurate way to determine $T_K$ might be through temperature-dependent measurements of linear conductance.

**Characteristic temperature dependence of the linear conductance**

We see in Fig. 2.2b that the Kondo resonance is suppressed as a function of temperature. There is a characteristic temperature dependence for the linear conductance in a spin-$\frac{1}{2}$ Kondo system that we will discuss further in Sec. 2.4.4. We can see an example of the unique temperature dependence in Fig. 2.2c, which depicts linear conductance traces versus electron occupancy (gate voltage) at different temperatures for a GaAs quantum dot. The temperature dependence of the conductance is different for an odd number of electrons ($N+1, N+3$) on

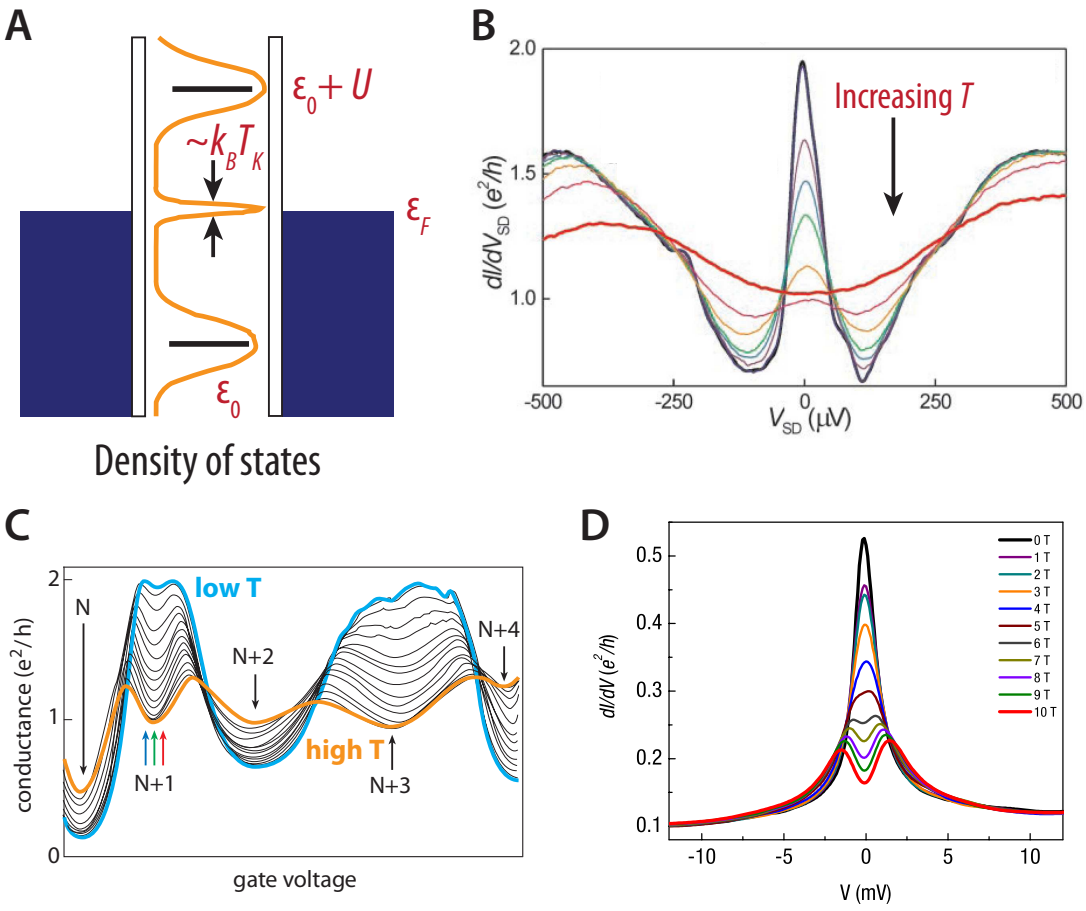


**Figure 2.2:** a) Schematic of the density of states in a Kondo-correlated quantum dot. There exists an additional resonance at the Fermi energy of width $\sim k_B T_K$. b) Differential conductance curves from [22], showing a zero-bias peak in $dI/dV$ that is suppressed with temperature. c) Linear conductance at different temperatures as a function of electron occupation, from [5]. The Kondo effect is observed for odd-electron occupation, when there is an unpaired spin on the dot. d) Magnetic field splitting of the Kondo resonance in a $C_{60}$ device.

the quantum dot, where there exists an unpaired spin and hence a Kondo effect, than for even occupancy ($N, N+2, N+4$). For the odd "valleys," conductance is maximized at low temperature and is suppressed with increasing temperature, whereas in even valleys, the behavior is the opposite. Recall that the Kondo singlet is formed for $T \lesssim T_K$. The behavior in Fig. 2.2c for odd-electron occupation is consistent with the formation of a Kondo resonance at the Fermi energy at low temperature.

**Splitting of the Kondo resonance in a magnetic field by $2g\mu_B B$**

A third signature of the Kondo effect in quantum dots is its response to an applied magnetic field. The field will alter the spin-degenerate states of the quantum dot by the Zeeman splitting, and the Kondo peak is shifted from zero-bias to finite bias $V = \pm g\mu_B B$, thus producing a splitting at twice the Zeeman energy [23]. Figure 2.2d shows an example of this for a $C_{60}$ device that we measured. The corresponding $g$-factor extracted from the peak positions is $g = 2.3 \pm 0.4$.

In the following sections, we describe each of the aforementioned points in greater detail.

### 2.4.2 Linear response conductance

We briefly summarize the calculation of the zero-temperature Kondo conductance of a quantum dot, and arrive at the result in two ways. Within the device geometry that we use to study the Kondo effect in this thesis, a primary experimental knob is the interelectrode spacing, which we vary to modify the

molecule-electrode coupling. The following results help us to understand how the asymmetry in the strength of coupling of the molecule to the two electrodes affects the Kondo conductance.

**Kubo formula**

An often used starting point for the calculation of linear response conductance is the Kubo Formula [4]

$$G = \lim_{\omega \to 0} \frac{1}{\hbar\omega} \int_0^\infty dt e^{i\omega t} \left\langle [\hat{I}(t), \hat{I}(0)] \right\rangle, \tag{2.9}$$

where $\left\langle [\hat{I}(t), \hat{I}(0)] \right\rangle$ is the current-current correlator, $\hat{I}$ is the current operator

$$\hat{I} = \frac{d}{dt}\frac{e}{2}(\hat{N}_R - \hat{N}_L), \tag{2.10}$$

and $\hat{N}_\alpha = \sum_{k\sigma} c^\dagger_{\alpha k\sigma} c_{\alpha k\sigma}$ is the total electron number operator. For Anderson-like Hamiltonians, as was used in our description of a quantum dot in Eq. (2.5), the evaluation of the Kubo formula results in the following [4]

$$G = \frac{e^2}{h} \sum_\sigma \int dE \, \frac{\Gamma_L \Gamma_R}{\Gamma_L + \Gamma_R} A_\sigma(E) \left( -\frac{\partial f}{\partial E} \right), \tag{2.11}$$

where $A_\sigma(E)$ is the spectral function and $f$ is the Fermi distribution function. The above result necessitates a few remarks. First, it connects the conductance of a quantum dot to its spectral function, a quantity that is directly related to the local density of states by $A_\sigma(E) = 2\pi\rho_\sigma(E)$. For $T = 0$, the term $-\frac{\partial f}{\partial E}$ is a sharply-peaked delta function $\delta(E - E_F)$, and thus the linear conductance through a dot will probe the local density of states at the Fermi energy. In the Kondo effect, recall that there is a resonance at $E_F$ owing to a virtual bound state, which leads to an increase in the dot conductance. This behavior is in contrast to that of the bulk resistivity in metals, where a Kondo resonance contributes to scattering, and hence, an increase in the resistivity.

Let us go ahead and compute the zero-bias Kondo conductance. The virtual bound state formed between the localized spin on the dot and the spin of the conduction electrons results in a resonance of Lorentzian form: (this can be computed from scattering phase shifts, see e.g. [2])

$$\rho(E) = \frac{1}{\pi} \frac{\Gamma/2}{(E - E_F)^2 + (\Gamma/2)^2}, \tag{2.12}$$

where $\Gamma = \Gamma_L + \Gamma_R$. Inputting the above into Eq. (2.11), we have:

$$\begin{aligned} G &= \frac{e^2}{h} \sum_\sigma \int dE \, \frac{\Gamma_L \Gamma_R}{\Gamma_L + \Gamma_R} \frac{\Gamma}{(E - E_F)^2 + (\Gamma/2)^2} \, \delta(E - E_F) \\ &= \frac{2e^2}{h} \frac{4\Gamma_L \Gamma_R}{(\Gamma_L + \Gamma_R)^2}. \end{aligned} \tag{2.13}$$

The result shows us that for a Kondo-correlated dot, the linear conductance is dependent on the dot-lead coupling asymmetry. It reaches the unitary limit $\frac{2e^2}{h}$ for perfectly symmetric coupling $\Gamma_L = \Gamma_R$. We will discuss what happens to the zero-bias conductance at finite temperatures in Sec. 2.4.4.

We note that Eq. (2.11) can be generalized to finite bias, as shown by Meir and Wingreen [24], and the current can be calculated according to the form

$$I = \frac{e}{h} \sum_\sigma \int dE \, \frac{\Gamma_L \Gamma_R}{\Gamma_L + \Gamma_R} A_\sigma(E) \left[ f(E - \mu_L) - f(E - \mu_R) \right]. \tag{2.14}$$

**Landauer formalism**

We can also treat the Kondo conductance as a transmission problem, within the framework of the Landauer formalism. There, the electrons incident on the dot experience potential scattering, so the $S$-matrix, which relates the outgoing amplitudes in terms of the incoming amplitudes, will reflect the associated phase

shifts. This is diagonal in the Glazman-rotated basis

$$S_\sigma = \begin{pmatrix} e^{2i\delta_{1,\sigma}} & 0 \\ 0 & e^{2i\delta_{2,\sigma}} \end{pmatrix}. \tag{2.15}$$

Since we are interested in the quantity $\mathbb{S}_{RL}$ (i.e., transmission from the left to right electrodes), we do a unitary transformation $\mathbb{S} = U^\dagger S U$ to rotate the scattering matrix back to the $L$-$R$ basis using Eq. (2.6):

$$\mathbb{S}_\sigma = \frac{1}{|t_L|^2 + |t_R|^2} \begin{pmatrix} e^{2i\delta_{1,\sigma}}|t_L|^2 + e^{2i\delta_{2,\sigma}}|t_R|^2 & (e^{2i\delta_{1,\sigma}} - e^{2i\delta_{2,\sigma}})t_L t_R^* \\ (e^{2i\delta_{1,\sigma}} - e^{2i\delta_{2,\sigma}})t_L^* t_R & e^{2i\delta_{2,\sigma}}|t_L|^2 + e^{2i\delta_{1,\sigma}}|t_R|^2 \end{pmatrix} \tag{2.16}$$

Fisher and Lee [25] showed that conductance in the Landauer formalism is

$$G = \frac{e^2}{h} \sum_\sigma Tr(t^\dagger t) \tag{2.17}$$

from which we can directly calculate the Kondo conductance using Eq. (2.16). Noting that $t = \mathbb{S}_{21} = \mathbb{S}_{RL}$, we have

$$G = \frac{e^2}{h} \sum_\sigma |\mathbb{S}_{RL,\sigma}|^2 = \frac{2e^2}{h} \frac{4\,|t_L|^2 |t_R|^2}{(|t_L|^2 + |t_R|^2)^2} \sin^2(\delta_K), \tag{2.18}$$

where we have defined the phase shift $\delta_K \equiv \delta_1$, noting that $\delta_2 = 0$ since the odd fermionic specie decouples. We can calculate this phase shift by using the Friedel sum rule, which is essentially a charge conservation condition

$$\sum_\sigma \Delta n_\sigma = \sum_\sigma \frac{1}{\pi} \delta_{K,\sigma}. \tag{2.19}$$

For the Kondo effect, we will have on the left-hand side $\Delta n_\downarrow + \Delta n_\uparrow = 1$, as one conduction electron leaves to participate in the screening of a local moment. On the right-hand side, we have $\frac{1}{\pi}(\delta_{K,\downarrow} + \delta_{K,\uparrow}) = \frac{2}{\pi}\delta_K$, giving us a Kondo phase shift of $\delta_K = \pi/2$. By making the substitution $\Gamma_\alpha = 2\pi |t_\alpha|^2 \rho(E_F)$ into Eq. (2.18) we again obtain

$$G = \frac{2e^2}{h} \frac{4\,\Gamma_L \Gamma_R}{(\Gamma_L + \Gamma_R)^2} \tag{2.20}$$

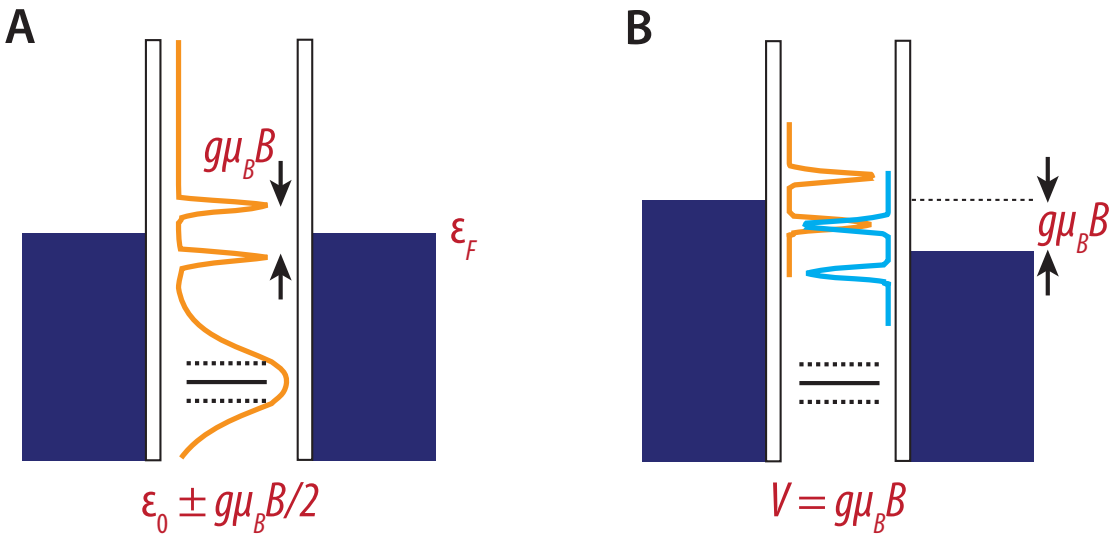


**Figure 2.3:** a) The density of states in the presence of a magnetic field. The localized level undergoes Zeeman splitting $\pm g\mu_B B/2$, as does the Kondo resonance. b) A finite bias $V = \pm g\mu_B B$ can compensate the Zeeman splitting and restore a peak in $dI/dV$, leading to a splitting of the Kondo peak at twice the Zeeman energy.

### 2.4.3 Effect of a magnetic field

A magnetic field alters the Kondo effect by splitting the localized level by the Zeeman splitting, i.e. $\varepsilon_0 \pm g\mu_B B/2$. This in turn also splits the Kondo resonance at the Fermi energy into two peaks with an energy difference of $g\mu_B B$ (see Fig. 2.3a). Since the density of states at the Fermi energy is suppressed by a magnetic field, the linear conductance is suppressed, as we observed in Fig. 2.2d. However, the application of a bias restores peaks in the $dI/dV$ at $V = \pm g\mu_B B$ (Fig. 2.3b), albeit suppressed due to a dissipative lifetime $\tau_\sigma$ from non-equilibrium effects, which has the equivalence of raising the temperature of the system [23]. This leads a splitting in the $dI/dV$ of the Kondo peak by $2g\mu_B B$, twice the Zeeman energy.

The dissipative lifetime mentioned above is a source of decoherence (even for

$T = 0$) when applying bias voltages. For this reason, an estimate of $T_K$ is generally better done using a temperature-dependence measurement than looking at the width of the Kondo resonance. For many single-molecule devices, however, there is reasonable agreement in the $T_K$ extracted from both methods.

**When can you resolve a field-induced splitting?**

In practice, magnetic-field dependence data is somewhat difficult to obtain, and may not be particularly striking for quantitative purposes. For GaAs quantum dots, the $g$-factor is fairly small and the Kondo temperatures are fairly low such that assigning peak positions is not easy, as features become washed out as they move away from zero bias. In single molecules, because the Kondo temperatures are high and the zero-bias peaks fairly wide, the magnetic-field-induced splitting are often not apparent at laboratory magnetic fields (although a suppression in linear conductance is usually discernable). Carbon nanotubes may be the best system for magnetic-field-dependent studies due to reasonably small Kondo temperatures and a $g$-factor close to the free electron value. In terms of theory, calculations of the $T = 0$ spectral functions suggest that the magnetic field splitting should be observable beyond a finite field value $g\mu_B B \simeq 0.5 k_B T_K$ [26].

### 2.4.4 Scaling: connecting the high and low temperature regimes

The temperature dependence of the conductance (resistivity)[1] for a spin-$\frac{1}{2}$ Kondo system had been known for a while in two distinctive regimes: low temperature

[1]Most calculations will produce the Kondo resistivity, as this is the traditional quantity of interest in bulk systems. These resistivities correspond to quantum dot *conductances*, and thus I will call these quantities "conductances."

and high temperature. For the low-temperature regime $T << T_K$, Nozières [27] showed that the Kondo problem has a Fermi-liquid description, and the conductance for the Anderson model is given by

$$G(T) = G(0)\left[1 - c\left(\frac{T}{T_K}\right)^2\right], \tag{2.21}$$

where $G(0)$ is the zero-temperature value of the conductance and $c = \pi^4/16$. In the high temperature $T > T_K$ regime, Hamann used the Nagaoka-Suhl approximation to obtain the conductance [2]

$$G(T) = \frac{G(0)}{2}\left[1 - \frac{\ln(T/T_K)}{\sqrt{\ln(T/T_K)^2 + \pi^2 S(S+1)}}\right]. \tag{2.22}$$

Because $T_K$ is a scaling invariant and the only relevant energy scale, the temperature dependence of all observables in the Kondo regime must be a *universal* function of $T/T_K$, e.g. $G(T) = G(0)\, f(T/T_K)$. This is a very remarkable result in the sense that even if two samples have completely different microscopic properties, their observables can be appropriately scaled by $T_K$ such that the scaled quantities collapse on top of each other, according to a universal function. However, results for the most experimentally relevant regime, $T \sim T_K$, was not known.

This issue was tackled by Costi *et al.* [29], who used the numerical renormalization group (NRG) to calculate the temperature dependence of various transport quantitites. Their results provided deep insight into the intermediate-temperature regime, and described the universal function for conductance for several decades of $T/T_K$. Figure 2.4 shows the universal function obtained from NRG calculations for both the Kondo and Anderson models. The results of the calculations are virtually identical throughout the entire temperature regime. For $T << T_K$, the calculations show the expected Fermi-liquid behavior, and in the high temperature regime $T \gtrsim T_K$ they agree with the Hamann result. There exists some deviation for $T > 10T_K$, but perfect agreement is not expected; the

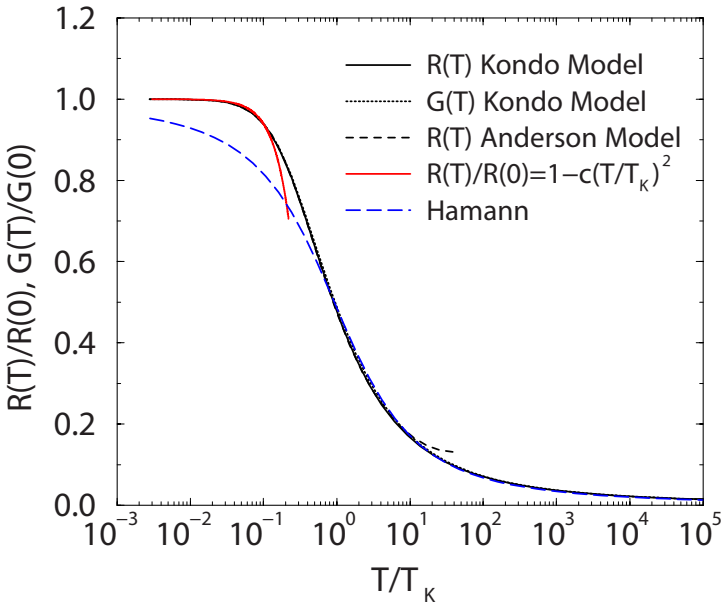


**Figure 2.4:** Universal function $f(T/T_K)$ for conductance in the Kondo regime, adapted from [28]. Numerical renormalization group calculations for the $S = \frac{1}{2}$ Kondo and Anderson models show identical results throughout the entire range of temperatures. They agree with the Fermi-liquid result $f = 1 - c(T/T_K)^2$ at low temperature and the Hamann result at high temperature (see text).

Hamann result is not a $T >> T_K$ assymptote but rather an approximation that is valid for $T > T_K$.

Goldhaber-Gordon *et al.* [30] introduced an analytical form to describe the NRG results, so that they can be compared to experiments

$$G(T) = G(0)\left[1 + \left(\frac{T}{T_K'}\right)^2\right]^{-\alpha_s} = G(0)\, f(T/T_K). \tag{2.23}$$

In the above, $T_K' = T_K/\sqrt{2^{1/\alpha_s} - 1}$ so that the Kondo temperature is defined by $G(T_K) = G_0/2$, as suggested by Costi [29]. The parameter $\alpha_S$ was found to be $\approx$0.22 for the spin-$\frac{1}{2}$ Kondo effect. This leaves only $G(0)$ and $T_K$ as the fitting parameters.

### 2.4.5 The Kondo effect beyond spin-$\frac{1}{2}$

We have thus far focused on a single-level, spin-$\frac{1}{2}$ quantum dot, but a real quantum dot is likely to be a bit more complicated. In this section, we address the basic physics for a multilevel dot, using the $S = 1$ case as a simple example.

What is different in a multilevel dot? First, interaction effects may become important, as we now have to consider the intradot exchange coupling, owing to Hund's rule (cf. the "universal" Hamiltonian [31]). Second, the presence of multiple levels complicates the decoupling scheme that we had used in Sec. 2.3, i.e., the operators cannot be simply rotated in $L$-$R$ space to fully decouple the odd combination of the leads. To see why, let us consider the tunneling term

$$\mathcal{H}_{tun} = \sum_{\alpha\in L,R;\,\nu k\sigma} \left( t_\nu^\alpha c_{\alpha k\sigma}^\dagger d_{\nu\sigma} + t_\nu^{*\alpha} d_{\nu\sigma}^\dagger c_{\alpha k\sigma} \right), \tag{2.24}$$

where the matrix elements $t_\nu^\alpha$ now also depend on the particular dot level $\nu$. In such a case the coupling to the odd channel $J_2$ can be non-zero, as the determinant of the coupling matrix is generally not zero. (Recall that the determinant gives you the product of the eigenvalues $J_1$ and $J_2$.)

$$\det J_{\alpha\alpha'} \propto \sum_{\nu\nu'} \left( t_\nu^L t_{\nu'}^R - t_\nu^R t_{\nu'}^L \right)^2 \neq 0. \tag{2.25}$$

This in turn leads to possibly two screening channels with Kondo couplings $J_1$ and $J_2$, if the localized spins occupy multiple dot levels. This scenario is possible for the case of a spin state $S \geq 1$ on the dot in which Hund's rule exchange favors parallel alignment of spins on the dot (see Fig. 2.5a).

Let us then consider the case for $S = 1$. The Landauer formula for the Kondo conductance gives us [32]

$$G = G_{max} \sin^2(\delta_1 - \delta_2), \tag{2.26}$$

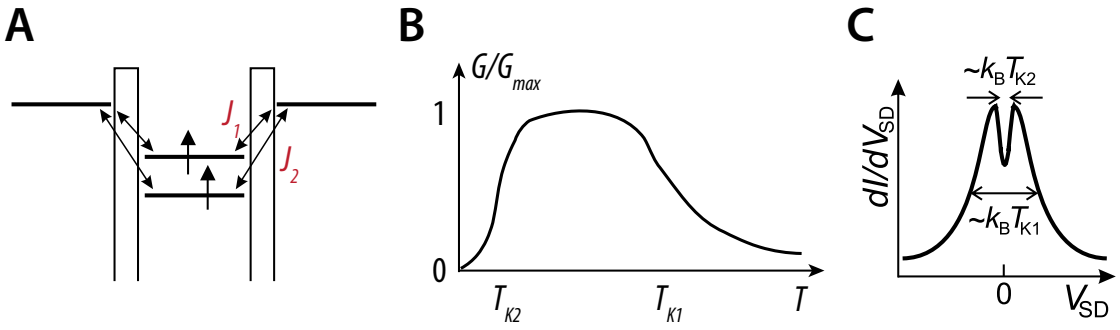


**Figure 2.5:** a) For multilevel dots with $S = 1$, two screening channels with Kondo couplings $J_1$ and $J_2$ are possible, adapted from [33]. b) Temperature dependence of linear conductance. c) Schematic of a $dI/dV$ trace for a two-stage Kondo effect for $T << T_{K_1}, T_{K_2}$, adapted from [33].

where $G_{max}$ is the largest attainable conductance based on geometric considerations, and $\delta_1$ and $\delta_2$ are the phase shifts associated with Kondo couplings $J_1$ and $J_2$, respectively. There will then be two Kondo temperatures $T_{K_1}$ and $T_{K_2}$ associated with each of the screening channels. Recall from Sec. 2.4.2 that according to the Friedel sum rule, the phase shift is $\delta = \pi/2$ in the Kondo regime, and 0 otherwise. This will be helpful in analyzing Eq. (2.26).

**Conductance as a function of temperature**

Let us consider the linear conductance as a function of temperature, assuming that $T_{K_1} > T_{K_2}$. We can divide this into 3 temperature regimes: 1) For $T >> T_{K_1}$ and $T_{K_2}$, there is no Kondo effect, and therefore the linear conductance will not be enhanced. The dot remains in an $S = 1$ state. 2) For $T_{K_2} < T << T_{K_1}$, there will only be a Kondo effect associated with the coupling $J_1$, such that $\delta_1 = \pi/2$ but $\delta_2 = 0$. Therefore, evaluation of Eq. (2.26) yields $G = G_{max}$ within this temperature regime. There still exists a free $S = \frac{1}{2}$, due to only partial screening

of the $S = 1$ state via coupling $J_1$. 3) For $T << T_{K_2}$ and $T_{K_1}$, there are now two Kondo effects in play. Both phase shifts are $\pi/2$, which leads to a suppression in the conductance. Here, the spin on the dot has been fully screened to $S = 0$. These results are summarized in Fig. 2.5b. What this analysis does is show the underlying mechanism behind the "two-stage" Kondo effect (discussed in the next section) in which the $S = 1$ spin state on the dot is first screened to $S = \frac{1}{2}$ and then to $S = 0$ as the temperature is lowered.

**Experimental observations of higher spin Kondo: singlet-triplet, underscreened, and two-stage**

The first set of experimental observations of higher-spin Kondo effects involved Kondo features in an even Coulomb valley, which indicated an integer spin state on the quantum dot. In a vertical GaAs dot [34] as well as in a carbon nanotube [15], a magnetic-field induced Kondo effect (at zero bias) was observed at finite field, thought to occur as the singlet and triplet states of the dot were brought to degeneracy by a magnetic field.

In other experiments, two adjacent Coulomb diamonds showed zero-bias Kondo peaks [35–38], which could be interpreted in terms of an *underscreened* Kondo effect [39]. This situation is probably the most common, as higher-spin Kondo experiments are likely to probe the temperature regime $T_{K_2} << T \lesssim T_{K_1}$. An underscreened Kondo effect occurs because $2S$ channels are required to screen a localized spin $S$ [12], but despite a quantum dot being in an $S = 1$ state, a second screening channel is not accessible at the experimental temperatures. For an underscreened Kondo effect, in which a free $S = \frac{1}{2}$ remains, the ground state is not described by a Fermi liquid, and the low-temperature conductance

does not obey Eq. (2.21), instead going as [28]

$$G(T) = G(0)\left[1 - \frac{b}{\ln(T/T_K)}\right]. \tag{2.27}$$

As a related note, there have been several reports of a gate-induced splitting of a zero-bias Kondo peak within an even Coulomb valley [36–38]. This behavior has been interpreted in terms of a singlet-triplet transition at zero magnetic field, in which the zero-bias peak is due to an underscreened Kondo effect in the triplet state, and the finite-bias peaks are due to excitations from the singlet to nearby triplet states.

Finally, there is a special case: the two-stage Kondo effect, observed when the temperature regime $T << T_{K_1}, T_{K_2}$ can be accessed and the Kondo couplings are similar such that $T_{K_1} \sim T_{K_2}$. While this scenario is the most general in principle, as it simply follows from Fig. 2.5b, obtaining these experimental conditions can be fairly difficult. Thus far, there have been two such experimental observations [33, 40]. The hallmark of a two-stage Kondo effect, as shown in Fig. 2.5c, is a broad Kondo peak of width $\sim k_B T_{K_1}$ in the $dI/dV$ on which there is a dip of width $\sim k_B T_{K_2}$ superimposed. The more common underscreened scenario can be found by considering the limit $T_{K_2} \to 0$.

With this, we complete our discussion of the Kondo effect and move on to a description of our experimental apparatus.

## 2.5 The mechanically controllable break junction

The mechanically controllable break junction (MCBJ) is a remarkably simple instrument that has produced a wealth of beautiful physics [43]. First implemented

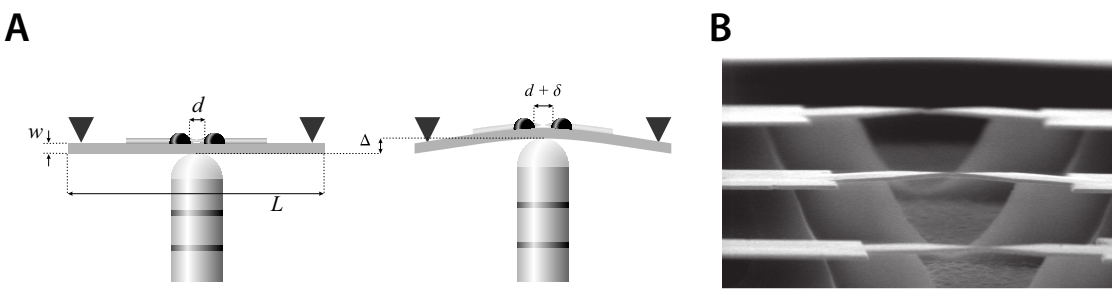


**Figure 2.6:** a) Schematic of the mechanically controlled break junction (MCBJ), taken from [41]. b) Scanning electron micrograph of a nanofabricated MCBJ device, from [42].

by Moreland and Ekin [44] and extended and improved by Muller *et al.* [45], the technique provides a very nice way of controlling the spacing between two electrodes with subatomic precision. The basic idea is to have a suspended wire on a flexible substrate, so that by bending the substrate, the interelectrode spacing can be varied (see Fig. 2.6a). Since this constitutes using a vertical displacement $\Delta$ of the pushing rod to induce a lateral displacement $\delta$ of the electrodes, there is a very large reduction factor $\delta/\Delta$, which is the reason behind the high precision and stability of the MCBJ. This reduction factor is dependent on the length of the beam $L$, the length of the suspended part of the wire $d$, and the thickness of the substrate $w$. For uniform bending, the reduction factor can be expressed as

$$\frac{\delta}{\Delta} \simeq \frac{3wd}{L^2} \tag{2.28}$$

for each electrode. Vrouwe *et al.* have studied the mechanics of bending in MCBJ devices [46]. For devices based on notched wires epoxied to phosphorous bronze substrates covered with Kapton tape, $\delta/\Delta \sim 10^{-3}$, but for nanofabricated devices (Fig. 2.6b), $\delta/\Delta$ can reach $\sim 10^{-6}$, so that picometer precision in the electrode displacement corresponds to a very achievable micron precision in the vertical displacement of the pushing rod. For our devices, the relevant dimensions are

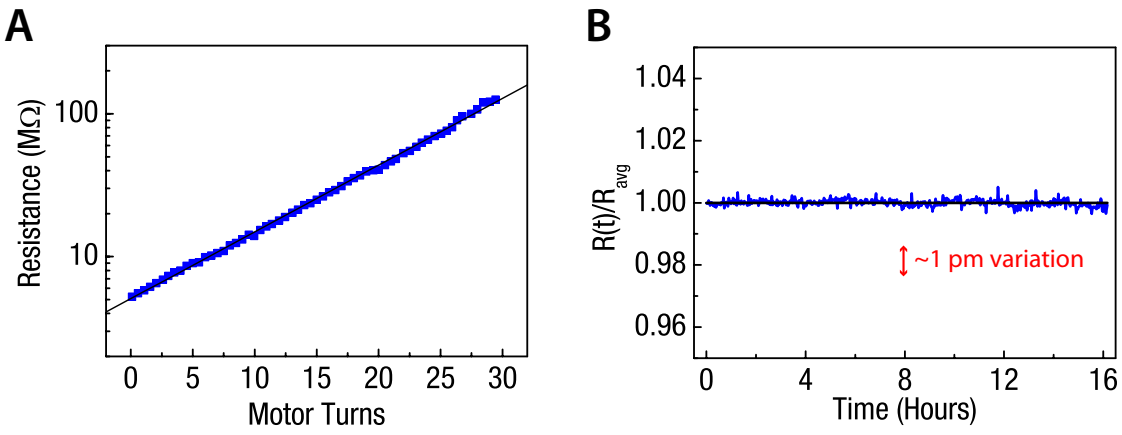


**Figure 2.7:** a) The resistance as a function of electrode displacement is measured and fit to an exponential (see text). b) The junction exhibits remarkably stability when held fixed over the course of 16 hours, showing resistance fluctuations corresponding to less than a picometer variation in electrode displacement.

$w = 200\ \mu$m, $L = 10$ mm, and $d = 500$ nm, which gives us $\delta/\Delta = 3 \times 10^{-6}$.

### 2.5.1 Electrode motion, stability

While Eq. (2.28) provides an estimate for the electrode displacement, in practice, the electrode motion is calibrated by measuring the tunneling resistance as a function of electrode spacing. The interelectrode gap is modeled as a square potential barrier so that the resistance increases exponentially with the width of the barrier

$$R \propto e^{2k\delta} = e^{2\delta\sqrt{2m_e\phi}/\hbar}, \tag{2.29}$$

where $m_e$ is the mass of the electron, and where we use the work function of gold $\phi \simeq 5.1$ eV as the height of the barrier. In our setup, a motor, going through a 100:1 reduction gearbox, cranks a pushing rod consisting of a screw with a pitch

of 1/100 inch. Figure 2.7a shows an example of a calibration curve, showing the exponential increase in the resistance with electrode spacing. The specific calibration can vary from chip to chip, depending on the oxide thicknesses and the etch procedure. We can obtain a calibration of between 2 and 8 pm per motor turn. Because of this fairly wide range, it is critical to decide on a consistent etching procedure.

As pointed out in the previous section, the MCBJ is very stable. Figure 2.7b shows that as the interelectrode gap is held fixed for 16 hours without any feedback mechanism, fluctuations in the tunneling resistance correspond to less than a picometer change in displacement.

### 2.5.2 Fabrication hint: suspending the junctions

Extensive fabrication details for MCBJ devices have been provided in previous theses [47,48], so let us discuss one hint that pertains to suspending the junctions. Traditional lithographic MCBJ devices have a $\sim 1$ $\mu$m layer of polyimide which is etched by an oxygen plasma to suspend the junctions (see, e.g. Ref. [42]). In contrast, our devices were designed such that a heavily-doped silicon substrate could also be used as a back gate, which means that we would like the suspended Au wire to be as close to the substrate as possible. This was achieved using a thin $\sim$ 40 nm $SiO_2$ layer, a thickness that we attempted to push to as low as $\sim$ 20 nm with limited success.

To suspend the junctions, we first used a stainless steel holder that could be immersed in 6:1 buffered oxide etch (BOE) for 60-90 secs to remove the oxide underneath the junction region (of course, all exposed oxide is removed

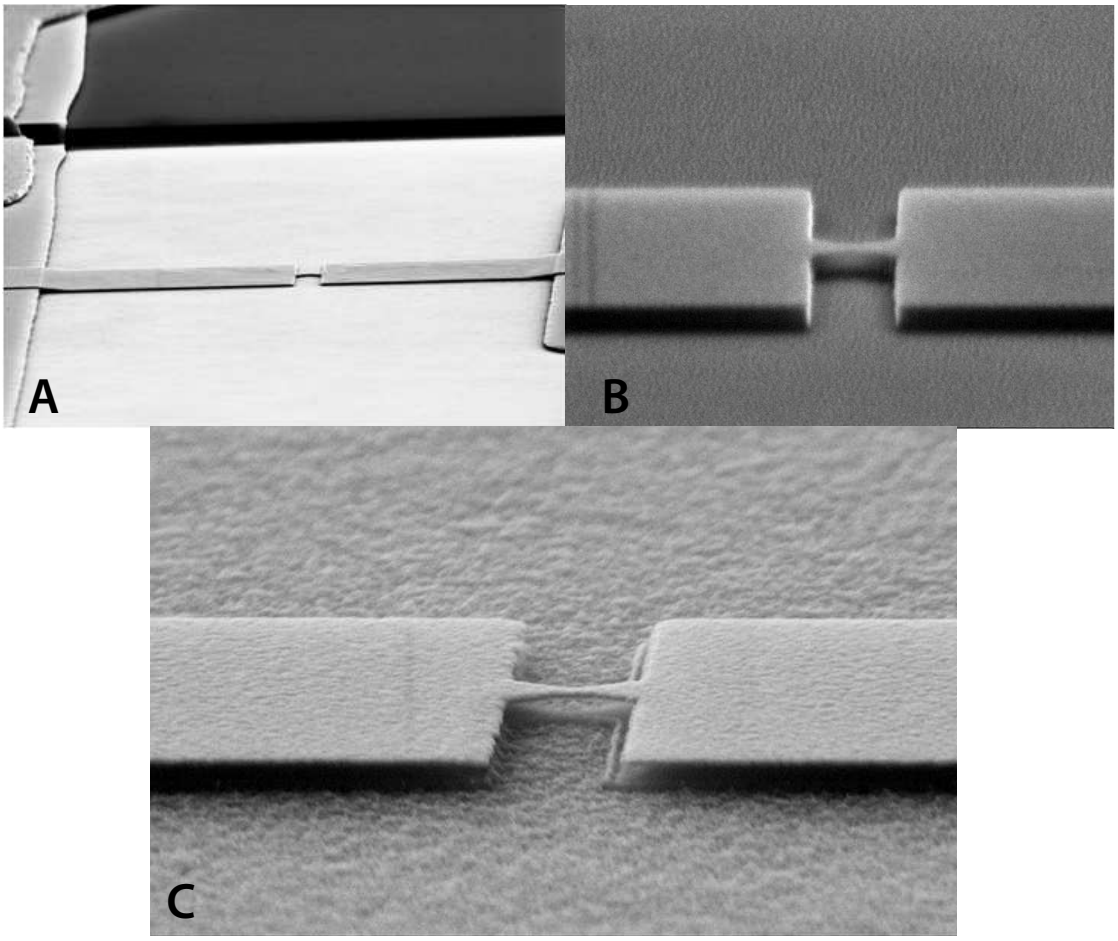


**Figure 2.8:** a) Example of a collapsed bridge that resulted from etching away all of the oxide under the Au wire. One possible way around it: b) Start with a dry anisotropic etch, leaving oxide just underneath the Au wire. c) Do a wet etch in dilute 30:1 BOE to suspend the junction. (As a scale reference, the length of the suspended part is ~ 500 nm.)

too). The holder unfortunately restricted flow of the BOE, and for the 99.999% of people who, like me, are not as careful and as skillful with their hands as Alex Champagne, the restricted flow can lead to some inconsistent etches, thus making reproducibility difficult.

I machined a few teflon holders with an "open-air" design that promoted flow, but this led to a much faster etch rate that made it difficult to remove the

oxide under the junction without removing oxide below the rest of the gold wire, thus leading to collapse of the bridge (Fig. 2.8a). One strategy that was not always employed, but seems to be fairly immune to variations in oxide thicknesses across chips and wafers, is to use a combination of dry and wet etches. The first step is to do a dry anisotropic etch in 30 sccm $CH_3F$ and 0.7 sccm $O_2$ for about 2 minutes to etch the oxide everywhere except underneath the Au wire (Fig. 2.8b). Then, it is followed up with a wet etch in dilute 30:1 BOE to suspend the bridge (Fig. 2.8c). The etch rate for BOE does not seem to go linearly with concentration, and 3 to 4 minutes in 30:1 BOE was required to suspend the junction. I did not stir or agitate the sample during the etch for reasons of reproducibility. As the image in Fig. 2.8c shows, the surface has some fluffy texture. I imagine that the unevenness is due to the slow etch rate of 30:1 BOE, as it tries to remove residual oxide that was left after the dry etch.

## 2.6 Why molecules?

Given that single-molecule devices at low temperature appear to be described by physics similar to that of other systems, the question is raised as to what may be interesting about studying them.

Aside from the technical challenge of fabricating and measuring devices based on single molecules – a task that some may consider to be a worthwhile in its own right – I can think of several reasons, all of which are addressed in this thesis.

First, molecules represent the ultimate limit in the miniaturization of a functional device element. This extreme quantum confinement leads to energy scales

vastly different than those of other systems, thus allowing exploration within these new regimes. Among the consequences are Kondo temperatures that are roughly 2 orders of magnitude larger than those of other quantum dots and large Hund's rule exchange couplings that can readily lead to exotic spin states.

Second, molecules have intrinsic vibrational modes that can couple to electron transport. Studying the electron-vibron coupling has implications in the electrical and mechanical functionality of nanoelectronic devices.

Third, molecules can be fairly symmetric, which leads to various degeneracies. Using a MCBJ enables us to study the evolution of a molecule as some of these symmetries are broken. The effects can include changes in the energies of vibrational modes, spin states, and spin multiplets.

CHAPTER 3

# TUNING THE KONDO EFFECT WITH A MECHANICALLY CONTROLLABLE BREAK JUNCTION

In this chapter, we present measurements of electron transport through $C_{60}$ molecules in the Kondo regime using a mechanically controllable break junction. By varying the electrode spacing, we are able to change both the width and height of the Kondo resonance, indicating modification of the Kondo temperature and the relative strength of coupling to the two electrodes. The linear conductance as a function of $T/T_K$ agrees with the scaling function expected for the spin-$\frac{1}{2}$ Kondo problem. We are also able to tune finite-bias Kondo features which appear at the energy of the first $C_{60}$ intracage vibrational mode. This work, published as *Phys. Rev. Lett.* **99**, 026601 (2007), was done in collaboration with Alex Champagne as well as Abruña group members Geoff Hutchison and Samuel Flores-Torres.

## 3.1 Introduction

The Kondo effect is a many-body phenomenon that can arise from the coupling between a localized spin and a sea of conduction electrons. At low temperature, a spin-singlet state may be formed from a localized spin-$\frac{1}{2}$ electron and the delocalized Fermi sea, leading to a correlated state reflected in transport as a zero-bias conductance anomaly [11, 49]. This feature has been observed in devices containing lithographically-defined quantum dots [13, 14], carbon nanotubes [15], and single molecules [16,17,50,51]. Other more exotic Kondo effects involving higher spin states [33, 34, 36, 40], non-equilibrium effects [52, 53], and orbital degeneracies [7] have also been observed.

While the Kondo effect has been intensely studied, previous experiments on nanotubes and molecules have lacked control over the molecule-electrode coupling. Here, we address the influence of coupling on transport in the Kondo regime by tuning the Kondo effect in $C_{60}$ molecules with a mechanically controllable break junction (MCBJ) [43,54]. By varying the electrode spacing, we show that both the Kondo temperature $T_K$ and the magnitude of the zero-bias conductance signal associated with the Kondo resonance are modified. These changes allow a determination of how the motion modifies the relative coupling of the molecule to the two electrodes. The normalized linear conductance exhibits scaling behavior as expected within the theory of the Anderson Model. The same devices can also exhibit finite-bias inelastic Kondo features at an energy that corresponds to the lowest-energy intracage vibrational mode of $C_{60}$. Changes in electrode spacing can tune the energy and amplitude of these signals.

## 3.2 Experimental details

### 3.2.1 Device fabrication

Our devices consist initially of continuous gold lines (32 nm thick, 500 nm long, and with a minimum width of 50 nm) suspended 40 nm above a 200 $\mu$m thick Si wafer [55] (Fig. 3.1a). Before incorporating $C_{60}$ molecules, we clean unbroken wires in an oxygen plasma (1 min at 30 mtorr, 0.25 W/cm$^2$) to remove any organic contaminants. We then deposit 25 $\mu$L of a 100 $\mu$M solution of $C_{60}$ in toluene, wait 1 minute and blow dry. We cool the samples to 1.6 K. The range of motion permitted by bending the Si substrate is generally too small

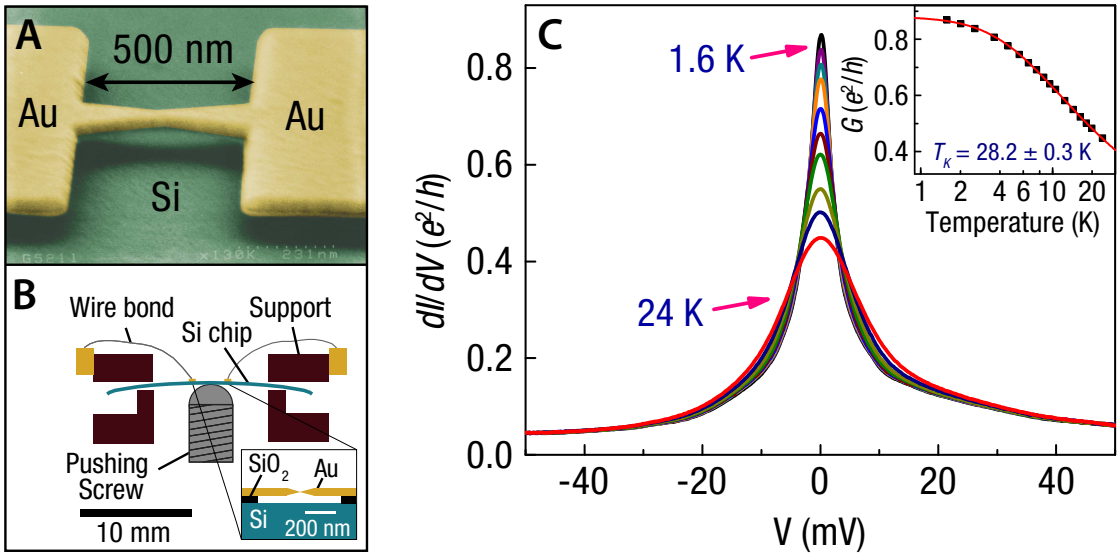


**Figure 3.1:** a) Scanning electron micrograph of a Au bridge suspended 40 nm above a Si substrate. b) Schematic of the MCBJ apparatus. c) $dI/dV$ traces of Device A at various temperatures. Inset: A fit of the linear conductance to the NRG interpolation function (Eq. (3.1)) yields a Kondo temperature of 28.2 ± 0.3 K.

to break the Au wires by mechanical motion alone, so we use electromigration to create a molecular-scale break in the wires before beginning studies as a function of mechanical motion [56]. We minimize the series resistance in our circuit during the electromigration process (the total series resistance is ≈6 Ω) and ramp a voltage stepwise until the resistance of a Au wire begins to change with time at constant $V$. This occurs consistently for $V$≈650 mV. We then hold $V$ fixed until the wire breaks. After electromigration, we find that one or a few molecules can sometimes (~20% of 194 devices studied) be found bridging the gap between electrodes, as inferred from the existence of a Coulomb blockade characteristic in the $I$-$V$ curve rather than a linear characteristic typical of bare junctions [16,50]. In approximately 3/4 of devices exhibiting Coulomb blockade, $dI/dV$ displayed a peak at $V$=0, which is a signature of the Kondo effect. We

performed control experiments with more than 200 bare Au junctions as well as 76 junctions treated with toluene but without $C_{60}$, and found a zero-bias feature in <2% of these devices: 3 bare Au junctions and 1 device exposed to toluene.

### 3.2.2 Calibration of electrode motion

We can control the size of the inter-electrode gap in our devices by using a stepper motor attached to a pushing screw to bend the silicon substrate at cryogenic temperatures (Fig. 3.1b). To calibrate the changes in electrode spacing, $d$, we measure the conductance of bare Au junctions as a function of motor turns and fit to the tunneling conductance expression $G \propto \exp(-2d\sqrt{2m_e\phi}/\hbar)$, where $\phi$ = 5.1 eV is the work function of Au. The mean calibration over 14 bare junctions is 6.1 ± 0.4 pm per motor turn; we apply this value to determine electrode displacements in identically-prepared devices containing $C_{60}$.

### 3.2.3 Why $C_{60}$?

We choose to study $C_{60}$ molecules because they are sufficiently durable to survive high temperatures present during electromigration [57] and because previous work on single-molecule $C_{60}$ devices has observed the Kondo effect [50, 51]. Photoemission studies of $C_{60}$ in contact with Au have shown that the molecule tends to gain an electron from the Au due to the molecule's high electronegativity [58], so that in our work $C_{60}$ is likely to often possess an unpaired spin in equilibrium, providing conditions needed for the Kondo effect.

## 3.3 Temperature dependence in the Kondo regime

Figure 3.1c shows differential conductance curves of a $C_{60}$ device (Device *A*) at several temperatures. We observe a prominent zero-bias peak that is suppressed with increasing temperature, in accordance with predictions for the Kondo effect. Shown in the inset of Fig. 3.1c, we fit the linear response conductance as a function of temperature to an interpolation expression [30] that is a good fit to the numerical renormalization group (NRG) result [29] for conductance in the Kondo regime with the addition of a constant background conductance [32],

$$G(T) = G(0)\left[1 + \frac{T^2}{T_K^2}(2^{1/s} - 1)\right]^{-s} + G_{el}, \tag{3.1}$$

using $s = 0.22$, and leaving $T_K$, $G(0)$, and $G_{el}$ as free parameters. Our data are well described by this expression, and we extract $T_K = 28.2 \pm 0.3$ K, $G(0) = 0.876 \pm 0.009\ e^2/h$, and $G_{el} = 0.042 \pm 0.006\ e^2/h$. The value for $T_K$ also agrees with that obtained by setting the full-width at half maximum of the base temperature zero-bias peak ($5.14 \pm 0.06$ mV) to $2k_BT_K/e$ [15,22], yielding $T_K \sim 30$ K.

## 3.4 Evolution of the Kondo resonance with electrode spacing

Figure 3.2 displays the evolution of the zero-bias peak as we vary the electrode spacing for Device *A* (Fig. 3.2a) and for Device *B* (Fig. 3.2b). For each electrode spacing, we can determine the Kondo temperature from the FWHM of the zero-bias resonance, and we can also deduce the relative coupling $\Gamma_M/\Gamma_L$ of the molecule to the more- and less-strongly coupled electrode based on the magnitude of the linear conductance near $T = 0$ [11,49]

$$G = \frac{2e^2}{h}\frac{4\,\Gamma_M\Gamma_L}{(\Gamma_M + \Gamma_L)^2} f(T/T_K) + G_{el}. \tag{3.2}$$

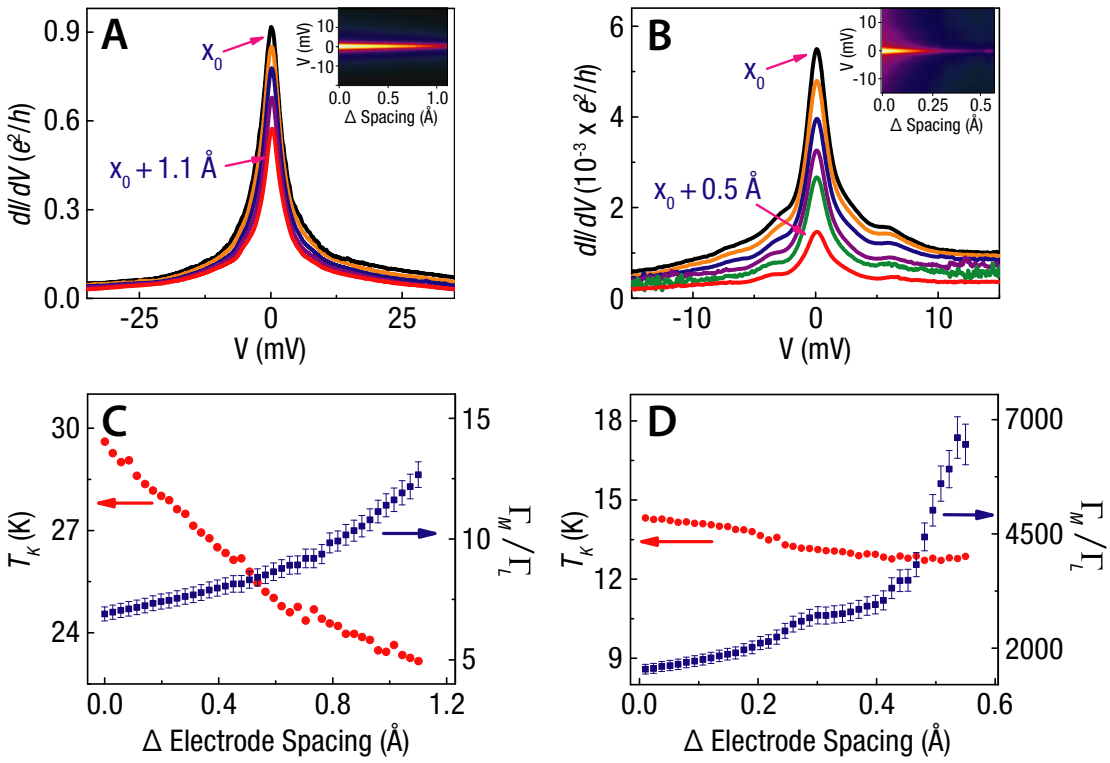


**Figure 3.2:** $dI/dV$ traces of a) Device $A$ and b) Device $B$ at various electrode spacings for $T = 1.6$ K. Insets to a) and b): $dI/dV$ (in color scale) as a function of bias voltage and electrode spacing at $T = 1.6$ K. c,d) The Kondo temperature and the relative coupling $\Gamma_M/\Gamma_L$ as a function of electrode spacing for Devices $A$ and $B$ at $T = 1.6$ K. The uncertainty in the determination of the Kondo temperatures is smaller than ±0.4 K.

To describe the dependence on $T$, we adopt Eq. (3.1) and use $f(T/T_K) = \left[1 + T^2/T_K^2(2^{1/s} - 1)\right]^{-s}$ with $s = 0.22$. The value of the background conductance is determined from fits of the $dI/dV$ as a function of $V$ to a Lorentzian plus a constant. The low value of the peak conductance of Device $B$ indicates that the molecule is coupled quite asymmetrically to its electrodes. In figures 2c and 2d, we plot the evolution of the Kondo temperature and relative coupling as a function of electrode spacing for Devices $A$ and $B$.

We find that as the electrode spacing is varied, $\Gamma_M/\Gamma_L$ increases by ≈330% for

a displacement of 0.55 Å in the asymmetrically-coupled Device $B$, while the increase is just ≈80% over a larger displacement of 1.1 Å in the more-symmetrically coupled Device $A$. This suggests that as the electrodes are pulled apart, the molecule in Device $B$ remains well-coupled to one of the leads so that the motion affects primarily $\Gamma_L$, whereas in Device $A$, $\Gamma_M$ and $\Gamma_L$ are both modified, although not exactly equally. The background conductance $G_{el}$ is always $\leq 0.045$ $e^2/h$ in Device $A$ and $\leq 6.4 \times 10^{-4}$ $e^2/h$ in Device $B$, and decreases by approximately a factor of 10 with 1.1 Å motion in Device $A$, and by approximately a factor of 3 over 0.55 Å motion in Device $B$.

In the more-symmetric Device $A$, the Kondo temperature can be tuned from ≈30 K to ≈23 K as the inter-electrode spacing is increased, whereas in asymmetric Device $B$, the Kondo temperature remains within a narrow range of 13-14 K. We can analyze these changes using the Haldane expression for the Kondo temperature in the limit of large charging energy $U$ [21],

$$T_K = \frac{\sqrt{\Gamma U}}{2} e^{\pi\varepsilon_0(\varepsilon_0+U)/\Gamma U} \sim e^{\pi\varepsilon_0/\Gamma} \tag{3.3}$$

where $\Gamma = \Gamma_M + \Gamma_L$ and $\varepsilon_0$ is the energy relative to the Fermi level of the localized state that produces the Kondo effect. We can expect both $\Gamma$ and $\varepsilon_0$ to vary as a function of electrode spacing: $\Gamma$ because the coupling of the molecule to at least one of the electrodes must decrease as the electrodes are moved apart and $\varepsilon_0$ because break junctions generally exhibit large built-in electric fields even when $V$=0, so that motion of the electrodes produces a gating effect on energy levels in the molecule [55]. If $\Gamma_M$ and $\Gamma_L$ are significantly asymmetric, then varying the electrode spacing will likely have little effect on the overall $\Gamma$, as only the weaker coupling may change significantly. This regime applies to Device $B$, where the coupling ratio always exceeds 1500. The observation of only a small change in $T_K$ as a function of electrode displacement for Device $B$ is consistent

with this picture. For Device $A$, we cannot distinguish the relative contributions of changes in $\Gamma$ and $\varepsilon_0$ to the tuning of $T_K$, based on our data. In principle, a gate electrode that can independently adjust $\varepsilon_0$ could help to disentangle the effects of adjusting electrode spacing. However, we find that the gate coupling for our device geometry is too weak to adjust $\varepsilon_0$ measurably for devices in the Kondo regime.

## 3.5 Universal scaling of linear conductance

In figure 3.3a, we show the temperature dependence of linear conductance for Device $C$ at several different electrode spacings. In this device, the Kondo temperature could be tuned over a significant range, from 60.3 ± 2.4 K (top curve) to 38.1 ± 1.2 K (bottom curve). In the Kondo regime, the conductance normalized to its zero-temperature value is expected to be dependent solely on $T/T_K$ and thus to exhibit universal scaling behavior. In figure 3.3b, we show that $G(T/T_K)/G(0)$ does indeed exhibit a reasonable collapse onto a function that is in close agreement with the universal function predicted by NRG calculations [29].

The evolution of transport properties as a function of electrode spacing is not always as smooth as we measured for Devices $A$, $B$, and $C$. In other devices, the conductance could exhibit sudden changes, and zero-bias conductance resonances could fluctuate in and out of existence. We ascribe these abrupt changes to motion of the $C_{60}$ molecule within the junction region.

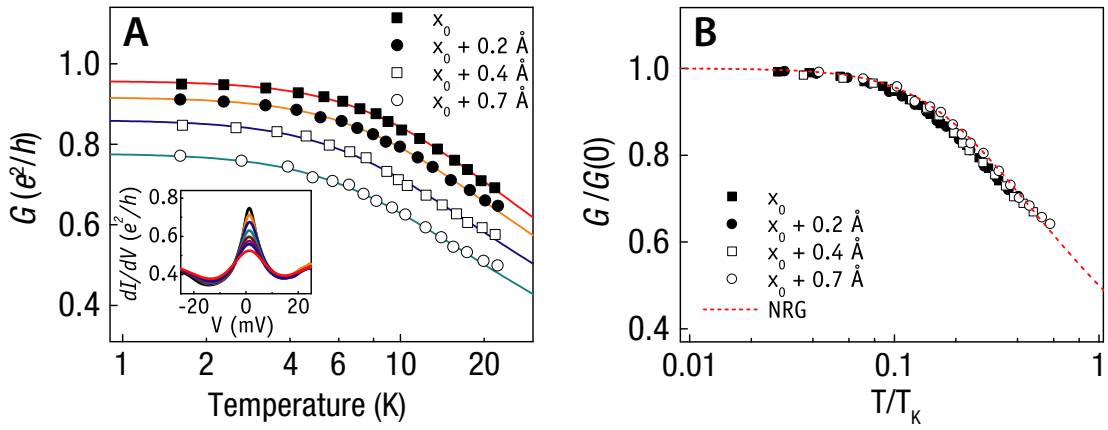


**Figure 3.3:** a) Linear conductance of Device *C* as a function of temperature, fit to the NRG interpolation expression (Eq. (3.1)). The extracted Kondo temperatures are (from the top trace to the bottom): 60.3 ± 2.4 K, 55.5 ± 0.9 K, 45.6 ± 1.9 K, 38.1 ± 1.2 K. Inset: $dI/dV$ traces at $x_0 + 0.7$ Å. b) The normalized conductance, $G(T/T_K)/G_0$, is a universal function of $T/T_K$. Scaled conductance data is compared to the NRG calculation (dotted line).

## 3.6 Tuning vibrationally-induced, non-equilibrium Kondo peaks

In addition to a zero-bias peak in $dI/dV$, in 5 out of 23 devices with Kondo temperatures greater than 20 K we have also observed peaks in $dI/dV$ at symmetric values of $V$ near ±33 mV (specifically, at 29.6, 32.8, 33.5, 36.9, and 37.2 mV in the five devices); see figure 3.4a. We did not observe any other similar features for $|V| < 60$ mV. The energy of 33 meV is known to correspond to the lowest intracage vibrational mode of isolated $C_{60}$, in which the molecule oscillates between a sphere and a prolate ellipsoid shape (Fig. 3.4a, inset) [59]. Previous investigations have shown that molecular vibrations can enhance $dI/dV$ at energies corresponding to vibrational quanta [59–61]. For devices in the Kondo regime, coupling to a vibrational mode has been predicted to result in an inelastic Kondo effect, which is manifested as sidebands in $dI/dV$ at $V \neq 0$ [62].

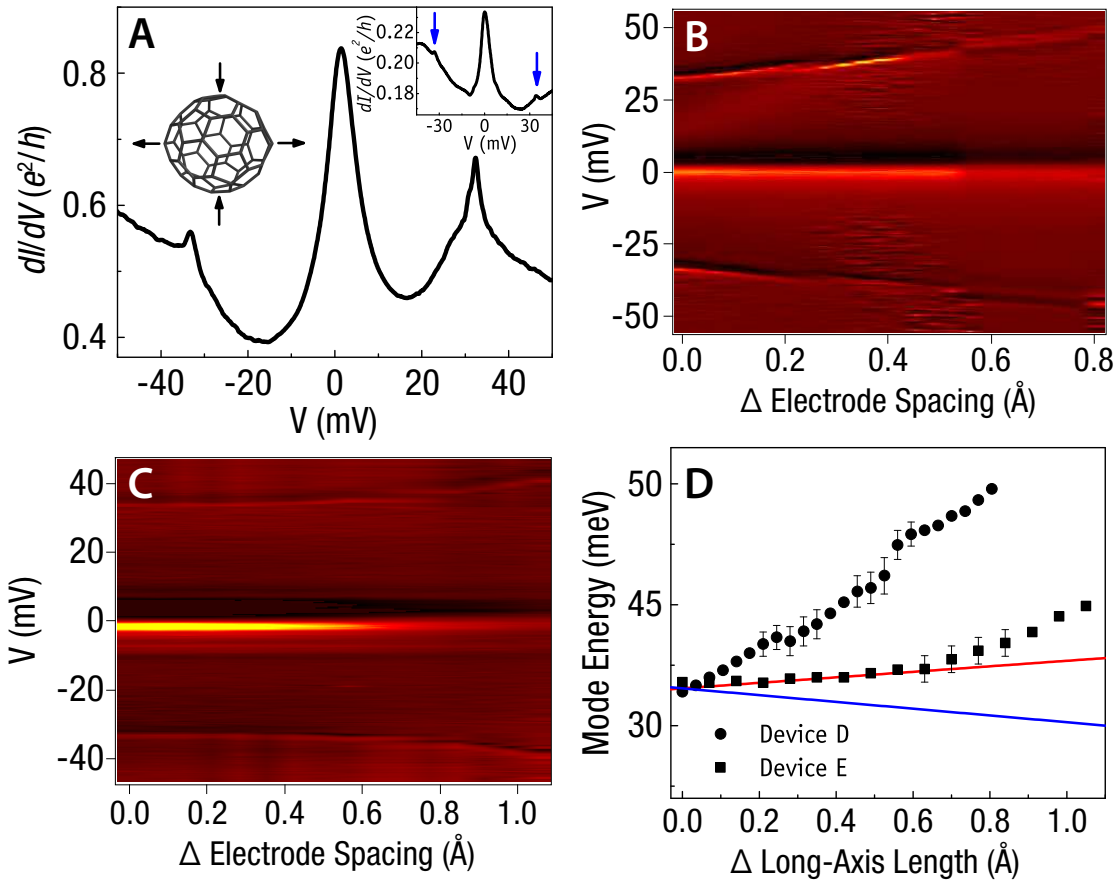


**Figure 3.4:** a) $dI/dV$ for Device $D$ at $T$ = 1.6 K showing satellite peaks near ±33 mV. Left inset: Schematic of the $H_g(1)$ intracage vibrational mode. Right inset: $dI/dV$ for Device $E$ at $T$ = 1.6 K. b, c) $d^2I/dV^2$ as a function of bias voltage and electrode spacing for Devices $D$ and $E$ at $T$ = 1.6 K. d) Stretching dependence of mode energies from Devices $D$ and $E$. Lines: short-axis (negative slope) and long-axis (positive slope) vibrational energies calculated using the PM3 semiempirical method.

Finite-bias features in the Kondo regime have been observed in single-molecule transistors coupled to a vibrational mode [16,50,63], in quantum dots coupled to an applied microwave field [64], and in quantum dots due to Kondo screening of excited states [36,53,65].

Figures 3.4b and 3.4c show $d^2I/dV^2$ for Devices $D$ and $E$ as a function of bias

voltage and electrode spacing. Consistent with what we found for Devices *A* and *B*, as the electrodes are pulled apart the magnitude of the zero-bias peak decreases more strongly in the less-symmetrically coupled (lower conductance) Device *E* than in the more-symmetrically coupled Device *D*. The strength of the sidebands is also different in the two devices; the satellite peaks are significantly more prominent in the more-symmetrically coupled Device *D* compared to the less-symmetrically coupled Device *E*, as predicted in Ref. [62]. As the electrode spacing, and hence the coupling asymmetry, is increased, the amplitude of the non-equilibrium peaks decreases in Device *D*, but the small peaks of Device *E* do not seem to be strongly modified. In both devices, the positions of the inelastic features increase in $|V|$ as the electrodes are pulled apart, suggesting that the mechanical motion increases the energy of the active vibrational mode.

The changes in vibrational frequency as a function of mechanical motion are larger than what we anticipated based on molecular modeling. We performed calculations in GAUSSIAN03 using the PM3 semiempirical Hamiltonian, which has been accurate in predicting the vibrational frequencies of fullerenes [66]. The geometries and harmonic frequencies were calculated under $C_{2h}$ symmetry using the native structure and by setting distance constraints on two atoms at opposite ends of the neutrally charged $C_{60}$ cage to define the long axis from the native length of 7.092 Å to 7.792 Å. The calculations indicate that the five-fold degenerate $H_g(1)$ mode at 33 meV is broken upon distortion into a set of two nearly-degenerate "short-axis" modes (involving motion perpendicular to the direction of stretching) which decrease in energy as the molecule is stretched and three "long-axis" modes which increase in energy (Fig. 4d). Only increases in energy are observed experimentally; we speculate that the long-axis modes may couple more strongly to electron transport. If we assume that the increase

in molecular diameter is equal to the increase in the electrode spacing, so as to determine an upper limit for the estimated frequency shift, then we find that the measured shift for Device *E* is comparable to the calculated frequencies of the long-axis modes, with the main deviations coming at large molecular diameter. However, the peak positions in the more-symmetrically coupled Device *D* shift more strongly than predicted, by roughly a factor of 10. This discrepancy suggests that more rigorous theoretical work may be needed to understand electron-vibration coupling in single-molecule systems, when including coupling to the electrodes and the Kondo effect.

## 3.7 Summary and acknowledgements

In summary, we have demonstrated how the Kondo effect is modified by tuning the spacing between electrodes in mechanically controllable break junction devices containing $C_{60}$ molecules. We measure changes in both the Kondo temperature and zero-bias conductance that are in good accord with theoretical expectations and that allow us to characterize how the mechanical motion changes the relative coupling of the molecule to the electrodes. We have also observed and tuned finite-bias Kondo features which appear at energies corresponding to an intracage vibrational mode of $C_{60}$. We find that the vibrational energy can change more strongly as a function of stretching than predicted by a simple semiempirical Hamiltonian.

We thank D. Goldhaber-Gordon, P. Brouwer, and A. Pasupathy for discussions, and K. Bolotin, F. Kuemmeth, and J. Grose for discussions and experimental help. JJP thanks the NSF for graduate fellowship support. This work

was supported by the NSF (DMR-0244713, CHE-0403806, DMR-0605742), the NSF/NSEC program through the Cornell Center for Nanoscale Systems, and through use of the Cornell Nanoscale Facility/NNIN.

## 3.8 Addenda

The following is intended to provide the reader with some enrichment and an update on a few developments since the completion of the experiments.

### 3.8.1 Electron-vibron coupling in $C_{60}$: which modes?

We discuss simple group theory arguments for which vibrational modes of $C_{60}$ might couple well to transport, particularly for the $C_{60}^{-}$ anion that we measured in the Kondo experiments. These arguments bring to light (somewhat) the observations in our work as well as those of other research groups.

We will be using a little bit of group theory language, and before we begin, I would like to point out the naming scheme for symbols like $T_{2g}$, which refer to the irreducible representations: $A$ stands for a non-degenerate representation, $E$ for 2-fold degenerate, $T$ for 3-fold degenerate, $G$ for 4-fold degenerate, and $H$ for 5-fold degenerate. The subscripts refer to the parity with respect to a center of inversion, with $g$ for even and $u$ for odd; these letters can be traced back to their German origin, namely *gerade* and *ungerade*. The subscript numbers refer to whether there is symmetry or antisymmetry with respect to a non-principal rotation axis.

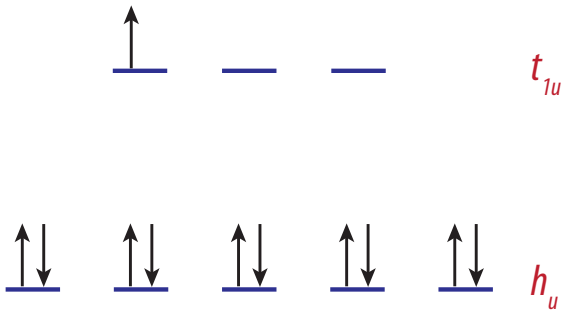


**Figure 3.5:** Energy levels and electron filling for $C_{60}^-$. Because of the Jahn-Teller effect, the electron in a $t_{1u}$ level couples to a normal mode of the molecule. Calculations suggest that the strongest-coupled mode is the one of lowest energy, namely the $H_g(1)$ "squashing" mode.

To understand the vibrational features that may appear in transport, we can begin by considering all the normal modes of a $C_{60}$ molecule. Because there are 60 atoms, we expect that $3N$ - 6 = 174 vibrational modes exist, nearly all of which are less than 200 meV in energy. The burning question, then, is which of the vibrational modes might show strong electron-vibron coupling. A possible solution is to consider the vibrational modes within a particular energy window and explicitly calculate Franck-Condon factors, as was done in Ref. [61]. However, symmetry considerations enable us to narrow down our search very quickly, as we will discuss below.

Based on the icosohedral symmetry of $C_{60}$, the full list of vibrations and their corresponding symmetry types is [67]

$$2A_g \oplus 3T_{1g} \oplus 4T_{2g} \oplus 6G_g \oplus 8H_g \oplus A_u \oplus 4T_{1u} \oplus 5T_{2u} \oplus 6G_u \oplus 7H_u. \qquad (3.4)$$

We have already neatly grouped the 174 normal modes into those corresponding to 46 different energies. The next insight comes from the symmetry of the relevant orbitals. Figure 3.5 depicts the electron filling for the highest-two energy levels in a $C_{60}^-$ anion. Due to the electronic degeneracy associated in

the filling of the $t_{1u}$ orbitals, there will be a Jahn-Teller distortion in which the electron in a $t_{1u}$ level couples strongly to a normal mode of the molecule. While we have invoked an argument involving Jahn-Teller vibron coupling, the group theory principles presented (below) will apply more generally because for $C_{60}^{n-}$, where $n$ = 0-6, transport may involve electrons hopping on and off the "LUMO" level, which is of $t_{1u}$ symmetry.

The basic idea is that for a vibrational mode to couple to an electronic state, the following 2 requirements must be met: 1) the mode is of even parity (to guarantee that the normal mode is vibrational rather than a translational) and 2) the decomposition of the Kronecker product $[\Gamma \otimes \Gamma]$ contains the irreducible representation of the vibrational mode. Without further ado, we will present the one-line solution. We can read off a group theory table (e.g., in Ref. [68]) the Kronecker products of irreducible representations in icosohedral symmetry, and find that

$$t_{1u} \otimes t_{1u} = A_g \oplus T_{1g} \oplus H_g. \tag{3.5}$$

The above result tells us that we need to only consider a small subset of the modes, namely those of $A_g$, $T_{1g}$, and $H_g$ symmetry. We can further narrow down the relevant modes because the $T_{1g}$ modes are antisymmetric, and therefore, cannot couple to the electronic levels. That just leaves the 2 $A_g$ and 8 $H_g$ modes as possibilities. $A_g(1)$ is the radial breathing mode of energy ≈61 meV, and $A_g(2)$ is a mode with energy ≈182 meV in which atoms move towards each of the 5-fold symmetry axes while retaining the radius of the fullerene cage. These $A_g$ modes do not break symmetries that lead to relative orbital shifts, so they will likely couple weakly in a Jahn-Teller active molecule like $C_{60}^{-}$ [69]. The strongest candidates for electron-vibron coupling are then the 8 $H_g$ modes, to which we narrowed down from the original 174 possible normal modes.

**Table 3.1:** Electron-vibron coupling constants in $C_{60}^{-}$, adopted from Ref. [70]

| Mode | Energy (meV) | Calculated couplings $g_k$ | | | |
|---|---|---|---|---|---|
| | | *Negri* | *Schlüter* | *Varma* | *Antropov* |
| $H_g(1)$ | 33 | 0.56 | 0.54 | 0.33 | 0.33 |
| $H_g(2)$ | 54 | - | 0.40 | 0.15 | 0.37 |
| $H_g(3)$ | 88 | - | 0.23 | 0.12 | 0.20 |
| $H_g(4)$ | 96 | 0.22 | 0.30 | 0.00 | 0.19 |
| $H_g(5)$ | 136 | - | 0.09 | 0.23 | 0.16 |
| $H_g(6)$ | 155 | - | 0.15 | 0.00 | 0.25 |
| $H_g(7)$ | 177 | 0.17 | 0.30 | 0.48 | 0.37 |
| $H_g(8)$ | 195 | 0.26 | 0.24 | 0.26 | 0.37 |

There have been a number of theoretical treatments of the electron-vibron coupling in $C_{60}^{-}$. The results from several studies are shown in Table 3.1. Calculations by Negri [71] suggest that the lowest-energy $H_g(1)$ mode is the most strongly coupled, both for the $C_{60}^{-}$ anion as well as for excitations within the neutral $C_{60}$ molecule. Other studies also suggest that the $H_g(1)$ mode has an electron-vibron coupling that is stronger relative to the other modes. Within the range of bias voltages typically applied in a single-molecule device in a lateral geometry, only the $H_g(1)$ and $H_g(2)$ modes are likely to appear in transport. A number of experiments, including ours, have observed the $H_g(1)$ mode [50, 72–74]. The $H_g(2)$ mode has been observed in STM studies [75]. Observations of peaks in the conductance of $C_{60}$ at ~60 mV have been interpreted as the $A_g(1)$ mode [76, 77]. In such a case, the coupling is thought to be dynamic [70]. We have thus far considered an isolated molecule, but within an experimental geometry, there exists an external field as well as broken spatial symmetries due to the presence of metallic electrodes. Recently, this issue has been addressed in an *ab initio* calculation [78], but the conclusions are largely in-line with the material presented:

strong coupling for the $H_g$ modes, but negligible coupling for the $A_g$ modes.

### 3.8.2 Scattering Bethe Ansatz: very preliminary comparisons

In the early 1980's, several physicists including N. Andrei, P. B. Wiegmann, among others, found exact solutions to the *s-d* Kondo model as well as to the Anderson model [79]. Their methods were based on the Bethe Ansatz, which Hans Bethe had used to solve the 1-D Heisenberg model in the 1930's. These exact solutions have yielded new analytical expressions and have been valuable in testing approximate methods for treating the Kondo problem.

Recently, Mehta and Andrei developed a non-equilibrium description of transport in the Kondo regime, called the Scattering Bethe Ansatz (SBA), and examined the interacting resonance level model [80]. In a nutshell, the approach is to first consider a two-lead Anderson impurity Hamiltonian

$$\mathcal{H} = \mathcal{H}_{dot} - i \sum_{j=1,2} \int dx \, \psi_j^\dagger \partial \psi_j(x) + \frac{t}{\sqrt{2}} \left[ \sum_{j=1,2} \psi_j^\dagger(0) d + h.c. \right], \tag{3.6}$$

and to then diagonalize it by constructing single-particle scattering eigenstates, leading to an $N$-particle scattering state $|\Psi\rangle$. The current operator is given by

$$\hat{I} = \frac{ie}{2\hbar} \sum_{j=1,2;\sigma} t_i \left( \psi_{j\sigma}^\dagger(0) d_\sigma - d_\sigma^\dagger \psi_{j\sigma}(0) \right), \tag{3.7}$$

from which the *I-V* characteristics can be found by taking the expectation value: $I(\mu_1, \mu_2) = \langle \Psi; \mu_1, \mu_2 | \hat{I} | \Psi; \mu_1, \mu_2 \rangle$.

Sungpo Chao has used the SBA method to numerically calculate transport quantities using various Anderson model parameters [81]. His results show a universal scaling of differential conductance with bias voltage, i.e.

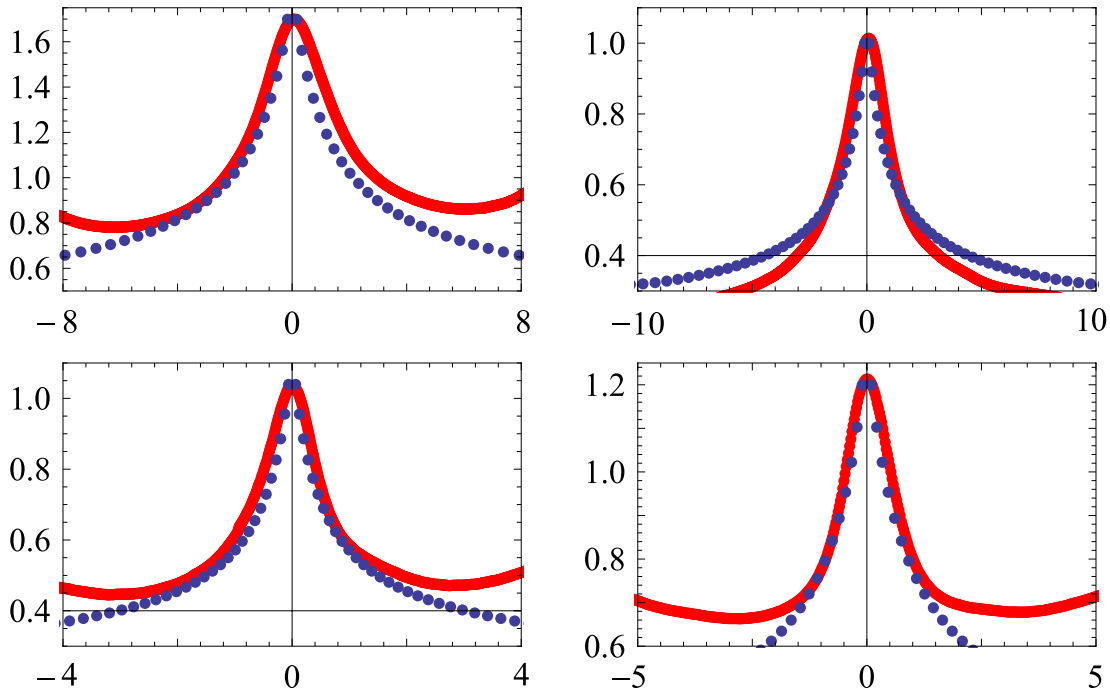


**Figure 3.6:** Very preliminary comparison of SBA calculations to data from four $C_{60}$ devices. The experimental data are shown in red, and the numerical results are shown as blue dots. The left axis for each panel is $dI/dV$ in units of $e^2/h$, and the bottom axis is approximately in units of $eV/k_BT_K$. The calculations show reasonable agreement for $eV$ greater than a few $k_BT_K$.

$G(V) \equiv dI/dV = G(0)f(eV/k_BT_K)$ for up to $eV \sim 8k_BT_K$. He has performed very preliminary comparisons of his calculations to data from our $C_{60}$ devices, assuming $U/\Gamma$=10. The results are shown in Figure 3.6. While the agreement isn't perfect, the SBA results constitute a fairly good description of the experimental results in the low-bias regime, for up to a few $k_BT_K$. As a reference point (while duly noting that non-equilibrium treatments like the SBA are generally more difficult than equilibrium treatments), comparison of experiment to calculated universal scaling curves of linear conductance usually breaks down by $T \sim T_K$.

### 3.8.3 Universal scaling in non-equilibrium transport

We earlier addressed a consequence of $T_K$ being the only relevant energy scale in a Kondo-correlated system: the linear conductance is a universal function of $T/T_K$, i.e. $G = G(0)f(T/T_K)$. One might suspect that there are additional scaling relations with respect to other perturbations such as bias voltage or magnetic field. For the spin-$\frac{1}{2}$ Kondo system, these relations naturally arise since the ground state is a Fermi liquid, which has a characteristic exponent for excitations at low energy, namely the $\propto E^2$ power-law form. In fact, the fitting function that we had used in Eq. 3.1 reduces to a Fermi liquid form $G(T) = G(0)\,[1-c(T/T_K)^2]$ for small $T$. While the quantitative effects of a magnetic field on a Kondo-correlated system are still under debate, analysis of bias-scaling relations has been important in past studies, notably in the identification of two-channel Kondo physics [82, 83]. There, the ground state is not a Fermi liquid, and excitations go as $\sim \sqrt{V}$, $\sqrt{T}$. Returning to the spin-$\frac{1}{2}$ system, Schiller and Hershfield [84] suggested a scaling function of the form

$$F(eV/k_BT) \equiv \frac{G(T,0) - G(T,V)}{AT^2} = \kappa\left(\frac{eV}{k_BT}\right)^2 - \beta\left(\frac{eV}{k_BT_K}\right)^2 + \ldots \tag{3.8}$$

and showed that universal behavior is observed for small $T$ and $V$.

Mike Grobis *et al*. have analyzed the low-energy scaling behavior $G(V,T)$ in a spin-$\frac{1}{2}$ quantum dot [85], and proposed a scaling equation based on the Schiller-Hershfield form

$$G(T,V) = G(T,0)\left(1 - \frac{c_T\alpha}{1 + c_T\left(\frac{\gamma}{\alpha} - 1\right)(T/T_K)^2}\left(\frac{eV}{k_BT_K}\right)^2\right) \tag{3.9}$$

where $\alpha$ characterizes the zero-temperature curvature, and $\gamma$ describes temperature broadening of the Kondo peak. Recently, Scott *et al.* [86] have studied this scaling for single molecules in the Kondo regime and observed universality

for small $V$, but with extracted parameters $\alpha$ and $\gamma$ that deviated from those of Grobis *et al*. In this section, we analyze the data from Fig. 3.1c within this framework.

We first study the power-law exponent for low energies. For small $V$ at fixed $T$, we expect that the conductance will be of the form

$$G(V,T) = G(0,T) - c_V V^P. \tag{3.10}$$

In Figure 3.7a, we plot $G(0,T) - G(V,T)$ for $T$ between 1.58 K and 14.3 K as a function $V$, and fit to the above functional form for $|V| \leq 1$ mV to extract the exponent $P$. The Kondo temperature for this device is ≈28 K. We extract $P = 1.91 \pm 0.07$ within the temperature range explored, a value consistent with the Fermi-liquid exponent of 2 (see Fig. 3.7b).

Having observed the $G \sim V^2$ dependence, we next fit our low-$V$ conductance (Fig. 3.7c) to the form proposed by Grobis *et al.* (Eq. 3.9). The conductance-peak center was slightly offset from $V = 0$ in the raw data due to amplifier drift, and we aligned the peak prior to doing analysis. Extracting the parameters $\alpha$ and $\gamma$ involves a two-dimensional fit, as the parameters cannot be uniquely determined for a fixed $T$. We tackled this by first fitting $\kappa(T) \equiv c_T\alpha/[1 + c_T(\gamma/\alpha - 1)(T/T_K)^2]$, then extracting $\alpha$ and $\gamma$ from fits of $\kappa(T)$ versus $T$. From this analysis, we obtained $\alpha = 0.134 \pm 0.012$ and $\gamma = 0.587 \pm 0.028$. By rescaling our conductance as $[1 - G(V,T)/G(0,T)]/\kappa(T)$ and plotting it versus $\pm(eV/k_BT_K)^2$, we observe that the conductance traces of Fig. 3.7c collapse onto the universal function (Eq. 3.9) for $|(eV/k_BT_K)^2| \lesssim 0.5$, which implies scaling for $V \lesssim 0.7T_K$.

We have yet to do an exhaustive analysis of many devices, but our results are in accord with those of Grobis *et al.*, who found $\alpha = 0.10 \pm 0.02$ and $\gamma = 0.5 \pm 0.1$ for a GaAs quantum dot. They are also in agreement with theoretical calculations

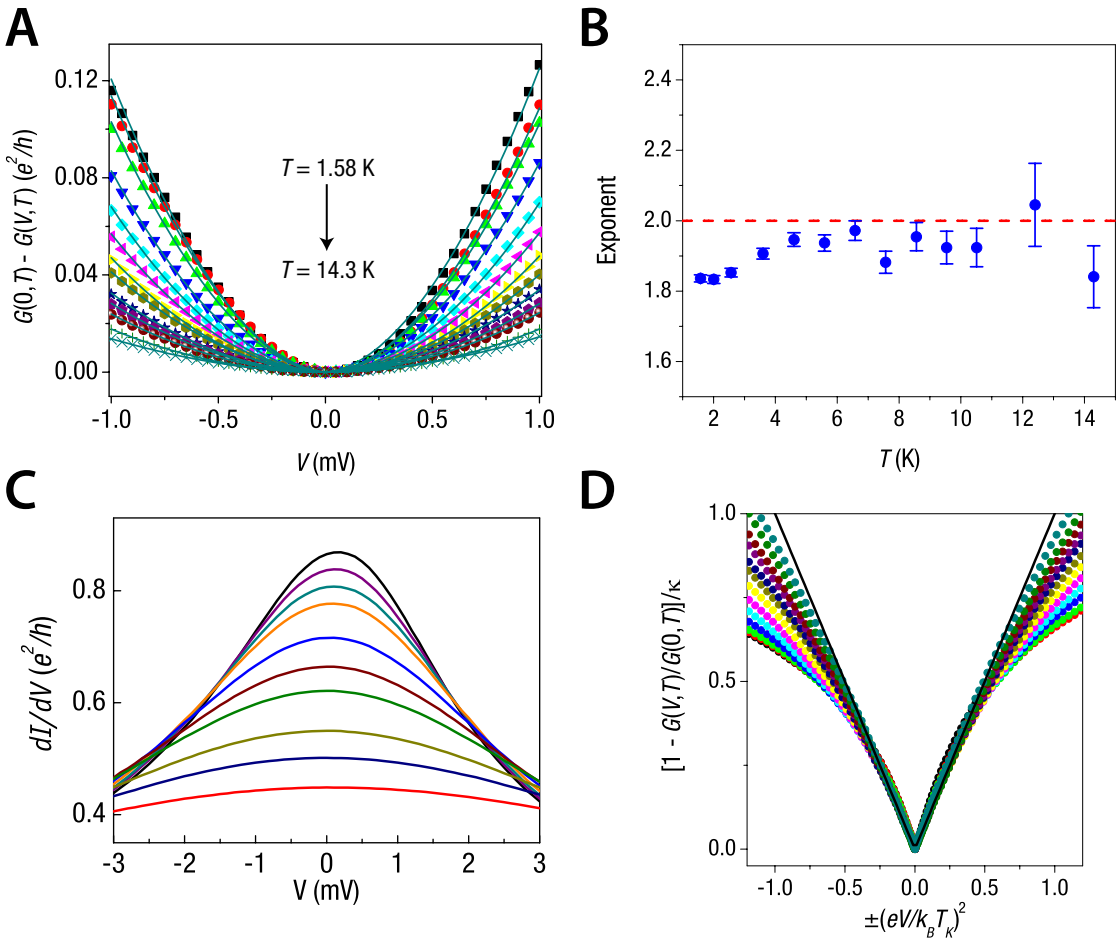


**Figure 3.7:** Scaling behavior in non-equilibrium transport. a) $G(0,T) - G(V,T)$ for a $C_{60}$ device was fit to a power-law form $\propto V^P$ for $|V| \leq 1$ mV and $T = 1.58$ K to 14.3 K. b) Across this temperature range, we obtain $P = 1.91 \pm 0.07$, in good agreement with the characteristic Fermi liquid exponent. c) The differential conductance of the device at low-bias. d) Rescaling the conductance in the form $[1 - G(V,T)/G(0,T)]/\kappa$ results in collapse onto the universal function (Eq. 3.9, shown as a black line) for $eV \lesssim 0.7T_K$.

that suggest $\alpha \approx 0.15$ [85]. Our results, however, differ from those of Scott *et al.*, who obtained $\alpha \approx 0.05$ and $\gamma \approx 0.1$ in single-molecule devices [86]. We do not know the origin of this discrepancy, but a difference in the fitting procedure in their work was the subtraction of a background conductance.

CHAPTER 4

# MECHANICAL CONTROL OF SPIN STATES IN SINGLE MOLECULES

In the previous chapter, we studied the spin-$\frac{1}{2}$ Kondo effect in a $C_{60}$ molecule. We now turn our attention to measurements of a higher-spin Kondo effect in an organometallic cobalt complex, particularly focusing on the effects of a symmetry-breaking distortion. As the molecule is stretched from an initial state in which the complex has an approximately octahedral symmetry to one in which this symmetry is broken, we observe that a zero-bias Kondo peak can split into finite-bias peaks. We determine the initial spin state of the molecule to be $S = 1$ by analyzing the temperature scaling of the Kondo resonance, in the process providing the first quantitative test of predictions for the underscreened $S = 1$ Kondo signal.

## Caveat lector

At this point in time, we have two possible models to explain the stretching dependence of our data: 1) a spin transition from an $S = 1$ triplet state to an $S = 0$ singlet state that occurs as a consequence of the competition between the exchange energy and the Jahn-Teller level splitting produced by the symmetry-breaking deformation, and 2) a tuning of a zero-field splitting in the molecule by geometric distortion. We hope that quantum chemistry calculations, additional analysis, and complementary measurements will provide us with the insight needed to distinguish between these models. In this chapter, however, we will present our data within the context of a singlet-triplet transition, mainly for the aesthetic reason of keeping the discussion clear.

## 4.1 Introduction

Single-molecule transistors have proven to be valuable model systems for studying fundamental quantum-mechanical processes, including Kondo physics [16, 17], electron-vibration coupling [63, 72, 73], and the effects of molecular spin on electron transport [38, 87–89]. Here we demonstrate a new level of quantum control of the spin in a single-molecule system. By connecting single transition-metal complexes within mechanically controllable break junctions [43, 54] that allow us to controllably stretch the molecule while measuring its electrical resistance, we demonstrate that we can change the spin of a molecule by varying its degree of mechanical deformation. One possible explanation for the results may be the mechanism underlying Hunds rule for atomic spins – competition between the exchange energy that favors high spin ($S$) states and level splittings induced by broken symmetries that favor $S = 0$.

## 4.2 Energy levels and dependence on stretching

The molecule that we study is a cobalt bis(terpy-SH) complex with thiol end groups (terpy-SH = 4-mercapto-2,2:6,2-Terpyridine), pictured in Fig. 4.1a, a molecule our group has studied previously using single-molecule devices with stationary electrodes [16]. Related molecules have been examined by other groups [20, 63, 86]. In its neutral form, this complex exists in the $Co^{2+}$ state in a $d^7$ configuration, with a low-spin filling that leads to a ground state spin of $S = \frac{1}{2}$ at low temperature [90, 91]. However, we will present evidence that when attached to metal electrodes in our devices, charge transfer from the electrodes can sometimes also result in the $Co^{1+}$ ($d^8$) being the ground state. It will be the

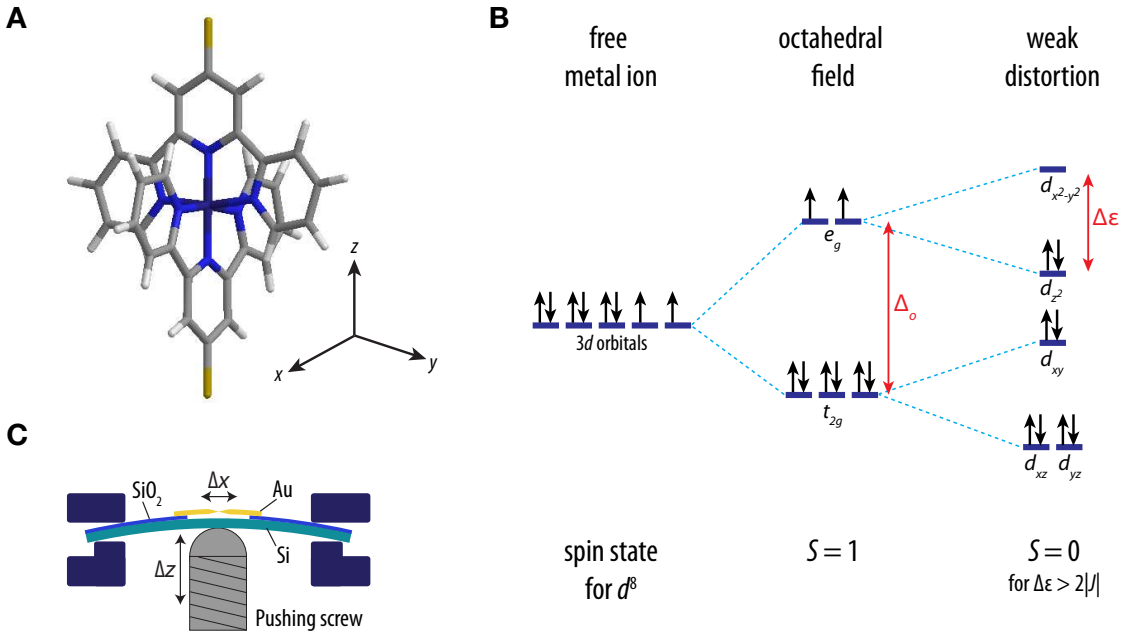


**Figure 4.1:** a) Structure of $[Co(TpySH)2]^{1+}$, a complex with 8 $d$-electrons. b) Energy levels of the complex as a function of stretching along the $z$-axis. c) Schematic of a mechanically controllable break junction device that is used to stretch the molecule.

$Co^{1+}$ state that is of interest for the spin transitions as a function of molecular deformation. The occupation of electronic energy levels for a $d^8$ complex is pictured in Fig. 4.1b. For a free Co ion, the five $d$-orbitals would be degenerate on account of spherical symmetry. When the ion is coordinated by two terpyridine ligands in an unstretched bis(terpy-SH) complex, the local environment of the Co ion has an approximately octahedral symmetry, causing the $d$ levels to be split into a set of three-fold degenerate $t_{2g}$ orbitals and two-fold degenerate $e_g$ orbitals, separated by $\Delta_0 \sim 2$ eV. For the $d^8$ configuration, the higher-lying $e_g$ orbitals must contain two electrons, and when these orbitals are degenerate or near-degenerate the exchange energy ($J\mathbf{S}^2$) can align their spins to produce an $S = 1$ ground state. However, the degeneracy between the $e_g$ orbitals will be broken if the octahedral symmetry of the molecule is distorted. If the distortion-

induced splitting $\Delta\varepsilon$ between the two highest-energy ionic levels is larger than the exchange energy, then both electrons must occupy the lower energy orbital with opposite spins to give an $S = 0$ ground state, with a low-energy excited triplet state higher in energy by $\Delta\varepsilon - 2J$.

## 4.3 Device preparation

We study the low-temperature electron transport properties of these molecules at cryogenic temperatures within mechanically-controllable break junction devices, fabricated by the procedure described in [55,73]. We initially make continuous gold lines (32 nm thick, 500 nm long, and with a 50 nm-wide constriction) suspended 40 nm above a 200 $\mu$m-thick Si wafer. To incorporate the molecules, we clean unbroken wires in an oxygen plasma to remove any organic contaminants and then immerse the chip containing the samples into a 0.2 mM solution of Co bis(terpy-SH) in acetonitrile for 24 hours, allowing the molecules to attach to the gold. After the chip is removed, excess solution is blown off with nitrogen gas, and we cool the sample to 1.6 K. We use electromigration [56] to create a molecular-scale break in the wires before beginning studies as a function of mechanical motion. We can then control the size of the inter-electrode gap in the device, thereby deforming the molecule, by using a stepper motor attached to a pushing screw to bend the silicon substrate at cryogenic temperatures (Fig. 4.1c).

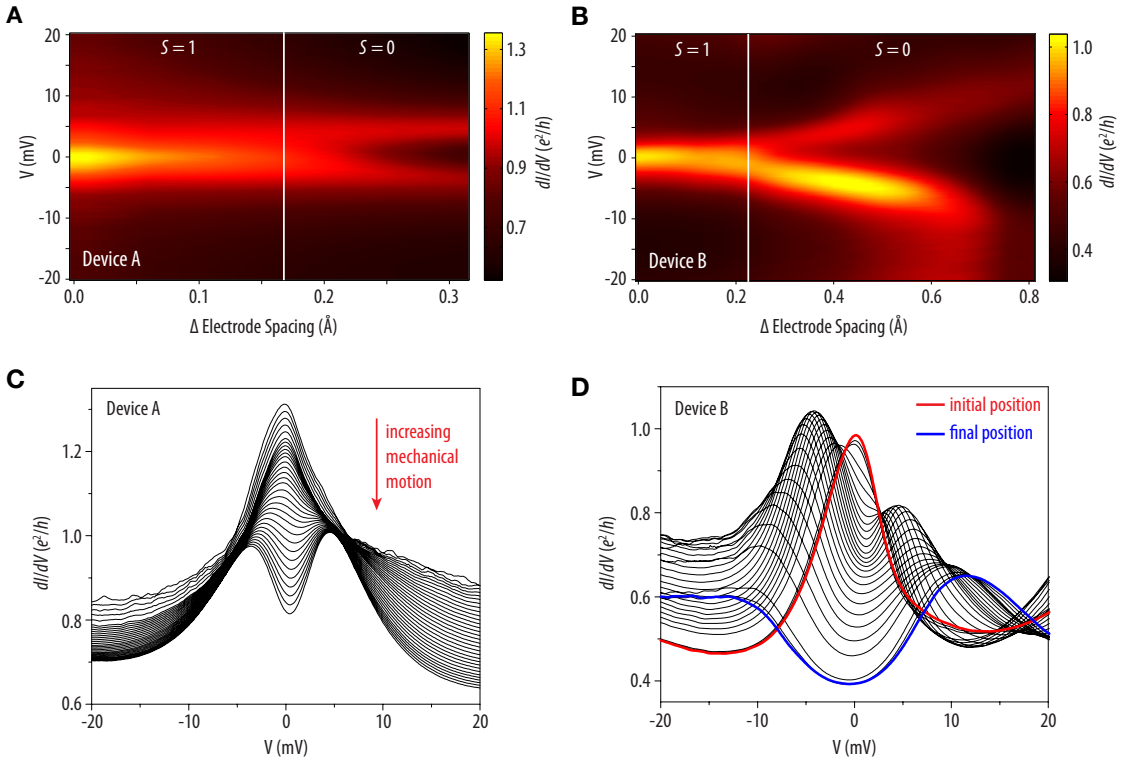


**Figure 4.2:** Evolution of zero-bias Kondo peaks into finite-bias peaks as a function of the mechanical motion of the electrodes at $T$ = 1.6 K for a) device $A$ and b) device $B$. c, d) Individual line traces showing the evolution of the zero-bias peak.

## 4.4 Stretching dependence: singlet-triplet transition?

Measurements of the molecular conductance as a function of increasing the electrode spacing are shown in Fig. 4.2. For these molecules, at the initial position for the electrodes, the differential conductance has a single peak centered at zero voltage, characteristic of Kondo-assisted tunneling via the molecule. In the Kondo effect, at low temperature and small voltage electron spins from the electrodes screen the spin of the molecule and in the process provide a quantum-coherent channel for electron flow through the molecule, thereby enhancing the conductance. The peak conductance for the devices in Fig. 4.2 is between 1 $e^2/h$

and 2 $e^2/h$, consistent with a single molecule strongly coupled to the electrodes to be in the Kondo regime.

As we stretch each molecule using the mechanically adjustable electrodes, we observe that the single conductance peak splits into two beyond a value for the change in electrode spacing that varies from device to device. For the two devices displayed in Fig. 4.2 (as well as for two others), by ramping the electrode spacing up and down we were able to reproducibly cross this transition between one peak and two. For other devices, mechanical motion of the electrodes sometimes resulted in random conductance shifts, sudden changes in peak shape and position, or irreversible changes that destroyed the device. Because of this device sensitivity, we explored a relatively narrow region of mechanical stretching. We also observed peaks that did not split with mechanical motion of the electrodes as well as devices that had split peaks prior to stretching.

The transitions we see as a function of mechanical motion between a single peak and split peaks in the differential conductance are qualitatively similar to measurements as a function of gate voltage in GaAs [36], carbon nanotube [37], and $C_{60}$ [38] quantum dots, which have been attributed to transitions between spin-triplet and spin-singlet Kondo effects for a fixed even number of electrons on the dot. We demonstrate below that our transitions are consistent with a transition between $S = 1$ and $S = 0$ ground states, in our case as a function of mechanical deformation. Because the Kondo temperature scale is significantly higher for our molecular devices than for the previous quantum-dot studies, we can perform the first quantitative tests of predictions for the temperature dependence of the $S = 1$ Kondo signal.

## 4.5 Temperature dependence

The functional forms for the temperature and bias dependence of the conductance due to the Kondo effect are predicted to depend on the spin $S$ of the Kondo impurity (the molecule in our case) and the number of screening channels for electrons in the leads that couple to the impurity. The most-studied case is $S = \frac{1}{2}$, which is fully screened to a many-body spin-zero state by a single screening channel. In general, for an impurity with spin $S$, $2S$ screening channels are required for complete screening [12]. For an impurity coupled to two metal electrodes as in our experimental geometry, there are two screening channels consisting of linear superpositions of orbital states from the two electrodes with, in general, different couplings $J_1$ and $J_2$ to the impurity that result in two Kondo temperature scales $T_{K_1}$ and $T_{K_2}$ [32]. (We assume $T_{K_1} > T_{K_2}$.) The Kondo temperatures depend exponentially on the couplings, so in the typical case $T_{K_1} >> T_{K_2}$. If $S = 1$, as the temperature is reduced to the range $T_{K_2} < T < T_{K_1}$ the result is a regime of an underscreened Kondo effect, in which the original impurity spin is only partly screened (to a value $S - \frac{1}{2}$) by the electrons in the electrodes. At lower temperatures, below both $T_{K_1}$ and $T_{K_2}$, there can be a second state of screening resulting in a two-stage Kondo effect [39, 92]. The underscreened Kondo effect is predicted to produce a much slower rise in the conductance for $T < T_{K_1}$, relative to the more-common fully-screened $S = \frac{1}{2}$ Kondo effect, due to additional logarithmic contributions to the conductance signal [93].

The temperature dependences of our measured conductance signals are shown in Fig. 4.3 at fixed values of electrode spacing. To fit to the theoretical predictions, we begin with curves of conductance as a function of temperature calculated using the numerical renormalization group (NRG) for $S = \frac{1}{2}$, 1, $\frac{3}{2}$,

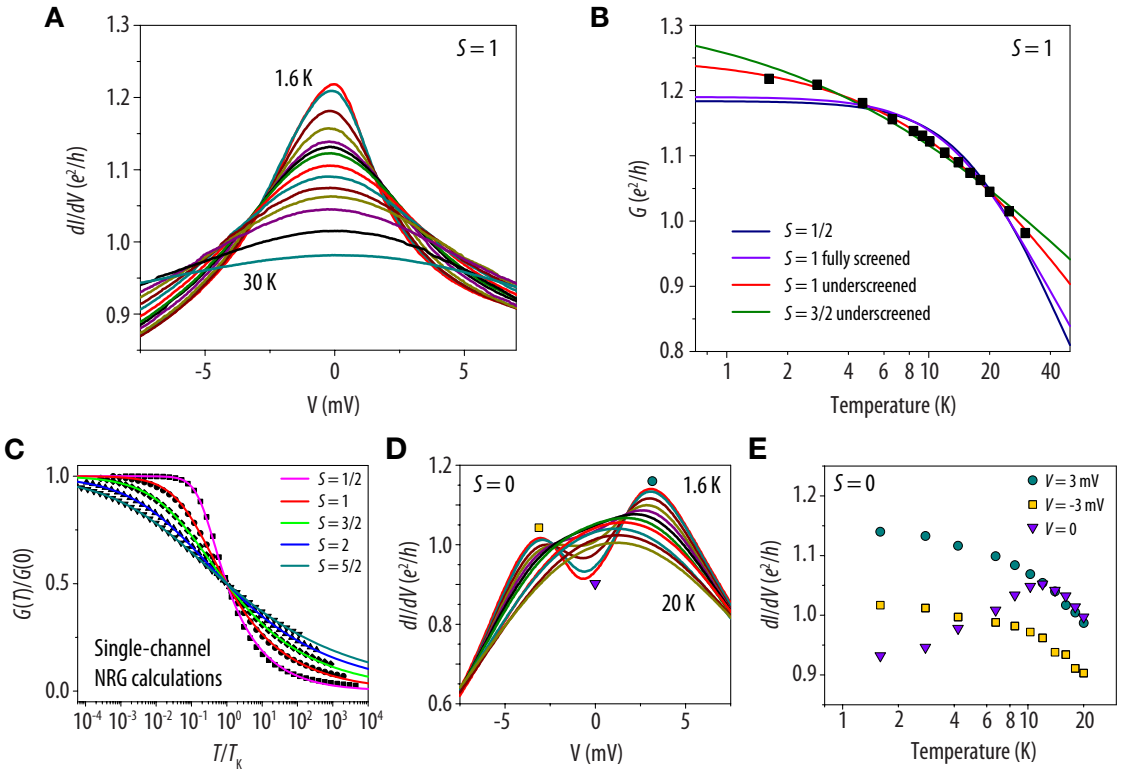


**Figure 4.3:** a) Temperature dependence of $dI/dV$ on the triplet side of the transition. b) Fits of linear conductance as function of temperature on the triplet side to $S = \frac{1}{2}$ and $S = 1$ fully screened, and $S = 1$ and $S = \frac{3}{2}$ underscreened calculations. c) Numerical renormalization group (NRG) calculations of quantum-dot conductances for the case of a single screening channel [94] and fits to Eq. (4.1). d) Temperature dependence of $dI/dV$ on the singlet side of the transition. e) The linear conductance on the singlet side exhibits non-monotonic behavior. The finite bias peaks at $V = \pm 3$ mV show a monotonic decrease.

2, and $\frac{5}{2}$ in the presence of a single screening channel [94] and for $S = 1$ with two screening channels having $T_{K_1} = T_{K_2}$ [95]. In analogy with the common practice in the spin-$\frac{1}{2}$ Kondo literature [30], by fitting to the NRG calculations we then generate an empirical fitting function, finding that a function of the form

$$G(T) = G(0)\left[1 + \left(\frac{T}{T_K'}\right)^{\xi(S)}\right]^{-\alpha_S},$$

provides an excellent fit to all of the NRG curves over orders of magnitude in

temperature, if we use values for the exponents $\xi(S)$ and $\alpha_S$ that depend on $S$ (see Sec. 4.8). In Figure 4.3b we fit the measured temperature dependence of the $V = 0$ conductance of device $A$ to the four different empirical forms: spin-$\frac{1}{2}$, underscreened $S = 1$, underscreened $S = \frac{3}{2}$, and fully screened $S = 1$. We find excellent agreement with the predictions for the underscreened $S = 1$ Kondo case, and significant deviations from all of the other cases, leading us to conclude that the ground state of the unstretched molecule in this device does indeed correspond to $S = 1$.

The temperature dependence for the stretched form of the molecule in device $A$ is shown in Fig. 4.3c. The temperature dependence of the zero-bias conductance is non-monotonic, initially increasing and then decreasing with $T$, in a form that is qualitatively similar to the bias dependence of the conductance, increasing from $|V| = 0$. This is consistent with the expected behavior in the $S = 0$ side of the transition based on calculations by Hofstetter and Schoeller [96].

## 4.6 Magnetic-field dependence

We now turn to the magnetic-field dependence of our devices. On the triplet side, the application of a magnetic field splits the zero bias peak (Fig. 4.4a). Within the model of a triplet-singlet crossing, the position of these peaks correspond to the energy difference of the lowest triplet states $T_-$ and $T_0$ (Fig. 4.4d). On the singlet side, a magnetic field moves the finite-bias peaks together, towards restoring a zero-bias peak (Fig. 4.4b). Here, the position of the peaks corresponds to the energy difference between the singlet and the lowest-energy triplet state $T_-$. While we could not fully restore the zero-bias peak in device $A$, in another

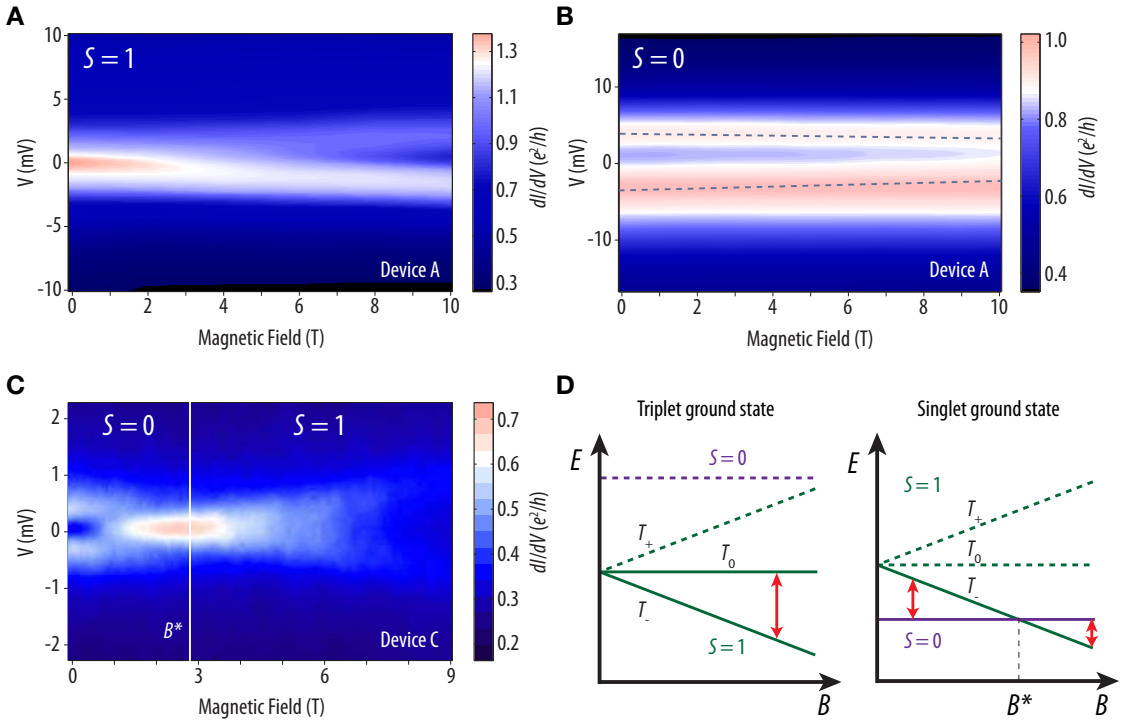


**Figure 4.4:** Magnetic-field dependence of the Kondo peaks. a) On the triplet side, the zero-bias peak splits as a function of magnetic field. b) On the singlet-side, the finite-bias peaks move closer together. c) In one device, we were able to drive a singlet-triplet transition by a magnetic field alone. c) Energy diagrams for the triplet and singlet ground states.

device, we were able to use a magnetic field to drive a transition from a singlet ground state to that of a triplet (Fig. 4.4c). The position of the peaks as a function of magnetic field can be understood in terms of Fig. 4.4d. The split peaks on the low-field side of the transition correspond to the energy difference between the singlet and the lowest-energy triplet state. A zero-bias peak is restored at a critical field $B^*$, which represents the field at which the singlet and lowest-energy triplet states are degenerate. At larger magnetic fields, the triplet becomes the ground state, and the position of the peaks represents excitations to the nearby singlet state. We do not resolve the other possible transitions in our data, in

contrast to recent experiments done at dilution-fridge temperatures [38]. We suspect that the primary reason is due to higher Kondo temperatures, which results in wider peaks; the higher temperature of our measurements may also play a role.

## 4.7 Conclusions and caveats

In this chapter, we have studied the effect of a symmetry-breaking distortion of an organometallic complex in the Kondo regime. As the molecule is mechanically stretched, a zero-bias Kondo peak may split into finite-bias peaks, which might be understood in terms of a singlet-triplet transition induced by the splitting of the $e_g$ orbitals. Temperature-dependence measurements of the unstretched molecule show excellent quantitative agreement with an $S = 1$ underscreened Kondo effect. Temperature measurements on the stretched molecule are qualitatively consistent with theoretical predictions of an $S = 0$ ground state [96]. The magnetic field data are also consistent with a singlet-triplet transition.

As stated at the beginning of the chapter, there exists another possible interpretation that a symmetry-breaking distortion controls the molecule's zero-field splitting. While the singlet-triplet interpretation is elegant and invokes very simple arguments, the zero-field splitting scenario seems to better capture the energy scales observed in the experiment (few meV's). We are currently carrying out calculations (Eric Neuscamman and Garnet Chan), doing further analysis, and thinking about complementary measurements that may provide us with more conclusive insight.

## 4.8 Appendix: Fitting NRG calculations

The goal here was to find a suitable function to describe the temperature-dependent conductances of underscreened Kondo-model calculations. Such a function would be very helpful in comparing experiments to theory and to allow for the extraction of relevant parameters. Note that there is no deep physics behind the proposed fitting form (Eq. (4.1)); it is an empirical function that describes the numerical calculations quite well over almost 7 decades of temperature. It does so by approximating slow, logarithmic corrections in the $T >> T_K$ limit and the slow $(\ln T/T_K)^{-2}$ asymptotic behavior in the $T << T_K$ limit (for underscreened cases) by reducing to a sub-linear form.

### 4.8.1 The spin-dependent universal fitting function

To describe the NRG results for the temperature-dependent conductance of a quantum dot with a Kondo impurity of spin $S$ and in the presence of a *single* screening channel, we seek a universal form $G(T) = G(0)\, f(T/T_K)$. We find that the calculated results are very well-described by the functional form

$$G(T) = G(0)\left[1 + \left(\frac{T}{T_K'}\right)^{\xi(S)}\right]^{-\alpha_S}, \tag{4.1}$$

where $G(0)$, $T_K'$, $\xi(S)$, and $\alpha_S$ are fitting parameters. We note that $\xi(S)$ can be adequately described by a spin-dependent function that we empirically determine to be

$$\xi(S) = \frac{4}{3S(S+1)} + \frac{2}{9}. \tag{4.2}$$

Note that for $S = \frac{1}{2}$, Eq. (4.2) gives $\xi(S) = 2$, the exact Fermi liquid exponent. Fitting experimental data will normally involve just a two-parameter fit of $G(0)$

and $T_K'$ since $\xi$ and $\alpha_S$ should be held at or near the appropriate spin-dependent fitted values, which are listed in Table 4.1.

For the Kondo temperature, we use the definition $G(T_K) \equiv G(0)/2$, which was first suggested by Costi [29] and adopted for quantum dots by Goldhaber-Gordon [30], so that $T_K'$ of Eq. (4.1) represents the actual $T_K$ with an appropriate scaling:

$$T_K' = \frac{T_K}{(2^{1/\alpha_S} - 1)^{1/\xi}}. \tag{4.3}$$

For spin-$\frac{1}{2}$ ($\xi = 2$), the fitting function (Eq. (4.1)) reduces to the usual form [30], but for higher spins, $G(T)$ represents the temperature-dependent conductances for *underscreened* Kondo effects. Theo Costi has calculated NRG resistivities, which correspond to quantum-dot conductances, for a Kondo impurity with spin $S = \frac{1}{2}$, 1, $\frac{3}{2}$, 2, and $\frac{5}{2}$ in the presence of a single screening channel, and made them available to us. The results for $S = \frac{1}{2}$, 1, and $\frac{3}{2}$ were published previously in Fig. 1 of Ref. [94] but were not available in a usable form. More recently, Costi *et al.* have done Anderson model NRG calculations of $G(T)$ for fully screened Kondo effects [95]. The usual spin-$\frac{1}{2}$ fitting function with $\xi = 2$ describes even the $S > 1/2$ fully screened cases very well for an appropriate $\alpha_S$ (see Table 4.1).

### 4.8.2 Fitting procedure and results

The NRG data came in the form of discrete points ($G$, $T/T_0$), where $T_0$ is a convenient theorists' scale defined from the zero-temperature susceptibility of the $S = 1/2$ Kondo model

$$\chi(0) = \frac{(g\mu_B)^2}{4k_B T_0}. \tag{4.4}$$

**Table 4.1:** Fitted exponents for underscreened and fully screened Kondo effects

| Single-channel (Fits based on Eq. (4.1)) (Underscreened for $S > 1/2$) | | | | Fully screened ($2S$ screening channels) | |
|---|---|---|---|---|---|
| **Spin** | Fitted $\xi$ | $\xi(S)$, eq. (4.2) | $\alpha_S$ | **Spin** | $\alpha_S$ |
| $S = 1/2$ | $1.95 \pm 0.12$ | 2 | $0.22 \pm 0.02$ | $S = 1/2$ | 0.22, ref. [30] |
| $S = 1$ | $0.88 \pm 0.03$ | 0.89 | $0.33 \pm 0.02$ | $S = 1$ | 0.16, ref. [95] |
| $S = 3/2$ | $0.58 \pm 0.01$ | 0.58 | $0.39 \pm 0.01$ | $S = 3/2$ | 0.146, ref. [95] |
| $S = 2$ | $0.43 \pm 0.01$ | 0.44 | $0.42 \pm 0.01$ | | |
| $S = 5/2$ | $0.36 \pm 0.01$ | 0.37 | $0.43 \pm 0.01$ | | |

We rescaled the temperature from $T/T_0$ to $T/T_K$ by using the definition $G(T_K) \equiv G(0)/2$. Various functional forms were then used to attempt to fit the calculations, and this eventually led to the form shown in Eq. (4.1). Because of the rescaling, all $T_K$ in the fits were defined to be 1 (in the units of $T_K$), and the values for "Fitted $\xi$" and $\alpha_S$ shown in Table 4.1 reflect the fitted values when all 4 parameters of Eq. (4.1) were left free.

In Fig. 4.5, we show the results of the individual fits to the spin-dependent functional form shown in Eq. (4.1) for $S = \frac{1}{2}, 1, \frac{3}{2}, 2$, and $\frac{5}{2}$. The fitting function shows excellent agreement with the calculations across 7 decades of temperature. Table 4.1 summarizes the fitted exponents for each of the spin scenarios. We also plot the universal functions for each spin case in Fig. 4.5(f).

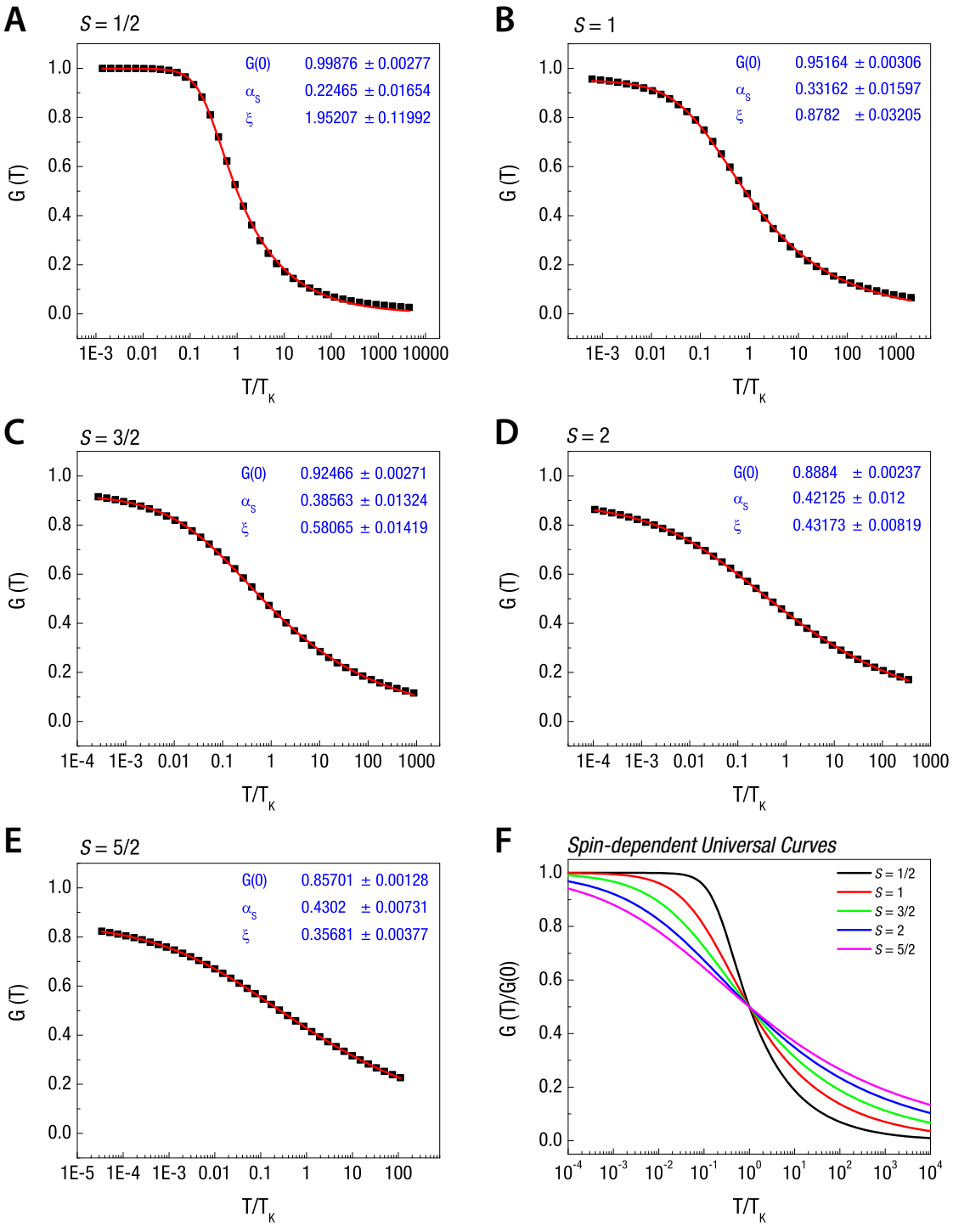


**Figure 4.5:** Fitting of NRG conductance calculations to Eq. (4.1) for a) $S = \frac{1}{2}$, b) $S = 1$, c) $S = \frac{3}{2}$, d) $S = 2$, and e) $S = \frac{5}{2}$. The fitting form provides excellent agreement with the calculations over a range of 7 decades in temperature. See the text for details. f) $G(T)/G(0)$ plotted versus $T/T_K$ for different spins using the parameters obtained from fits, listed in Table 4.1.

**Comment on temperature-independent constant offsets**

In many papers in the literature, a constant background offset $a$ is used in fitting Kondo data to NRG calculations:

$$G(T) = G(0)\, f(T/T_K) + a. \tag{4.5}$$

There are reasons to justify such a parameter, and in our previous work on $C_{60}$, we introduced such a constant for the sake of completeness. However, the rule of thumb is that the offset should be fairly small. Grobis *et al.* [85] note that if the background offset is left as a free parameter, then the offset can be of a substantial size, and $G(0)$ and $T_K$ are affected by 20-30% each. Furthermore, the net effect of the offset is that the fit is improved for large $T$, but worsened for low $T$.

In principle, one can imagine that by leaving $a$ and $\alpha_S$ completely unrestricted, a large range of data can be described. For this reason, we did not include a background offset, and stuck closely with fixed values of $\xi$ and $\alpha_S$. Furthermore, because our experimental data lies in the relatively small $T/T_K$ regime, the exclusion of a constant background would lead to a more accurate description.

CHAPTER 5

# STUDIES OF DEVICES WITH FERROMAGNETIC ELECTRODES

Two years of my Ph.D. were spent trying to make single-electron transistors attached to ferromagnetic electrodes. These devices would allow for the study of spin-dependent transport through quantum dots and perhaps more tantalizingly, the study of high-frequency precession dynamics in individual nanostructures. While these goals, in their numerous forms, were ultimately not successful, the main ideas are worth revisiting in the future, perhaps with a fresh set of hands. This chapter describes the fabrication and characterization of ferromagnetic-electrode devices, as well as the progress towards experiments.

## 5.1 Motivation

Recent theories predict a wide range of physical phenomena that arise from the interplay between spin-dependent transport and single-electron physics in nanometer-scale quantum dots [97–103]. Controlled experiments that test these predictions would provide valuable insight into the mechanisms affecting the tunneling magnetoresistance (TMR), spin accumulation, the Hanle effect, as well as interaction-induced magnetic fields.

However, due to the technical challenges involved in coupling an individual quantum dot to ferromagnetic electrodes, the number of experimental studies to date has been rather limited [51,104–107]. Developing strategies to reliably contact molecules and nanoparticles to ferromagnetic electrodes with well-defined properties would be of great importance, not only for the study of fundamental phenomena, but also for potential magnetic memory and storage applications.

In addition to DC measurements of spin-dependent transport, we were also interested in pushing high-frequency measurement techniques [108, 109] to study spin dynamics at the level of a single molecule or a nanoparticle. Such experiments would allow a new level of spin control, and could provide detailed information with regards to spin-torque-induced excitations as well as mechanisms that limit spin coherence in these structures.

## 5.2 Device design and fabrication

There were numerous considerations in the design of the ferromagnetic-electrode devices. Many of the considerations revolved around compatibility with high-frequency measurements; the devices could be used for DC measurements as well. First, we used a silicon wafer with a thick 10,000 Å oxide layer in order to reduce capacitance, and hence, possible leakage of high-frequency current to the substrate. We used highly doped silicon wafers, as has been tradition with the magnetic nanopillar devices within the group, but later found out that a rule of thumb[1] for microwave measurements is to use silicon with a resistivity of at least 100 Ω·cm to prevent losses due to substrate conductivity.

A second consideration was to keep the size of individual devices small and well-separated from each other. The dimensions for each device, including contact pads, were $\sim 400\ \mu\text{m} \times 400\ \mu\text{m}$, and the devices were separated by $\sim 1$ mm. Third, we sought to have compatibility with the CNS high-frequency probe station, so the center of the contact pads were separated by 150 $\mu$m, to match the pitch of the high-frequency probes. Fourth, the field of the electromagnet was

[1] See http://www.microwaves101.com/encyclopedia/microstriploss_conductivity.cfm.

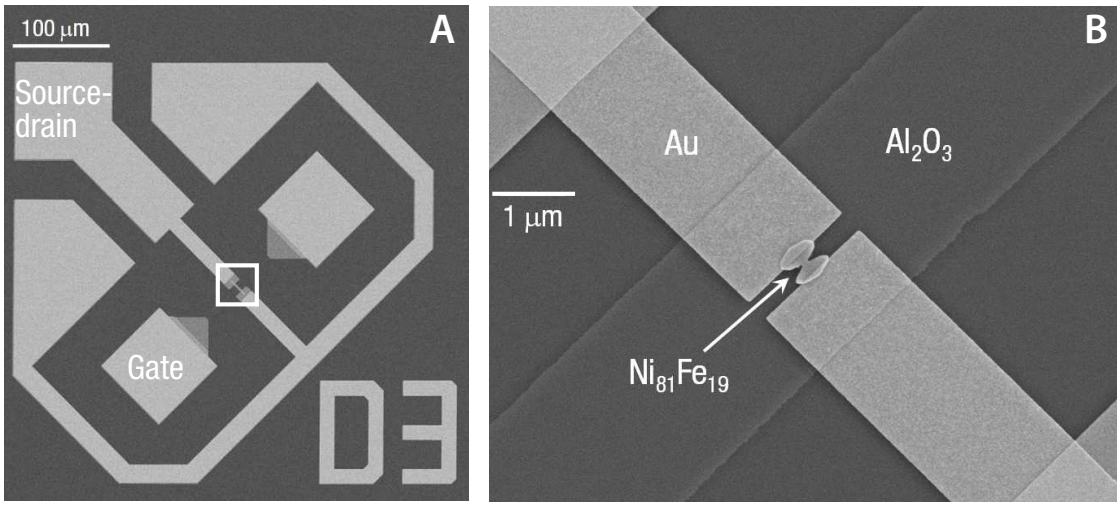


**Figure 5.1:** a) SEM of a device, showing the 3 source-drain contacts on the upper left and the 2 gate contacts. The junction region is marked by a white box. b) A zoom-in of the junction region, showing the gate oxide, Au pads, and the magnetic electrodes.

oriented 45° with respect to the probe arms, so to account for this, the devices were also rotated 45°. We allowed for three different possible orientations for the probes to contact a device, so that the magnetic field could be applied at 0°, 45°, or 90° with respect to the direction of the current. Finally, the electrode design was optimized using OOMMF[2] so that the magnetic moments of the electrodes have a stable antiparallel alignment over a reasonable range of applied magnetic field.

Scanning electron micrographs of a device are shown in Figs. 5.1a and b, which reflect the points discussed above. The fabrication consists of 4 aligned photolithography and 2 aligned e-beam lithography steps. First, we begin with a patterning and etching of alignment marks for the remaining photolithography steps. Then comes a 16 nm Au layer (the "thin" Au layer), which defines the

[2]http://math.nist.gov/oommf

contact pads as well as the large features shown in Fig. 5.1a. The third step is the "thick" Au layer, which involves deposition of ~ 130 nm of Au onto a pattern almost identical to that of the thin Au layer. The discrepancy lies in the junction region (indicated by a box in Fig. 5.1a), where the thick Au layer is recessed by ~ 5 $\mu$m so that an aligned e-beam layer that comes later will contact *only* the thin Au layer. The last photolithography step is the ~ 2 $\mu$m thick Al strip that runs between the two gate contacts shown in Fig. 5.1a; the evaporation is done at liquid $N_2$ temperatures to promote surface smoothness of the Al film, and the layer is then oxidized (Fig. 5.1b). Metal deposition for the photolithography steps is done using e-beam evaporation, and a 1 nm Ti adhesion layer is used.

The e-beam lithography steps involve two locally aligned 16 nm thick Au pads separated by ~ 350 nm, followed by locally aligned 32 nm thick permalloy ($Ni_{81}Fe_{19}$) ellipses; these features are shown in Fig. 5.1b. A very thin adhesion layer (< 1 nm Cr) was sometimes used when evaporating the Py layer, but no significant differences were noticed. The Au layer was deposited via e-beam evaporation, but the Py layer was deposited via thermal evaporation, something that will again be stressed in Sec. 5.2.5. The following sections will detail some of the finer points of the fabrication as well as a few helpful hints.

### 5.2.1 Masks and alignment marks

The masks were made with a few additional features compared to that of previous generations. These helped with the alignment and processing steps that came later in the fabrication. For the first mask that is used to define alignment marks, we not only included the standard GCA keys, but also several global

alignment marks for the VB6 and the JEOL. Typically, you would not rely on these, but there was an occasion in which they were of immense help. If you anticipate that the wafer may be processed in *pieces*, then it would also be helpful to define a few more sets of GCA keys offset from the main one so that each section of the wafer can be processed independently. CAD files for all of these masks will be available on the Ralph group wiki site.

**Etching alignment marks: Oxford 100**

The alignment marks are etched into the silicon oxide (traditionally via the PT72), then directly into the silicon (via the Unaxis). The PT72 has a nominal etch rate of $\sim 30$ nm/min for thermally grown oxide, but the average rate falls to a small fraction of that value for a long run, thus causing much consternation. For recent fabrications, I took advantage of the Oxford 100, which has a fast etch rate of $\sim 120$ nm/min for thermal oxide. The primary motivation for initially using the Oxford 100 was the thick oxide layers. However, given its significantly faster etch rate, I don't see why the Oxford 100 should not be used for wafers with thinner oxide. It will save much time and heart ache. After the oxide etch step, the Unaxis is used to etch the silicon, as per the norm.

**Mask for the thick Au layer: local alignment marks and dicing lines**

In previous masks of break junction devices in the group, specific local alignment marks were not defined, so that for e-beam lithography, very large features from the photolithography steps were used for global alignment. This was clearly non-optimal. So in the mask for the thick gold layer, I included 4 sets of alignment

marks for the VB6 (a 10 $\mu$m $\times$ 10 $\mu$m square) and for the JEOL (a Greek cross with arms that are 63 $\mu$m long and 3 $\mu$m wide). Long array marks were placed around the VB6 squares to make it very easy to identify them under a microscope. These alignment marks can be used for global alignment (e.g., by choosing one from each of the four corner dies of the wafer) or for local alignment. Because the alignment marks are made of >100 nm Au, the image contrast is extremely good under an SEM such that the e-beam software identifies them without a hitch.

In addition to the e-beam alignment marks, dicing lines were included by defining a 20 $\mu$m border around the mask. These take the guesswork out of dicing the wafer, which is the final and perhaps most frightening step of the fabrication process. Also, in contrast to previous generations, all of the photolithography was done using *positive* masks, as will be detailed in the next section.

### 5.2.2 Image reversal begone: using LOR

The traditional approach to photolithography in the group has been to use an ammonia-based image-reversal process [47, 48, 110]. This procedure effectively turns a positive photoresist into a negative one, and in the process, changes the profile of the resist so that it develops an undercut. This characteristic is important for metal deposition and liftoff because it helps to prevent a phenomenon known as "fencing," in which the edges of the lithographically defined metal are clearly much taller than the rest of the feature (see Fig. 5.2a). It is important to avoid fencing when doing multi-layer lithography, particularly when a subsequent thin metal layer needs to be directly contacted over an edge.

Ammonia-based image reversal has given rather mixed results for our lithog-

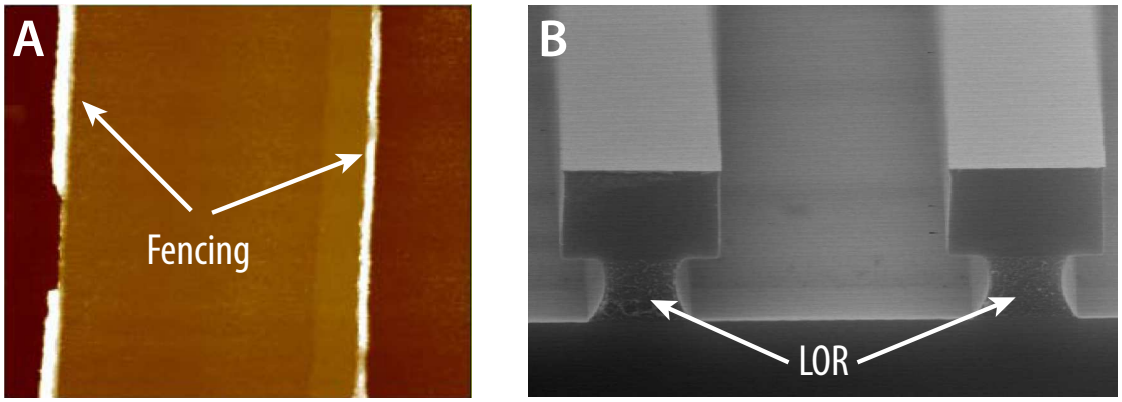


**Figure 5.2:** a) Demonstration of the "fencing" phenomenon in the deposition and liftoff of a metal, as a result of a poor undercut from the image reversal process (adapted from [110]). b) A LOR bi-layer recipe produces nice undercuts, from http://www.microchem.com.

raphy (~ 40% success rate) as well as for Ferdinand's [110]. With the availability of LOR resists[3] at CNF, a complete switch from image reversal to LOR was made, as the latter has been 100% reliable so long as the solution is reasonably fresh. When the process does not work, owing to contamination or degradation of the community-shared LOR, no wafers are wasted (unlike for image reversal), because the lithography features are washed out such that one would not even think about going ahead with metal deposition.

The LOR process basically consists of a bilayer recipe in which the LOR is the bottom layer, and a photoresist (e.g. Shipley 1813) is the top layer. The LOR is removed at a faster rate by the developer than the photoresist, so that an undercut is created (see Fig. 5.2b). The recipe calls for a few extra spinning, baking, and development steps, but given the success rate and robustness of the specific recipe details, it is well worth the time. One other thing to note is that LOR does *not* dissolve in acetone, so that for liftoff, a solution based on *N*-

[3]See http://www.microchem.com for specifications.

Methyl-2-pyrrolidone must be used. There are two common ones: Microposit Remover 1165 and Microchem Remover PG. Both strippers seem to be very similar, but the latter is about twice as expensive (~ $150 per bottle), so we use 1165. Here is a recipe that was found to work very well.

1. Clean wafer with acetone/IPA while spinning.
2. Dehydration: Bake wafers on a 180° C hotplate for 10 min.
3. Spin LOR3A[4] in the polyimide spinner. Program two steps:
   - Dispense the LOR while the spinner is at 500 rpm (200 rpm/s acceleration, step time: 5 sec). It is okay to not do this dynamically.
   - Spin for 45 sec at 3500 rpm at a ramp rate of 1000 rpm/s.
4. Bake at 180° C for 10 min (LOR soft-bake step).
5. Spin S1813 at 4000 rpm for 45 sec at a ramp rate of 1000 rpm/s.
6. Bake 2 min at 115° C.
7. Expose desired pattern on the stepper.
8. Do a post-exposure bake for 2 min at 115° C.
9. Develop the S1813 with MF321 for 60 sec on an automated machine. Use a "double puddle" recipe if available. This is an incomplete, gentle developing step.
10. Bake at 135° C for 5 min. This step is critical, as it "hard bakes" the photoresist and makes it more resistive to a developer, but does not do much to the LOR.

[4]LOR5A and even LOR10A have worked well. These numbers indicate their nominal thicknesses in 100's of nm for a spin at 3000 rpm. The solutions do get noticeably more viscous, so properly dispensing them onto the wafer without bubbles will be more challenging. Recently, the "B" series line has been introduced.

11. Develop with 300MIF for 60 sec on an automated machine. Use a "double puddle" recipe if available. This step finishes the developing process and creates the undercut.
12. Descum in your favorite etcher, e.g. for 1 min on the Oxford 80.
13. Do an evaporation.
14. Liftoff in 1165 remover. Acetone will *not* remove LOR!

### 5.2.3 Rational electrode design: OOMMF simulations

The desired characteristics of the magnetic electrodes were both clean parallel and antiparallel alignment of the magnetic moments over a reasonable field range. Towards this end, I did some micromagnetic modeling in OOMMF before deciding on the electrode designs. The two questions that I explored were: 1) whether it is feasible for electrodes made from a single e-beam lithography step to have the desired properties and 2) whether Kirill's two-layer e-beam design [111] could be further optimized.

For the one-step e-beam design simulations, a "hammer" shape, which consists of an ellipse attached to thin leads, seemed to show the most promise. Two prototype structures from an e-beam dose test are shown in Fig. 5.3a. With regards to the switching dynamics, the basic idea for such a structure is that the elliptical parts contain magnetic vortex states near the switching transition such that the moments of the junctions are arranged antiparallel. In the actual device, the "bowtie" parts were further widened and elongated to minimize resistance. While promising *in silico*, the pattern ultimately did not work, as there were issues with electromigrating the wires: the ellipses might be deformed during

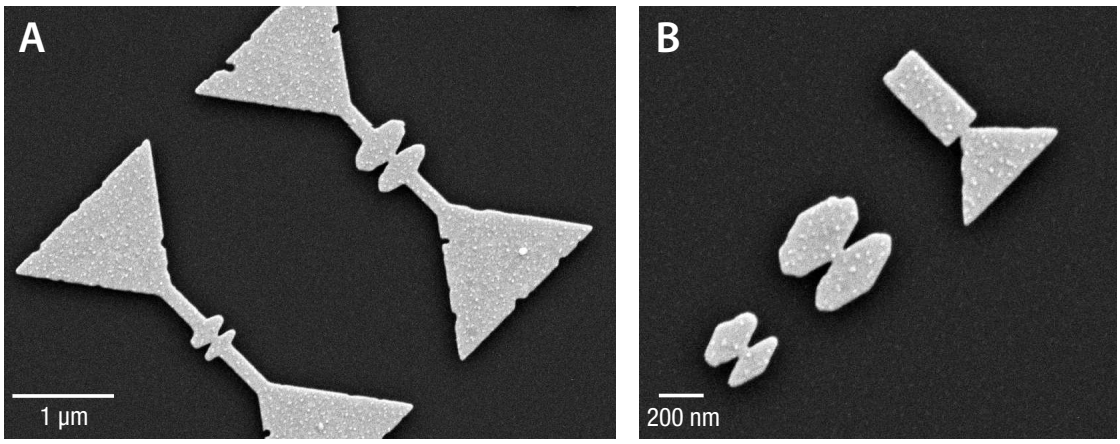


**Figure 5.3:** SEMs of possible electrode designs, from a dose test. a) "Hammer" shapes, for fabrication with a single e-beam step. b) Several possibilities for the magnetic electrodes, for a two-level e-beam lithography process.

the electromigration process or the electromigration could happen at the wrong place in the wire. Furthermore, all-Py wires broke at rather high voltages and led to large gaps. So instead, I ended up using a two-layer e-beam process, in which the first layer consists of two Au pads, and the second layer consists of two small magnetic electrodes (e.g., see Fig. 5.1b).

Several of the considered designs for the second-layer e-beam step are shown in Fig. 5.3b. Among them are the rectangle-triangle design used by Abhay [51] and two ellipse variants. The shape of each electrode is different so that they have different switching fields; for ellipses, this is achieved by having a different semi-minor axis length in each electrode.

While all of these structures were eventually fabricated, only the ellipse designs exhibited the desired properties in the micromagnetic modeling. Notably, stable parallel and antiparallel configurations were fairly immune to small-scale variations in the structure, which was an important consideration because

first, e-beam lithography does not produce perfect ellipses, and second, the post-electromigrated electrode shapes may show large variations. Furthermore, slightly smaller ellipses seemed to show better properties in the simulations.

### 5.2.4 E-beam lithography

#### Leica VB6 scripts

All of the e-beam scripts and pattern files are neatly organized into subdirectories within the main `[VB.USERS.RALPH.JOSH.FMR]` directory. (The files for the mechanical break junctions are in `[VB.USERS.RALPH.JOSH.MBJ]`.) They include dose tests, one-layer and two-layer magnetic devices, and Au devices as well. The reader may find these scripts to be helpful, particularly for looking up appropriate syntax to do alignment or a dose test. For each run, there are four commands that need to be executed.

- `@1_ALIGN_MARK_DEF.COM` : Define alignment mark, a 10 $\mu$m $\times$ 10 $\mu$m square.
- `@2_GLOBAL_ALIGN.COM` : Global alignment step.
- `@3_CENTER_WAFER.COM` : Shift the origin to the center of wafer.
- `@4_PROCESS_NAME.COM` : The actual writing step.

#### Two-level e-beam process

The two-level e-beam process consists of an aligned exposure of the Au pads followed by an aligned exposure of the magnetic ellipses. Because the ellipse patterns are fairly small, there is very little room for shifts and errors; doing only

a global alignment results in a mere ~ 60% yield of usable devices. As a result, we turned to local alignment. The wafer contains 132 dies (12 × 12 grid with 3 dies in each corner left blank), and local coordinates were configured for every 2 × 2 grid, using alignment marks patterned on each die during a photolithography step. Automated identification of alignment marks and coordinate calculations significantly slow down the e-beam run. The writing time alone (excluding pump down, calibration, and global alignment) for the Au pads can take more than 4 hours, and for the ellipses more than 3 hours. Because of scheduling restrictions, the e-beam runs may need to be done at odd hours.

**E-beam resist recipes**

Our group has been using a bilayer recipe consisting of a layer of MMA/MAA on the bottom and a layer of 495K PMMA on top. While the recipe should give good undercuts, it seems to noticeably reduce resolution and overall quality, and requires higher doses than a PMMA layer alone. I have found that a single 950K PMMA layer does not seem to give much fencing effects, if any at all, possibly since the PMMA layers are far thinner than photoresist layers; this route may be one to consider. If concerned about undercuts, I imagine that a 495K/950K PMMA bilayer may give you the desired effects (because of different resist sensitivities) without as large of a drop in resolution and quality.

### 5.2.5 Permalloy evaporations: do them thermally

This cannot be stressed enough, so even if it is a rather minor point, it is getting its own section. For permalloy ($Ni_{81}Fe_{19}$) evaporations on the Sharon, do them

thermally. When using new pellets for an e-gun evaporation, no matter how you tweak the ramping, you will be re-creating Mount Doom inside the chamber, splattering large pieces of lava-like material everywhere. Even when things settle down, there is always the threat of an eruption, which can throw off the crystal monitor and the chamber pressure, or even worse, happen in the middle of evaporating onto your sample. If you closely examine your crucible after the evaporation, you will probably notice that there are cracks; the Lesker website tells us that the crucibles are good for only one evaporation (for Py). Bearing in mind that these are your precious devices that we are talking about – not a certain ring that needs to be destroyed in Mordor – doing a thermal evaporation using a tungsten boat will save you much grief. Note that the required current will be almost near the maximum threshold, so make sure your boat is well-contacted, and be prepared to crank the current-control knob. We have not been able to get liftoff to work after sputtering, but it may be worth trying, since evaporation leads to Ni-rich permalloy, whereas sputtering preserves the content of its target.

## 5.3 Electrode characterization

Measurements were carried out in the CNS high-frequency probe station equipped with an electromagnet as well as on a dipstick with superconducting coils on the vacuum can. The numerous and recurring leaks on the probe station made it very difficult to get stable contact at low temperature, and we were never able to get good measurements on the setup. We eventually switched to a dipstick, with plans to modify the stick for high-frequency measurements if experiments looked promising. In this section, we describe characterization of the magnetic electrodes using the dipstick.

**Magnet calibration**

We made an effort to calibrate the dipstick magnet a little bit more carefully than was done before. A Hall sensor was mounted onto a chip carrier and was cooled to $T = 4.2$ K. Using a control current of 1 mA through the sensor, the Hall voltage was measured as a function of the current supplied by the Kepco through the superconducting coils. The result is shown in Fig. 5.4a, with the fitted slope being 23.2 mV/A. Because these sensors vary wildly in their Hall coefficients, I then calibrated the Hall voltage to the superconducting magnet controller on the TLM dilution fridge, which was operated at $T = 1.8$ K. The results are shown in Fig. 5.4b, with the slope of the fit (in the field range up to 1 T) being 238.9 mV/T. From this, we determined that 1 A of Kepco supply current corresponds to a field of about 0.0971 T.

**Switching characteristics**

In Fig. 5.4, we show measurements of the switching characteristics of elliptical Py electrodes in which a nanoscale gap was created by electromigration. We use as the definition for the tunneling magnetoresistance TMR = $(R_{AP} - R_P)/R_P$. Clear regions of high and low resistance suggest the formation of well-defined parallel and antiparallel states. According to the Jullière Model [112], the TMR provides information about the spin-polarization in the magnets

$$\text{TMR} = \frac{2P^2}{1 - P^2}, \tag{5.1}$$

where $P$ is the spin polarization of the magnetic electrodes. This quantity is defined by $P = (\nu_\uparrow - \nu_\downarrow)/(\nu_\uparrow + \nu_\downarrow)$ where $\nu_\uparrow$ and $\nu_\downarrow$ are the density of states for spin-up and spin-down electrons, respectively, at the Fermi level. From the

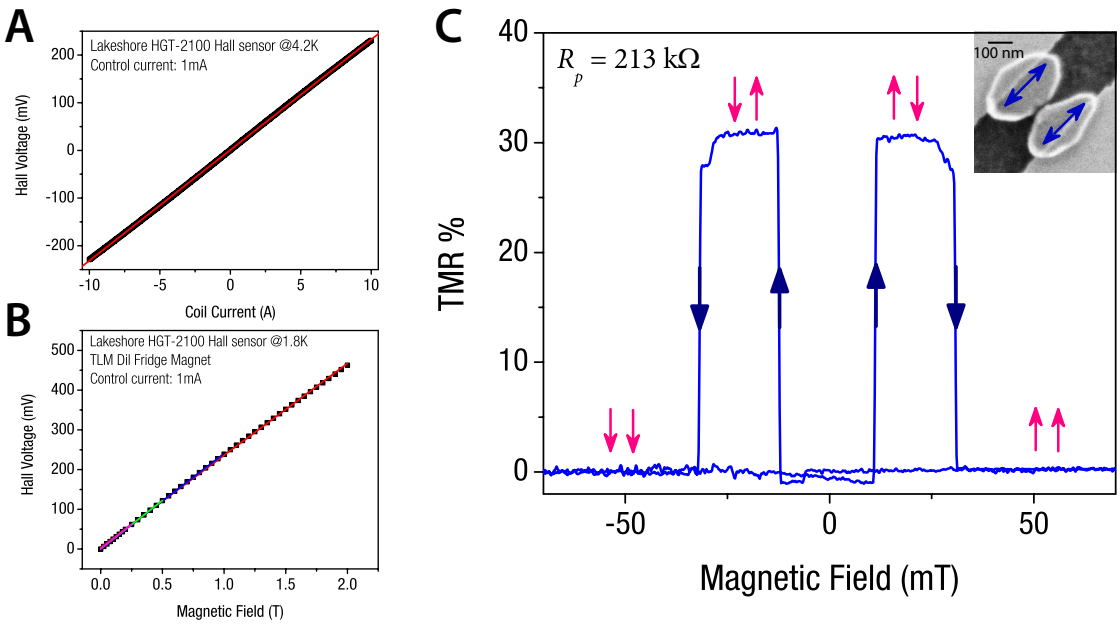


**Figure 5.4:** Magnet calibration and switching characteristics. a) Hall voltage vs. Kepco current in a 4.2 K dunker. b) Hall voltage vs. dilution fridge magnet reading at $T$ = 4.2 K. c) Switching characteristics of the electrodes $T$ = 4.2 K.

~31% TMR of our device, we estimate $P \sim 37\%$. This value is comparable to a spin polarization of 35% obtained by point-contact Andreev spectroscopy measurements in Py films [113]. Measurements of electrodes with bowtie or rectangle-triangle shapes did not produce as large TMR values, and showed significant device-to-device variations.

## 5.4 Experiments

We now describe several of the experiments that were pursued. While they were ultimately not successful, my hope is the following sections may be a useful as a starting point for a future student.

### 5.4.1 Kondo effect with ferromagnetic electrodes

One experiment that was of interest was the study of the Kondo effect in a molecule attached to ferromagnetic electrodes, particularly the prospect of using a gate voltage to control an effective magnetic field. Such an opportunity is presented because a major difference in the physics of a system with ferromagnetic leads is the emergence of an *exchange field*. To motivate why such an entity might exist, we can consider a localized spin on a quantum dot that is well-coupled to the electrodes (as discussed in Chapter 2). In such a case, there will be an appreciable exchange interaction of the form $J\,\mathbf{s}\cdot\mathbf{S}$, where $\mathbf{S}$ is the localized spin and $\mathbf{s}$ represents a net spin for a ferromagnetic electrode at the Fermi energy. To the localized spin, this interaction very much looks like a Zeeman coupling $\mathcal{H}_Z = g\mu_B\mathbf{B}_{ex}\cdot\mathbf{S}$, so that the spin feels an effective magnetic field $\mathbf{B}_{ex}$ (the exchange field) when the electrodes are spin-polarized. Figure 5.5a depicts a schematic of this situation. Both the source and drain electrodes contribute an effective field, so that for parallel alignment of the magnetic moments, the exchange field will be maximized, but for antiparallel alignment, the exchange field contribution from each electrode points in opposite directions such that the net exchange field may be reduced all the way to zero. In the presence of an applied magnetic field $\mathbf{B}$, the total field experienced by the localized spin will just be $\mathbf{B} + \mathbf{B}_{ex}$ (Fig. 5.5a).

Pasupathy *et al.* [51] demonstrated a splitting in the Kondo peak for $C_{60}$ molecules attached to Ni electrodes, a phenomenon that could be explained by an exchange field [99]. The Kondo peak could be restored as the magnetic moments of the electrodes were turned antiparallel, where any residual Kondo splitting might be attributed to a difference in coupling to the source and drain

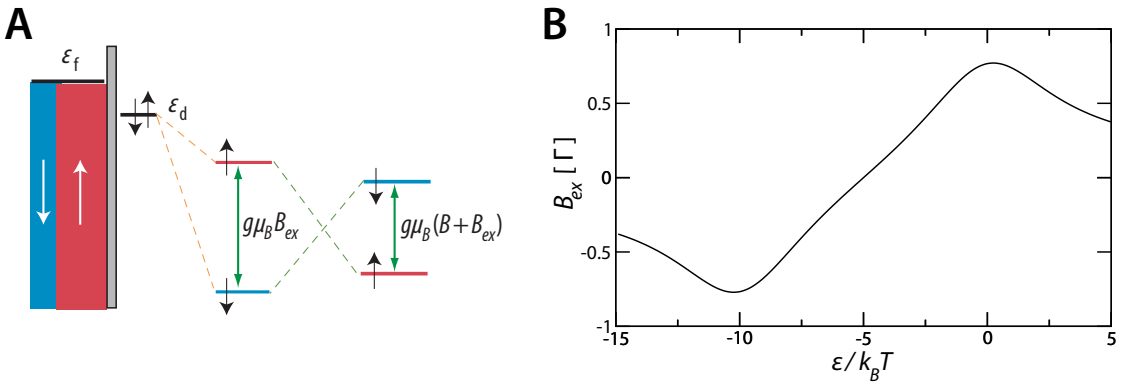


**Figure 5.5:** a) When a localized spin is coupled to spin-polarized leads, an exchange field will emerge. Adapted from [106]. b) The exchange field (in units of coupling strength Γ) versus the position of the localized level. For this plot, $U/k_BT = 10$, and the electrode is assumed to be a half-metal. Adapted from [114].

electrodes or by a misalignment angle between the electrode moments.

The exchange field can be found analytically with the assumption of an energy-independent tunnel coupling Γ [115]

$$B_{ex} \simeq \frac{\Gamma P}{\pi} \mathrm{Re}[\phi(\epsilon) - \phi(U+\epsilon)], \tag{5.2}$$

where $P$ is the spin polarization of the electrodes, $\epsilon$ is the energy of the localized spin with respect to the Fermi level, and $\phi$ is a variant of the digamma function. Based on the above expression, we see that the exchange field requires spin-polarized electrodes $P \neq 0$, a Coulomb repulsion $U \neq 0$, and good tunnel coupling. The exchange field is also dependent on the level position $\epsilon$, and from Fig. 5.5b, we see that both the magnitude and sign of the field can be controlled as a function of level position.

I cooled down the TLM in the Fall of 2007, and in measurements of Py-$C_{60}$-Py junctions, I started to see a few hints that suggested gate-control of the

exchange field (made somewhat ambiguous because of a leaky gate). However, a preprint came out in arxiv in early November of that year, in which Hauptmann *et al.* presented very nice data that demonstrated the things that I had set out to explore. The work was published 6 months later [106], and I thank the Copenhagen group for sharing their results early. In retrospect, perhaps I should have pushed on, but at the time, I had an A-exam to take, and felt that there were larger fish to catch (see Sec. 5.4.2), so I decided to focus on other projects.

I have never made ferromagnetic mechanical break junctions, but it may be an interesting experiment to control the exchange field by varying the coupling $\Gamma$. However, one may need to be careful about magnetostriction effects [116].

### 5.4.2 High-frequency measurements

The goal of these experiments was to progress towards electrical excitation and detection of spin precession in an individual molecule or a nanoparticle – possibly at the level of a single spin. Our strategy was based on the microwave techniques used in the measurement of precessional dynamics in magnetic nanopillars, developed by the group [108, 109]. A few recent techniques for single-spin detection have included very impressive advances in magnetic resonance force microscopy [117] as well as clever use of spin-to-charge conversion in GaAs double quantum dots [118, 119].

In a nutshell, our efforts to explore possible high-frequency dynamics involved the following. In the first technique known as spin-transfer-driven ferromagnetic resonance (ST-FMR) [109], an AC spin-transfer driving current $I(t) = I_0 \cos(\omega t)$ is used to excite magnetic resonance, which in turn results in

a time-varying magnetoresistance $R(t) \propto \Delta R \cos(\omega t + \delta)$ across the device. The scheme for detecting the precession dynamics involves the measurement of the DC component of voltage $V_{mix} = \langle I(t)R(t)\rangle = \frac{1}{2} I_0 \Delta R \cos(\delta)$ that appears at resonance. In the second technique, a DC current is applied through the sample to excite dynamics, and the spectrum of magnetoresistance oscillations induced by the precession is measured [108].

**Au electrodes**

We actually began by exploring dynamics in devices with non-magnetic Au electrodes. This was partially motivated by the STM experiments of Mannasen *et al.* [120, 121] as well as Durkan and Welland [122], who examined the spectrum of the tunneling current through a single "spin center" – provided by a nitrogen vacancy or a paramagnetic molecule. They observed a modulation of the tunneling current at the Larmor frequency, which was interpreted as being caused by the precession of a single spin. However, the reproducibility of these experiments were somewhat in question, and the physical mechanism for the observations was unclear: theories based on spin-orbit coupling and temporal spin polarization had to be invoked to explain the data [123–125].

We did not necessarily expect to obtain results similar to those of the STM experiments, but another motivation to examine this system was based on theory [126], which suggested that spin-flip coupling between the localized spin and the spin of the conduction electrons (somewhat similar to that of the Kondo effect) is critical for an oscillating conductance, with Fourier components at both the fundamental and twice the Larmor frequency. We applied the ST-FMR technique to junctions that contained $C_{60}$, cobalt bis(Terpy-SH), or cobalt bis(Terpy-

$C_5H_{10}SH$). While gateable Coulomb blockade and Kondo features were seen in the DC transport, we did not observe any discernable signals in the high-frequency measurements. The quality of the measurements on the CNS table-top cryo probe station was generally poor.

**Ferromagnetic electrodes**

Ferromagnetic-electrode devices were then measured. A clear advantage for such devices in comparison to those with Au electrodes is that any excitation of spin dynamics in the molecular junction should result in resistance oscillations, owing to magnetoresistance effects. On the theoretical side, Waintal and Parcollet have predicted that a spin-transfer torque exerted by a spin-polarized current on a nanoscale magnetic grain can stabilize uniform precession states [127, 128].

The biggest difficulty in carrying out these measurements were the small but recurring leaks on the probe station. These leaks, which seemed to never fully go away after repairs, led to poor electrical contact to the device by the probes as well as very unstable junctions due to ice build-up on the chip. During the relatively short periods in which junctions were stable enough to measure, no clear ST-FMR or DC spectra signals were observed. After many months of wrestling with the equipment, the decision was made to first switch measurement setups and to then look at ways to fabricate devices incorporating magnetic nanoparticles.

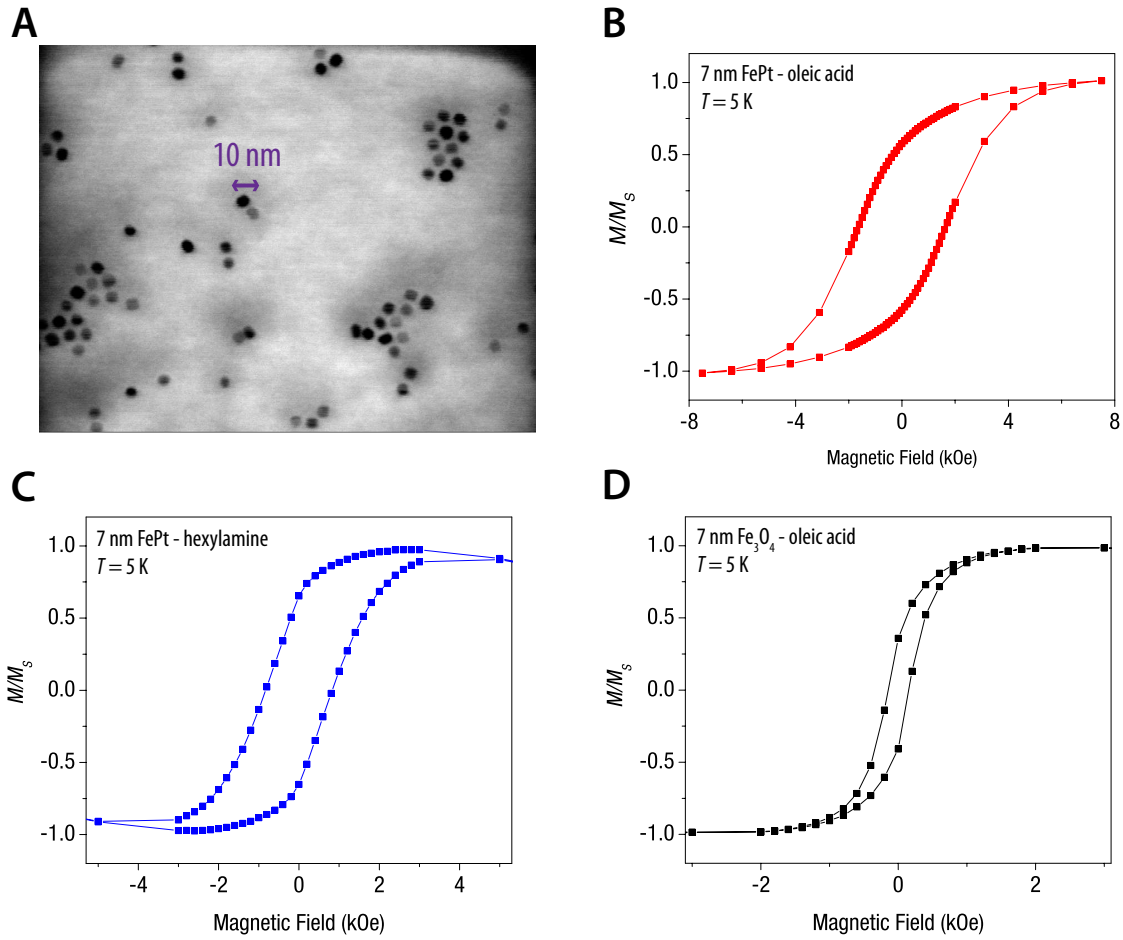


**Figure 5.6:** a) STEM image of 7 nm FePt nanoparticles. SQUID magnetization hysteresis loops at $T = 5$ K for b) FePt nanoparticles coated with oleic acid/oleylamine, c) FePt nanoparticles coated with hexylamine, and d) $Fe_3O_4$ coated with oleic acid/oleylamine.

### 5.4.3 Magnetic nanoparticles

Angang Dong in Chris Murray's group at the University of Pennsylvania synthesized for us 7 nm FePt nanoparticles. These particles have very large uniaxial magnetocrystalline anisotropy ($K_u \simeq 7 \times 10^6$ J/m$^3$), which results in magnetic stability, and are therefore of interest for high-density magnetic recording applications [129, 130]. Annealing films of FePt particles can lead to very large

coercivities, in excess of 20 kOe [131, 132]. Without annealing, FePt particles are fairly soft magnets, so we expect that they may be manipulated by an applied magnetic field or a spin-polarized current without too much difficulty.

Figure 5.6a shows an STEM image of the synthesized FePt nanoparticles. The particles appear to be monodisperse, with an average diameter of ~7 nm, as expected. We then investigated the low-temperature magnetic behavior of films of the magnetic particles on $Si/SiO_2$ substrates. In Figs. 5.6b-d, we show the change in the magnetic moment of the FePt particles with different surface groups as well as that of $Fe_3O_4$ particles (given to us just to try), as a function of applied magnetic field, at $T = 5$ K. A hysteresis loop is observed for all the particle films, consistent with magnetic behavior. We found that the coercivities can vary, with $H_c \approx 1.5$ kOe for FePt particles covered with oleic acid and oleylamine (Fig. 5.6b), $H_c \approx 1$ kOe for FePt particles covered with hexylamine (Fig. 5.6c), and $H_c \approx 0.3$ kOe for the much softer $Fe_3O_4$ particles covered with oleic acid and oleylamine (Fig. 5.6d). These differences in coercivity may reflect ligand effects, but may also be due to the particle synthesis conditions as well as film preparation.

**Aggregation in ligand-exchanged FePt particles**

We next attempted to incorporate these particles into gaps between magnetic electrodes. First, we focused on the ligand-exchanged FePt particles that had 4-bromobenzenediazonium tetrafluoroborate on the particle surface. The reason for this is that the as-made particles have on the surface oleic acid and oleylamine, which are chains that contain 18 carbon atoms, through which we do not expect to get measurable current. Figures 5.7a and b show the results of placing a

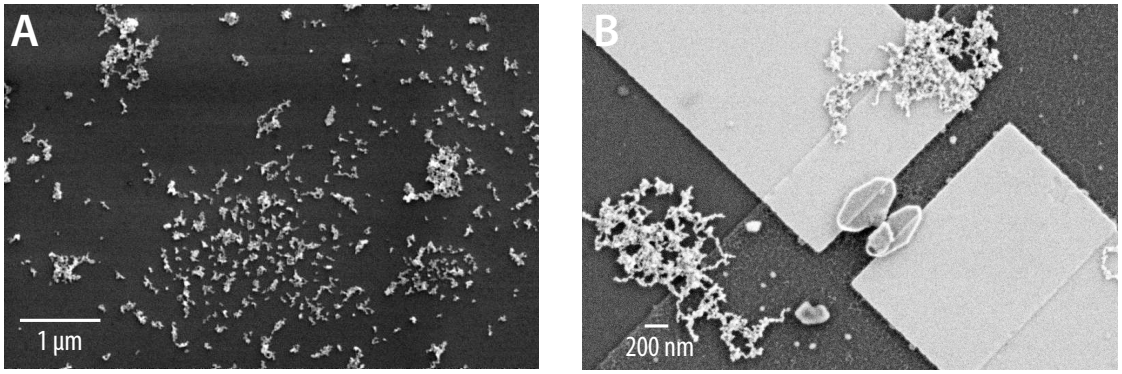


**Figure 5.7:** Ligand-exchanged FePt particles in acetonitrile, drop cast and blow dried a) on $SiO_2$ and b) near the magnetic junction.

small drop of ligand-exchanged particles in acetonitrile onto a chip and blow drying with $N_2$ gas. The particles had a strong tendency to aggregate. In an effort to obtain well-separated particles, we tried numerous things: varied the particle concentration, used mixtures of different solvents, allowed air-drying, and also used rare-earth magnets to create a perpendicular field during the drying process. However, particle aggregation remained.

Angang then sent us more particles with different ligands such as hexylamine. The idea was to have slightly longer ligands than that of the initial ligand-exchanged particles so that they would be capable surfactants, but the ligands would still be far shorter than oleic acid/oleylamine, for measuring transport. Unfortunately, these particles did not appear to be stable after about a week, which forced us to try other things.

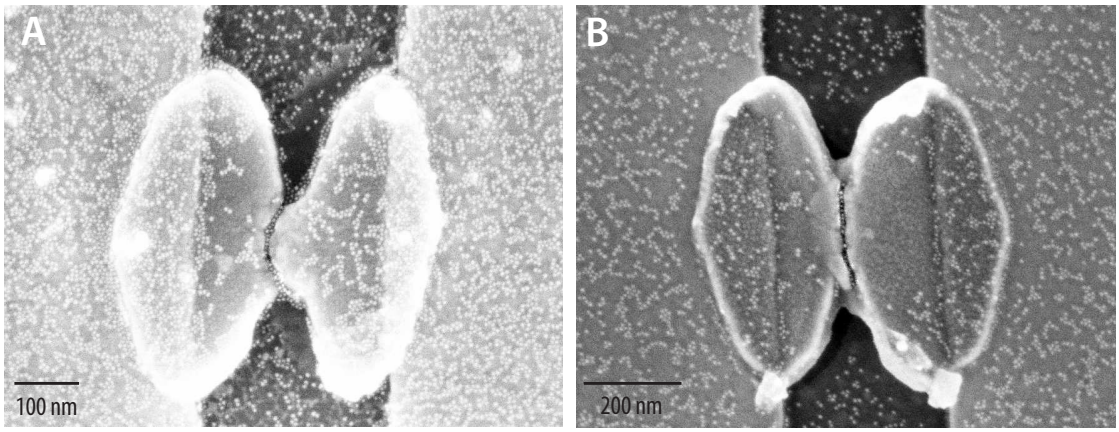


**Figure 5.8:** a) and b) Images of two magnetic junctions on different chips, after each chip was dipped in a hexane solution of FePt with oleic acid/oleylamine, and air dried. The magnetic ellipses were electromigrated prior to adding particles. The particle concentration was lower in panel b) than in a).

**Results of dipping and drying, using FePt particles with oleic acid/oleylamine**

We noticed that FePt particles with oleic acid/oleylamine ligands in hexane did not aggregate like the aforementioned ligand-exchanged particles, so we began to focus on trying to assemble them. Because hexane evaporates very quickly, an easy way to get particles onto the devices is to dip a chip into a dilute solution of FePt in hexane and to let it air dry. Figures 5.8a and b show images of electromigrated junctions after this dipping procedure, in which the FePt particles are incorporated into the gap between the magnetic electrodes. However, this process typically led to *arrays* of particles in the junction as opposed to one or a few particles. This in turn led to a lot of offset charge noise when trying to take *I-V* measurements, and of course, very large voltages were required. Despite lowering the solution concentration, the particles seemed to still have a preference for settling in the electrode gap. This can be seen in Fig. 5.8b, where a

less-concentrated solution was used than in Fig. 5.8a, but the gap is still packed with particles. A previous study with semiconductor nanocrystals and gold nanoparticles have attributed this to a capillary force [133]. The sweet spot in solution concentration for reducing particle density in the junctions appeared to be over a narrow range, as there was a fairly abrupt shift from packed junctions to empty junctions as the solution concentration was lowered. We were unable to hit this sweet spot.

**Self-assembly process**

We then turned to self-assembly. The basic idea here was to create a densely packed self-assembled monolayer (SAM) [134] of short alkanedithiol chains on the electrode surface prior to deposition of the oleic acid/oleylamine-stabilized FePt nanoparticles. The stronger affinity of the nanoparticles to the thiol groups on the SAM may displace a substantial fraction of the oleic acid/oleylamine, so that the particle may be effectively contacted to the electrodes by alkanedithiol chains. Because this procedure involves long incubation times of up to several days, we made an attempt to minimize exposure of the magnetic electrodes and particles to air. First, we electromigrated the ellipses in vacuum on the McEuen lab 4 K probe station, then immediately placed the chip into a $\sim$ 2 mM solution of 1,6-hexanedithiol (Fluka) in absolute ethanol. Parafilm was placed around the vial, which was stored either in vacuum or in a glove box for 24-48 hours, so that a well-ordered SAM could form. Next, we quickly rinsed with ethanol and transferred the chip to a solution of very dilute FePt particles in hexane for at least 24 hours. This was also stored either in vacuum or in a glove box.

Figures 5.9a-c show the results of the assembly procedure. It took many

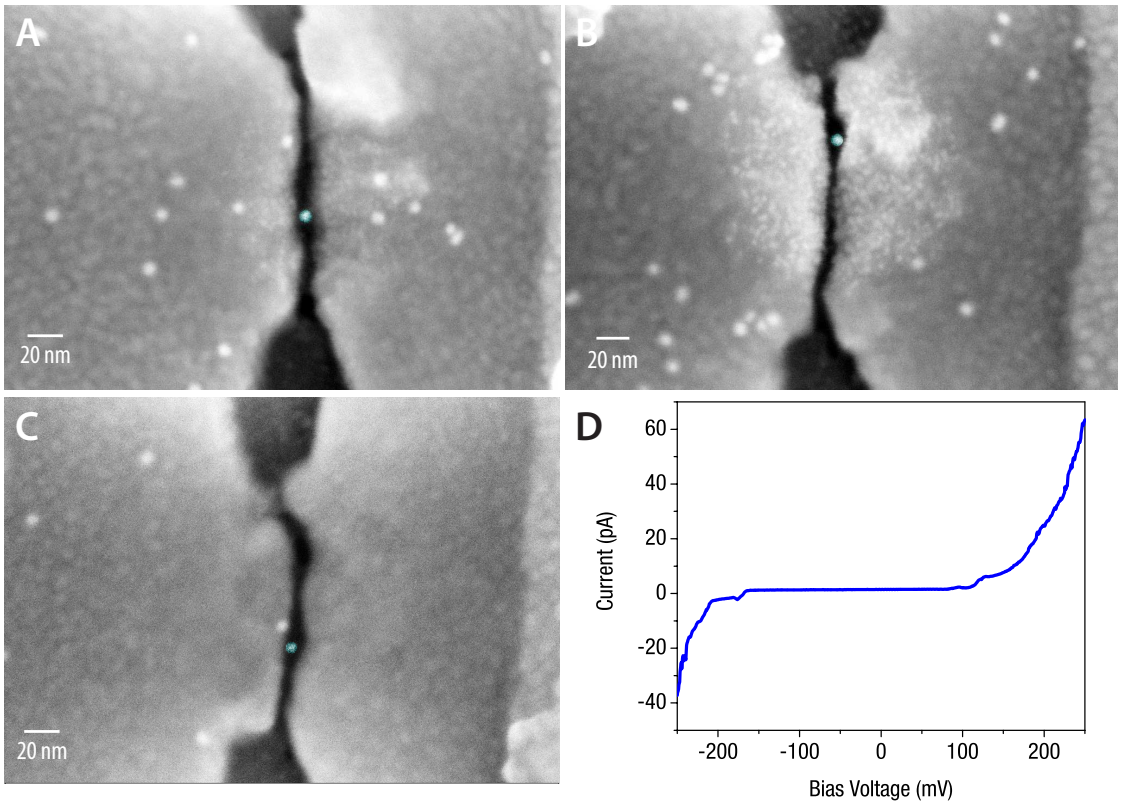


**Figure 5.9:** a) through c) SEMs of junctions in which a FePt particle was incorporated by means of a 1,6-hexanedithiol SAM. The particles between the electrodes are lightly highlighted in cyan. d) The *I-V* characteristic of a device, showing a Coulomb blockade signature.

tries before things started to work, but once they did, all 25 devices on a chip had either 0, 1, or 2 particles in the junction with respective ratios of ~ 70:20:10. Usually 1 or 2 devices per chip showed measurable currents at low temperature, and a Coulomb blockade characteristic was always observed in the *I-V*. Of the ~7-10 devices that were measured, none showed a gate dependence sufficient enough to change the charge state, and many devices were still a bit switchy. This prevented study of TMR through the nanoparticle, which would have given an indication of the extent to which ferromagnetic properties were degraded by some exposure to air.

We also measured a few $C_{60}$ devices as well. Since the molecules are first deposited on top of the electrodes and the electromigration is done in vacuum at low temperature, we expect to avoid effects of oxidation. A few $C_{60}$ devices showed some gate dependence, but the concentration of the $C_{60}$ used was a bit higher than optimal, as the transport characteristics suggested that current was flowing through multiple molecules. I did not have time to further explore these devices.

In this section, we have summarized progress towards fabricating single-electron transistors attached to ferromagnetic electrodes. While a nice device was not demonstrated, some of the ideas presented may be useful in the future.

CHAPTER 6

# ROOM-TEMPERATURE MEASUREMENTS OF SINGLE-MOLECULE CONDUCTANCE

In the previous chapters, we focused on low-temperature transport measurements of single molecules, in which we were concerned with transport *regimes* rather than the quality and reproducibility of molecule-electrode contacts. We now turn our attention to ongoing work in which we aim to measure and understand a molecule's conductance at room temperature. This is done using a statistical approach: by repeatedly forming and breaking metal-molecule-metal junctions, and building and analyzing conductance histograms. We discuss the development of the measurement apparatus (the "sewing machine"), and present preliminary results. This work was done in collaboration with Eugenia Tam and Mitk'El Benedict Santiago-Berrios. We thank Latha Venkataraman and Jonathan Widawsky for valuable advice.

## 6.1 Introduction

Understanding the conductance of a molecule has been a very difficult problem. On the experimental side, conductance measurements of a simple alkanedithiol chain attached to Au surfaces have shown discrepancies of over 5 orders of magnitude across different studies [135]. On the theoretical side, there is still ongoing debate with regards to understanding the canonical example of benzenedithiol; exotic bonding configurations [136] or a model of overlapping molecules [137] need to be invoked in order to show better agreement with the original experiment [138]. These issues point to a major difficulty in single-molecule measurements: poor control over the molecule-electrode contact.

One way to overcome this problem and to obtain meaningful information about the conductance of a molecule is to take a statistical approach. This involves constructing histograms by binning conductance values obtained by repeatedly making and breaking contact in a molecular environment (see Fig. 6.1a). In the metal-atom contact community, this procedure has been used (in the absence of molecules) to obtain information about conductance quantization in metallic point contacts [43]. As the size of the contact is narrowed by pulling apart the metals, there is a *stepwise* decrease in the conductance. For monovalent metals such as Au, these steps occur approximately at integer multiples of the conductance quantum $G_0 = \frac{2e^2}{h}$, with the lowest 1 $G_0$ conductance step arising from a single-atom contact. If this procedure is done in the presence of molecules, then additional steps below 1 $G_0$ may be observed in the traces, which indicates the formation of metal-molecule-metal junctions (Fig. 6.1b). Building a histogram of these traces provides information about the conductance of a molecule, averaged over many possible contact geometries and bonding configurations.

Smit *et al.* were the first to do low-temperature statistical measurements for the conductance of a hydrogen molecule bridging Pt electrodes, using a mechanically controllable breakjunction [60]. Xu and Tao shortly thereafter performed room-temperature statistical measurements of bipyridine molecules in solution, using a Au tip and substrate [139]. More recently, Venkataraman *et al.* measured molecules with amine end groups, and showed that amines form specific, well-defined bonds to Au, which results in narrow peaks in the conductance histogram (see Fig. 6.1c) even without having to resort to data selection [140, 141]. Their results were also in good agreement with DFT calculations. Other room-temperature studies in mechanically controllable breakjunctions have also been

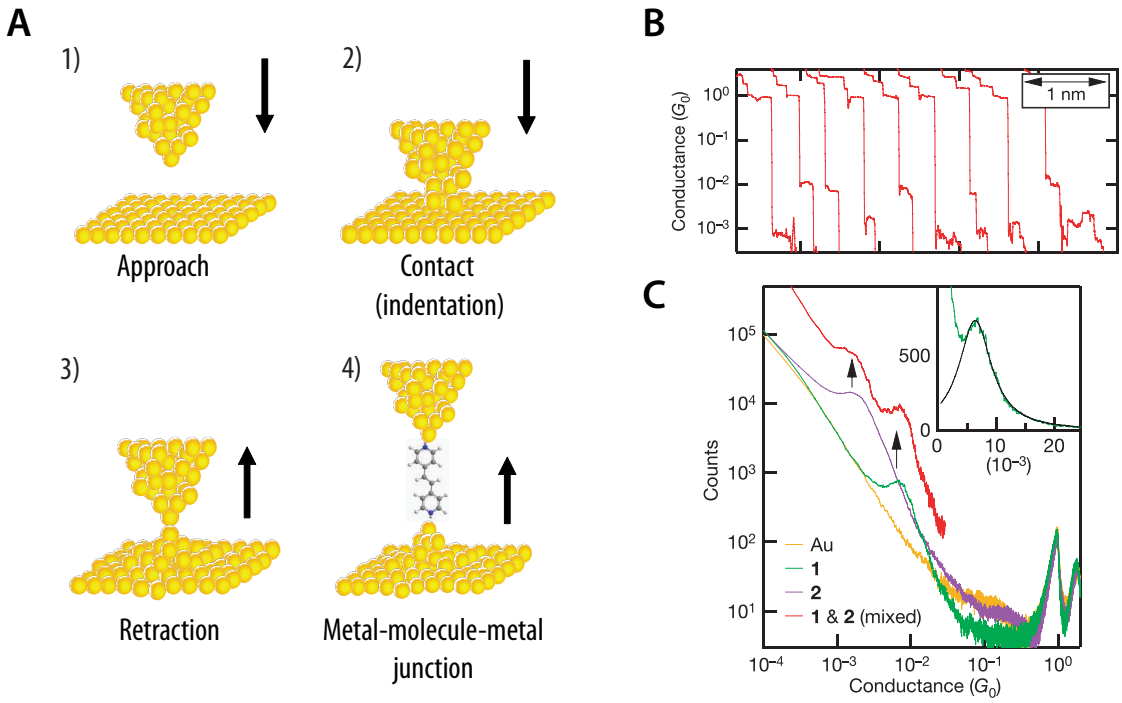


**Figure 6.1:** a) Schematic showing the repeated making and breaking of contact in a molecular environment. b) Conductance traces taken during the retraction cycle show quantization in the conductance above $G_0$ and additional plateaus below 1 $G_0$ when a metal-molecule-metal junction forms, from [141]. c) For molecules with amine end groups, clear peaks in the conductance histogram are seen below 1 $G_0$ and can be fit to a Gaussian or Lorentzian shape (see inset), from [141].

reported [142–144].

## 6.2 Instrument design

Our goal was to develop the capability to do such statistical conductance measurements. Some of the primary requirements for the "sewing machine" instrument included 1) a fast and precise control of the Au tip movement so that many make-and-break contact cycles can be completed in a short time, 2) a large

dynamic range in the conductance measurement, from contact to tunneling, 3) fast and timed data acquisition capabilities, and 4) low electrical, vibrational, and acoustic noise.

### 6.2.1 Au tip movement

The controlled mechanical motion needed to make and break contact is achieved in two stages, via a piezoelectric tip mounted on a motorized micrometer (M-227.10 DC-mike high-resolution linear actuator with piezo tip from Physik Instrumente). The micrometer, driven by the C-862 Mercury motor controller, provides 10 mm of travel range for coarse movement, while the piezo tip extends/contracts by 20 nm per volt applied. Figure 6.2 shows a photograph of the micrometer and piezo actuator. Attached to the piezo is a mount for the tip holder machined from Kel-F®. The substrate holder is also made from the same material, and the substrate clamp is electroplated with gold.

### 6.2.2 Electronics

The main pieces of electronics that we use are the 24-bit National Instruments PXI-4461 DAQ card[1], an Ithaco Model 1211 current preamplifier, and a Keithley 2400 SourceMeter. We initially used a high voltage amplifier from Physik Instrumente to drive the piezo, but we found that the noise level was far beyond acceptable for our application. We eventually decided to drive the piezo using the (unamplified) output channel of the DAQ card, because that gives us both

[1] A PXI chassis is needed to interface to a computer. Recently, a PCI version of this card has been introduced.

the resolution as well as the speed and timing that we need, through DAQmx programming. The Ithaco is probably the lowest-noise current preamp on the market. Its output is read through an ADC channel of the DAQ card, typically at a rate of 40 kS/sec (the maximum rate is 204.8 kS/sec). The Keithley 2400 is used as a bias voltage source for the Au tip. Initially, we used a second DAQ output channel, but the PXI-4461 card does not like to supply static voltages, so we chose to work around this by using the Keithley.

The original control and data acquisition system was designed around an M-series multipurpose DAQ card from National Instruments, but the card did not provide sufficient resolution for precisely driving the piezo with the output channel or for reading small currents through the input channel. We therefore upgraded to the 24-bit PXI-4461 DAQ card.

### 6.2.3 Noise isolation

#### Electrical noise

For electrical noise isolation, we removed as many potential ground loops as we could. We also use an isolation transformer to float stubborn pieces of equipment. In contrast to all DAQ cards that we have previously used, the PXI-4461 has floating outputs and differential input modes, which further help to reduce ground loops. We use a pi-filter on the output of the Keithley, which provides a static bias voltage. We also snipped the ground wire in the power cable of the Ithaco, after which the current preamp performs as well as running on battery power. The rated spectral noise density of the Ithaco at $10^{-6}$ A/V gain is $200 \times 10^{-15}$ A/$\sqrt{\text{Hz}}$, and the setting has a maximum bandwidth of $\sim 30$ kHz.

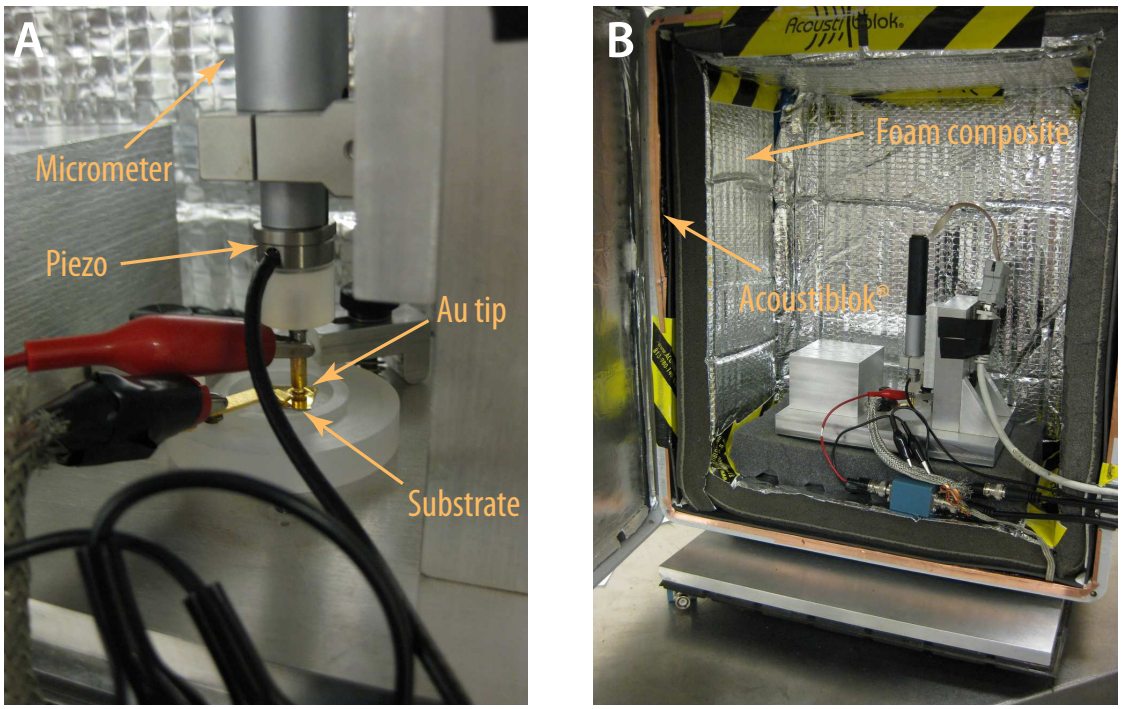


**Figure 6.2:** a) Photograph of the instrument, showing the parts that control the making and breaking of contact. b) A foam composite and Acoustiblok® soundproofing material are used for acoustic isolation. The instrument sits on a bicycle inner tube on top of a vibration-isolation table.

When applying a typical bias of 25 mV, this corresponds to an rms amplifier noise of $\sim 1.5 \times 10^{-5}\ G_0$. After these optimizations, we reached this noise floor. If lower noise is required, the rise time of the current preamp can be increased.

### Vibrational and acoustic noise

Initially, vibration isolation consisted of placing the instrument on top of a stack of 16″ diameter bicycle inner tubes, while acoustic noise was reduced by a plexiglass box padded with a composite foam (Quiet Barrier® Specialty Composite). We later moved the system to a more quiet room, and we placed the

instrument on a vibration-isolation table (Technical Manufacturing Corporation). To improve acoustic isolation, we replaced the old Plexiglass cover with a fiberglass enclosure, padded inside with the composite foam and also a layer of Acoustiblok® soundproofing material, with the edges sealed with acoustic isolation or caulking material (see Figure 6.2b).

### 6.2.4 Acquisition software

We wrote the acquisition software in National Instruments LabWindows/CVI. A typical data collection cycle begins with an automatic approach of the tip by micrometer movement. The piezo is then used to push the tip towards the substrate, in increments of ~0.2 nm. Once contact is achieved (i.e., the conductance is greater than a few $G_0$), a linear waveform is output to the piezo to begin retraction at a rate of 10-20 nm/s for a distance of 3-10 nm. The current is typically sampled at a rate of 40 kS/sec; the Au tip is biased at 10-50 mV. Conductance traces are only recorded during the retraction phase of the cycle. Under normal conditions, we are able to take a few thousand traces per hour.

The acquisition software bins the conductance counts after the completion of each trace, and an updated histogram can be visualized at any point during the data run. The user also has the option of saving individual conductance traces. We have used uniform bin sizes, but this can give low counts at high conductances if the bin size is chosen to be small. A logarithmically scaled bin size, with each count normalized by its bin size, largely gets rid of this problem [142]. The Schönenberger group has since gone further and built a logarithmic current preamplifier [144]. A second issue to consider is that when

the bin size corresponds to about 10 $\mu$V or smaller on the input of the acquisition card, the binning is affected by intrinsic digitizing noise of the ADC. It can be calibrated out by binning a uniform probability input (e.g., a linear ramp) with the same scale used for the measurement histogram [145]. We have not yet run into major issues with binning, but we plan to incorporate additional features and corrections into the software.

### 6.2.5 Sample and tip preparation

The tip is a short piece of gold wire (Alfa Aesar, 0.25 mm, 99.999% purity), freshly notched with a clean razor and pulled just before each experimental run. The substrates are silicon chips with 2 nm Ti/100 nm of Au freshly evaporated. If oxide forms on the substrate or the tip, many make-and-break contact cycles are required before conductance steps are observed; also, there is usually a small feature near ~0.1 $G_0$ in the conductance histogram. The tweezers, tip holder and the substrate holder/clamp are cleaned and blow-dried with $N_2$ gas. Conductance traces are either taken in air or with the tip immersed in 1,2,4-trichlorobenzene (TCB), a solvent that was chosen for its high boiling point of 213° C. In pure TCB, the histograms are featureless for conductances below 1 $G_0$ and are almost identical to that of Au in air. To measure molecules, we place 5-20 $\mu$L of 1-5 mM solutions on the substrate. For molecules with amine end groups, measurements are always made with fresh solutions, so as to make sure that the amine groups have not oxidized.

## 6.3 Preliminary results

In this section, we present preliminary results of our measurements of bare Au junctions and of a few molecules with amine or pyridine end groups. We chose to start by measuring these molecules, because they have been previously studied [139, 141, 146], and are expected to lead to well-defined peaks in the conductance histograms. As far as we are aware, our results represent the first ones that directly corroborate the work of Venkataraman *et al*. All of the histograms shown in the following sections were constructed without any data selection. We are also currently studying other molecules.

### 6.3.1 Gold contacts

Before embarking on molecule measurements, we chose to first examine the conductance of Au contacts, which has been thoroughly studied by many groups. Figure 6.3a shows a conductance histogram assembled from 25000 breaking traces of bare Au in TCB. We applied a bias voltage of 25 mV, and the Au tip was retracted at 20 nm/s. We observe a sharp primary peak at 1 $G_0$ and smaller peaks near 2, 3, and 4 $G_0$, consistent with previous studies of Au contacts. The downward shift from integer multiples for the latter peaks have been attributed to backscattering of electrons from defects near the contact [43]. Having observed these results, we moved onto the study of molecules.

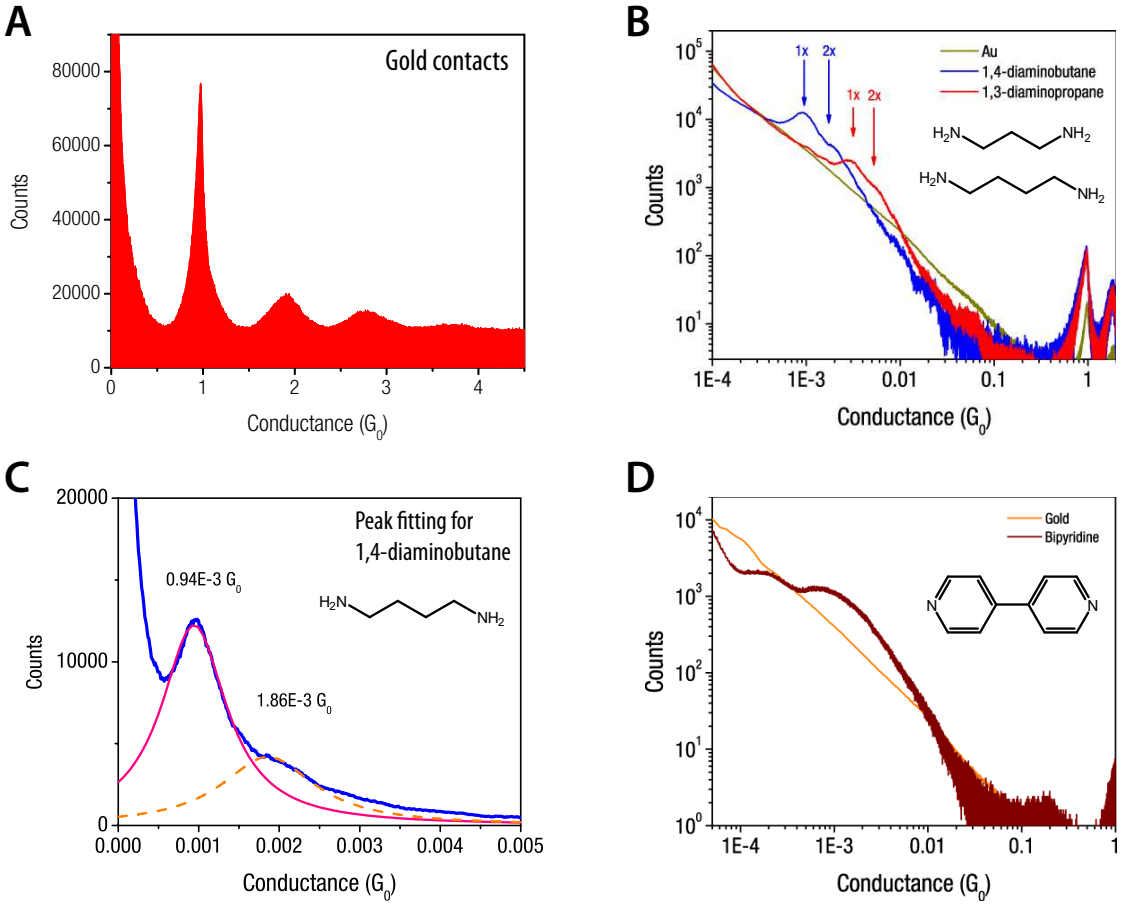


**Figure 6.3:** a) Conductance histogram for Au in TCB without any molecules, showing peaks in the conductance roughly at multiples of $G_0$. b) Conductance histograms for 1,3-diaminopentane, 1,4-diaminobutane, and bare Au. A primary and a secondary peak is observed in the histogram for the molecules. c) Fits of the primary (red) and secondary (dotted orange) peaks to a Lorentzian for 1,4-diaminobutane. The secondary peak occurs at nearly twice the value of the primary peak. d) Conductance histograms for 4,4'-bipyridine and bare Au. Two prominent peaks near 2E-4 $G_0$ and 6E-4 $G_0$ are present, similar to the observations in [146].

### 6.3.2 Diaminoalkanes and 4,4′-bipyridine

We began by measuring diaminoalkanes, as they have been demonstrated to exhibit well-defined molecular conductances [141]. We measured 1,3-diaminopropane, 1,4-diaminobutane, and 1,5-diaminopentane. The results for the first two molecules are shown in Fig. 6.3b. The conductance histograms were derived from 3000 conductance traces taken in 1 mM solutions of diaminoalkanes in TCB. The control traces of bare Au were taken in pure TCB. We used a bias of 25 mV, a retraction speed of 10 nm/s, and a bin size of $10^{-5}$ $G_0$.

As figure 6.3b shows, there is a clear primary peak in the conductance histogram for both molecules (marked as "1x" in the figure); there is also a faint secondary peak (marked as "2x" in the figure) centered at nearly twice the conductance value of the primary peak. The peak for the longer 1,4-diaminobutane occurs at a lower conductance than that of the shorter 1,3-diaminopropane, as expected, since a longer chain should be more resistive. We performed fits of the primary and secondary peaks for both molecules, and we find that the peaks are centered at $2.71 \pm 0.05 \times 10^{-3}$ $G_0$ and $5.65 \pm 0.07 \times 10^{-3}$ $G_0$ for 1,3-diaminopropane and at $0.94 \pm 0.04 \times 10^{-3}$ $G_0$ and $1.86 \pm 0.1 \times 10^{-3}$ $G_0$ 1,4-diaminobutane (shown in Fig. 6.3c). These values agree well with those obtained by Venkataraman *et al* [141], and the secondary peaks, occuring at roughly twice the conductance of the primary peak, can be interpreted as due to two molecules conducting in parallel.

We have also taken preliminary data on 4,4′-bipyridine (Fig. 6.3d). This molecule has been shown to exhibit a high conductance peak at $\sim 6 \times 10^{-4}$ $G_0$ and a low conductance peak at $\sim 2 \times 10^{-4}$ $G_0$, which have been interpreted as different stable configurations of the molecule that depend on the electrode

separation. The quality of our data may have suffered a bit, as it was taken before the vibration-isolation table was installed. Although the peaks in our data are not as sharp as those reported in the results of Quek *et al.*, the location of the conductance peaks are still consistent with their results.

## 6.4 Future experiments

We would like to continue to make improvements to the instrument, add new capabilities, and further explore ways to manipulate junctions and analyze information from individual conductance traces. One goal is to improve junction stability, so that fast *I-V* traces might be measured. This would enable us to study transport through a metal-molecule-metal junctions at room temperature. In terms of new capabilities, we would like the ability to couple in light, for the study of photochromic molecules, as well as the capability to do electrochemistry *in situ*, so that we can study redox molecules. Not only would we study transition-metal complexes as a function of the metal center, but also as a function of oxidation states. Finally, recent work has used mechanical manipulation of the molecular junction [146] and analyzed the plateaus of conductance traces [147], and we would like to build upon these studies to gain further understanding.

## BIBLIOGRAPHY


[1] J. Kondo, Prog. Theor. Phys. **32**, 37 (1964).

[2] A. C. Hewson, *The Kondo problem to heavy fermions* (Cambridge University Press, New York, 1997).

[3] H. Bruus and K. Flensberg, *Many-body quantum theory in condensed matter physics : an introduction* (Oxford University Press, New York, 2004).

[4] M. Pustilnik and L. Glazman, J. Phys.: Condens. Matter **16**, R513 (2004).

[5] L. Kouwenhoven and L. Glazman, Phys. World **14**, 33 (2001).

[6] D. C. Ralph and R. A. Buhrman, Phys. Rev. Lett. **69**, 2118 (1992).

[7] P. Jarillo-Herrero *et al.*, Nature **434**, 484 (2005).

[8] J. Koch, M. E. Raikh, and F. von Oppen, Phys. Rev. Lett. **96**, 056803 (2006).

[9] P. W. Anderson, Phys. Rev. **124**, 41 (1961).

[10] J. R. Schrieffer and P. A. Wolff, Phys. Rev. **149**, 491 (1966).

[11] L. I. Glazman and M. E. Raikh, JETP Lett. **47**, 452 (1988).

[12] P. Nozires and A. Blandin, J. Phys. (Paris) **41**, 193 (1980).

[13] D. Goldhaber-Gordon *et al.*, Nature **391**, 156 (1998).

[14] S. M. Cronenwett, T. H. Oosterkamp, and L. P. Kouwenhoven, Science **281**, 540 (1998).

[15] J. Nygard, D. H. Cobden, and P. E. Lindelof, Nature **408**, 342 (2000).

[16] J. Park *et al.*, Nature **417**, 722 (2002).

[17] W. Liang *et al.*, Nature **417**, 725 (2002).

[18] V. Madhavan *et al.*, Science **280**, 567 (1998).

[19] H. C. Manoharan, C. P. Lutz, and D. M. Eigler, Nature **403**, 512 (2000).

[20] A. Zhao *et al.*, Science **309**, 1542 (2005).

[21] F. D. M. Haldane, Phys. Rev. Lett. **40**, 416 (1978).

[22] W. G. van der Wiel *et al.*, Science **289**, 2105 (2000).

[23] Y. Meir, N. S. Wingreen, and P. A. Lee, Phys. Rev. Lett. **70**, 2601 (1993).

[24] Y. Meir and N. S. Wingreen, Phys. Rev. Lett. **68**, 2512 (1992).

[25] D. S. Fisher and P. A. Lee, Phys. Rev. B **23**, 6851 (1981).

[26] T. A. Costi, Phys. Rev. Lett. **85**, 1504 (2000).

[27] P. Nozires, J. Low Temp. Phys. **17**, 31 (1974).

[28] R. Bulla, T. A. Costi, and T. Pruschke, Rev. Mod. Phys. **80**, 395 (2008).

[29] T. A. Costi, A. C. Hewson, and V. Zlatic, J. Phys.: Condens. Matter **6**, 2519 (1994).

[30] D. Goldhaber-Gordon *et al.*, Phys. Rev. Lett. **81**, 5225 (1998).

[31] I. L. Aleiner, P. W. Brouwer, and L. I. Glazman, Phys. Rep. **358**, 309 (2002).

[32] M. Pustilnik and L. I. Glazman, Phys. Rev. Lett. **87**, 216601 (2001).

[33] W. G. van der Wiel *et al.*, Phys. Rev. Lett. **88**, 126803 (2002).

[34] S. Sasaki *et al.*, Nature **405**, 764 (2000).

[35] J. Schmid *et al.*, Phys. Rev. Lett. **84**, 5824 (2000).

[36] A. Kogan *et al.*, Phys. Rev. B **67**, 113309 (2003).

[37] C. H. L. Quay *et al.*, Phys. Rev. B **76**, 245311 (2007).

[38] N. Roch *et al.*, Nature **453**, 633 (2008).

[39] A. Posazhennikova and P. Coleman, Phys. Rev. Lett. **94**, 036802 (2005).

[40] G. Granger *et al.*, Phys. Rev. B **72**, 165309 (2005).

[41] W. H. A. Thijssen, Ph.D. Thesis, Universiteit Leiden, 2008.

[42] C. A. Martin *et al.*, New J. Phys. **10**, 065008 (2008).

[43] N. Agrait, A. L. Yeyati, and J. M. van Ruitenbeek, Phys. Rep. **377**, 81 (2003).

[44] J. Moreland and J. W. Ekin, J. Appl. Phys. **58**, 3888 (1985).

[45] C. J. Muller, J. M. van Ruitenbeek, and L. J. de Jongh, Phys. Rev. Lett. **69**, 140 (1992).

[46] S. A. G. Vrouwe *et al.*, Phys. Rev. B **71**, 035313 (2005).

[47] A. R. Champagne, Ph.D. Thesis, Cornell University, 2005.

[48] A. N. Pasupathy, Ph.D. Thesis, Cornell University, 2004.

[49] T. K. Ng and P. A. Lee, Phys. Rev. Lett. **61**, 1768 (1988).

[50] L. H. Yu and D. Natelson, Nano Lett. **4**, 79 (2004).

[51] A. N. Pasupathy *et al.*, Science **306**, 86 (2004).

[52] S. De Franceschi *et al.*, Phys. Rev. Lett. **89**, 156801 (2002).

[53] J. Paaske *et al.*, Nat. Phys. **2**, 460 (2006).

[54] J. M. van Ruitenbeek *et al.*, Rev. Sci. Instrum. **67**, 108 (1996).

[55] A. R. Champagne, A. N. Pasupathy, and D. C. Ralph, Nano Lett. **5**, 305 (2005).

[56] H. Park *et al.*, Appl. Phys. Lett. **75**, 301 (1999).

[57] M. L. Trouwborst, S. J. van der Molen, and B. J. van Wees, J. Appl. Phys. **99**, 7 (2006).

[58] B. W. Hoogenboom *et al.*, Phys. Rev. B **57**, 11939 (1998).

[59] R. Heid, L. Pintschovius, and J. M. Godard, Phys. Rev. B **56**, 5925 (1997).

[60] R. H. M. Smit *et al.*, Nature **419**, 906 (2002).

[61] A. N. Pasupathy *et al.*, Nano Lett. **5**, 203 (2005).

[62] J. Paaske and K. Flensberg, Phys. Rev. Lett. **94**, 176801 (2005).

[63] L. H. Yu *et al.*, Phys. Rev. Lett. **93**, 266802 (2004).

[64] A. Kogan, S. Amasha, and M. A. Kastner, Science **304**, 1293 (2004).

[65] A. Vidan *et al.*, Phys. Rev. Lett. **96**, 156802 (2006).

[66] J. J. P. Stewart and M. B. Coolidge, J. Comput. Chem. **12**, 1157 (1991).

[67] A. Ceulemans, P. W. Fowler, and I. Vos, J. Chem. Phys. **100**, 5491 (1994).

[68] D. R. Pooler, J. Phys. A: Math. Gen. **13**, 1197 (1980).

[69] N. Koga and K. Morokuma, Chem. Phys. Lett. **196**, 191 (1992).

[70] N. Manini, E. Tosatti, and A. Auerbach, Phys. Rev. B **49**, 13008 (1994).

[71] F. Negri, G. Orlandi, and F. Zerbertto, Chem. Phys. Lett. **144**, 31 (1988).

[72] H. Park *et al.*, Nature **407**, 57 (2000).

[73] J. J. Parks *et al.*, Phys. Rev. Lett. **99**, 026601 (2007).

[74] T. Bohler, A. Edtbauer, and E. Scheer, Phys. Rev. B **76**, 125432 (2007).

[75] J. I. Pascual *et al.*, J. Chem. Phys. **117**, 9531 (2002).

[76] T. Frederiksen *et al.*, Phys. Rev. B **78**, 233401 (2008).

[77] N. A. Pradhan, N. Liu, and W. Ho, J. Phys. Chem. B **109**, 8513 (2005).

[78] N. Sergueev, A. A. Demkov, and H. Guo, Phys. Rev. B **75**, 233418 (2007).

[79] N. Andrei, K. Furuya, and J. H. Lowenstein, Rev. Mod. Phys. **55**, 331 (1983).

[80] P. Mehta and N. Andrei, Phys. Rev. Lett. **96**, 216802 (2006).

[81] S.-P. Chao, Personal communication (2009).

[82] D. C. Ralph *et al.*, Phys. Rev. Lett. **72**, 1064 (1994).

[83] R. M. Potok *et al.*, Nature **446**, 167 (2007).

[84] A. Schiller and S. Hershfield, Phys. Rev. B **51**, 12896 (1995).

[85] M. Grobis *et al.*, Phys. Rev. Lett. **100**, 246601 (2008).

[86] G. D. Scott *et al.*, Phys. Rev. B **79**, 165413 (2009).

[87] H. B. Heersche *et al.*, Phys. Rev. Lett. **96**, 206801 (2006).

[88] M.-H. Jo *et al.*, Nano Lett. **6**, 2014 (2006).

[89] J. E. Grose *et al.*, Nat. Mater. **7**, 884 (2008).

[90] H. Oshio *et al.*, Inorg. Chem. **40**, 1143 (2001).

[91] R. Hogg and R. G. Wilkins, J. Chem. Soc. , 341 (1962).

[92] A. Posazhennikova, B. Bayani, and P. Coleman, Phys. Rev. B **75**, 245329 (2007).

[93] W. Koller, A. C. Hewson, and D. Meyer, Phys. Rev. B **72**, 045117 (2005).

[94] F. Mallet *et al.*, Phys. Rev. Lett. **97**, 226804 (2006).

[95] T. A. Costi *et al.*, Phys. Rev. Lett. **102**, 056802 (2009).

[96] W. Hofstetter and H. Schoeller, Phys. Rev. Lett. **88**, 016803 (2001).

[97] A. Brataas *et al.*, Phys. Rev. B **59**, 93 (1999).

[98] E. Y. Tsymbal *et al.*, Phys. Rev. Lett. **90**, 186602 (2003).

[99] J. Martinek *et al.*, Phys. Rev. Lett. **91**, 127203 (2003).

[100] J. Konig and J. Martinek, Phys. Rev. Lett. **90**, 166602 (2003).

[101] I. Weymann *et al.*, Phys. Rev. B **72**, 115334 (2005).

[102] M. Braun, J. Konig, and J. Martinek, Europhys. Lett. **72**, 294 (2005).

[103] S. Braig and P. W. Brouwer, Phys. Rev. B **71**, 195324 (2005).

[104] S. Sahoo *et al.*, Nat Phys **1**, 99 (2005).

[105] A. Bernand-Mantel *et al.*, Appl. Phys. Lett. **89**, 062502 (2006).

[106] J. R. Hauptmann, J. Paaske, and P. E. Lindelof, Nat. Phys. **4**, 373 (2008).

[107] K. Hamaya *et al.*, Phys. Rev. B **77**, 081302 (2008).

[108] S. I. Kiselev *et al.*, Nature **425**, 380 (2003).

[109] J. C. Sankey *et al.*, Phys. Rev. Lett. **96**, 227601 (2006).

[110] F. Kuemmeth, Ph.D. Thesis, Cornell University, 2008.

[111] K. I. Bolotin *et al.*, Nano Lett. **6**, 123 (2006).

[112] M. Julliere, Phys. Lett. A **54**, 225 (1975).

[113] L. Bocklage *et al.*, J. Appl. Phys. **101**, 09J512 (2007).

[114] J. Konig *et al.*, Quantum dots attached to ferromagnetic leads: Exchange field, spin precession, and kondo effect, in *CFN Lectures on Functional Nanostructures Vol. 1*, pp. 145–164, 2005.

[115] J. Martinek *et al.*, Phys. Rev. B **72**, 4 (2005).

[116] R. C. O'Handley, *Modern magnetic materials : principles and applications* (Wiley, New York, 2000).

[117] D. Rugar *et al.*, Nature **430**, 329 (2004).

[118] J. M. Elzerman *et al.*, Nature **430**, 431 (2004).

[119] F. H. L. Koppens *et al.*, Nature **442**, 766 (2006).

[120] Y. Manassen *et al.*, Phys. Rev. Lett. **62**, 2531 (1989).

[121] Y. Manassen *et al.*, Phys. Rev. B **48**, 4887 (1993).

[122] C. Durkan and M. E. Welland, Appl. Phys. Lett. **80**, 458 (2002).

[123] L. N. Bulaevskii, M. Hruska, and G. Ortiz, Phys. Rev. B **68**, 125415 (2003).

[124] A. V. Balatsky, Y. Manassen, and R. Salem, Phys. Rev. B **66**, 195416 (2002).

[125] D. Mozyrsky *et al.*, Phys. Rev. B **66**, 161313 (2002).

[126] J.-X. Zhu and A. V. Balatsky, Phys. Rev. Lett. **89**, 286802 (2002).

[127] X. Waintal and O. Parcollet, Phys. Rev. Lett. **94**, 247206 (2005).

[128] O. Parcollet and X. Waintal, Phys. Rev. B **73**, 144420 (2006).

[129] S. Sun *et al.*, Science **287**, 1989 (2000).

[130] S. Sun *et al.*, J. Phys. Chem. B **107**, 5419 (2003).

[131] H. Zeng *et al.*, Nature **420**, 395 (2002).

[132] R. D. Rutledge *et al.*, J. Am. Chem. Soc. **128**, 14210 (2006).

[133] Y. Cui *et al.*, Nano Lett. **4**, 1093 (2004).

[134] J. C. Love *et al.*, Chem. Rev. **105**, 1103 (2005).

[135] A. Salomon *et al.*, Adv. Mater. **15**, 1881 (2003).

[136] M. Di Ventra, S. T. Pantelides, and N. D. Lang, Phys. Rev. Lett. **84**, 979 (2000).

[137] E. G. Emberly and G. Kirczenow, Phys. Rev. Lett. **87**, 269701 (2001).

[138] M. A. Reed *et al.*, Science **278**, 252 (1997).

[139] B. Xu and N. J. Tao, Science **301**, 1221 (2003).

[140] L. Venkataraman *et al.*, Nano Lett. **6**, 458 (2006).

[141] L. Venkataraman *et al.*, Nature **442**, 904 (2006).

[142] M. T. Gonzalez *et al.*, Nano Lett. **6**, 2238 (2006).

[143] C. A. Martin *et al.*, J. Am. Chem. Soc. **130**, 13198 (2008).

[144] S. Wu *et al.*, Nat. Nano. **3**, 569 (2008).

[145] K. Hansen *et al.*, Phys. Rev. B **56**, 2208 (1997).

[146] S. Y. Quek *et al.*, Nat Nano **4**, 230 (2009).

[147] M. Kamenetska *et al.*, Phys. Rev. Lett. **102**, 126803 (2009).